Bergische Universität Wuppertal

Fachbereich Elektrotechnik, Informationstechnik, Medientechnik

Hybrid organic-inorganic structures for solution processed organic light emitting diodes (OLEDs)

zur Erlangung des akademischen Grades eines

Dr.-Ing.

genehmigte Dissertation
von

Author :	Danny Krautz, Dipl.-Ing., M. Sc.
Referent :	Prof. Dr. rer. nat. Thomas Riedl
Korreferent :	Prof. Dr. rer. nat. Ullrich Scherf
Tag der mündlichen Prüfung :	11.04.2014

Die Dissertation kann wie folgt zitiert werden:

urn:nbn:de:hbz:468-20140625-113409-8
[http://nbn-resolving.de/urn/resolver.pl?urn=urn%3Anbn%3Ade%3Ahbz%3A468-20140625-113409-8]

Contents

Hiermit versichere ich, die vorliegende Arbeit selbstständig verfasst und nur die angegebenen Quellen und Hilfsmittel verwendet zu haben.

Hiermit versichere ich, dass die Dissertation in der vorgelegten oder einer ähnlichen Fassung noch nicht zu einem früheren Zeitpunkt an der Bergische Universität Wuppertal oder einer anderen in – oder ausländischen Hochschule als Dissertation eingereicht worden ist.

Danny Krautz

Thanks

It has been a pleasure to work at the Fraunhofer IAP and to have the guidance of Prof. Dr. Thomas Riedl from the University Wuppertal as my supervisor for the past three years. This time has been a memorable and valuable experience. This thesis would never have seen the light of day without my supervisor's inspiration and superb guidance. Therefore, I would like to say thank you to Prof. Dr. Thomas Riedl who has been always approachable, patient, supportive and enthusiastic.

I also would like to thank Prof. Dr. Ullrich Scherf for being my co-adviser and for his valuable support.

Dr. Armin Wedel from the Fraunhofer IAP has always given sound advice that have lead to better ways of continuing my studies and I appreciate his support regarding my thesis and my work at the Fraunhofer IAP.

I am very grateful to the MERCK Southampton team for the exceptional experience during my research stay and in particular to Dr. Michael Heckmeier, Dr. Frank Meyer, Dr. David Sparrowe and Dr. Miguel Carrasco.

A thesis would not be possible with supportive and helpful colleagues. I appreciated the time spent with them inside the lab and in the real world. I enjoyed the time riding the bike to the ICFO with Dr. Lars Neumann, I enjoyed the first months sharing the cleanroom with Dr. Dominico Tulli and I enjoyed our little German island with Dr. Sybille Braungardt and Dr. Florian Wolfgramm. Additionally, I am grateful to Manuela Furkert and Luis Enrique who helped me with the lab equipment and administrative work at ICFO.

The Fraunhofer IAP group is too large to thank everyone individually, but members from the past and from the present have made it a brilliant environment to work in. In special, I would like to *say thanks to my colleagues from the Fraunhofer Institute. In particular, Dr. Tonino Greco for all the valueable discussions and for giving me motivation during the writing of the dissertation; Dr. Alexander Lange for the help of the AFM measurements; Stefanie Kreißl for processing of the samples; and Dr. Christine Boeffel for all the fruitful discussions.*

I would like to thank Dr. Steve Albrecht for introducing me to the facilities from the soft matter group at the University of Potsdam.

The thesis is coming to an end and I hope my friends will be able to breathe again. They helped me so much that I cannot express in words how much I appreciate their friendship and endless support. Markus, Maik, Silvio, Lu, Francesca, Sabrina, Martin, Korbi, Jimmy, Fred, Kathrin, Maria and Ronny, you all together are part of this story.

My mother has always been my biggest fan and gave me the biggest support through good and hard times. Love to you always.

Milene, thanks for having been a brilliant support during my PhD, I would not have gone this far without you. Thank you for trusting my capabilities during the PhD period and for being the best what happened to me. You gave me the biggest present in life, Luisa. Thank you. I love you!

List of Abbreviations

General

ALD	Atomic layer deposition
LCD	Liquid Crystal Display
OLED	Organic Light Emitting Diode
HOMO	Highest Occupied Molecular Orbital
LUMO	Lowest Unoccupied Molecular Orbital
ITO	Indium Tin Oxide
HTL	Hole Transport Layer
HBL	Hole Blocking Layer
ETL	Electron Transport Layer
EBL	Electron blocking Layer
PL	Photoluminescence
EL	Electroluminescence
AFM	Atomic Force Microscope
RPM	Revolutions Per Minute
FN	Fowler-Nordheim tunneling
RS	Richardson-Schottky thermionic emission
SCLC	Space-Charge-Limited-Current
PLQE	Photoluminescence quantum Efficiency
PLED	Polymer light emitting diode

Symbol	**Unit**	**Description**
U	V	Voltage
I	A	Current
F	V/m	Electric Field
J	A/m^2	Current Density
L	cd/m^2	Luminance
Ro	nm	Intermolecular Distance
$\mu_{n,p}$	cm^2/Vs	Charge Carrier Mobility
μ_0	cm^2/Vs	Low-Field Mobility
η_{ext}	%	external efficiency
η_r	%	internal efficiency
η_{out}	%	outcoupling efficiency
η_{mol}	%	photoluminescence efficiency
γ	%	charge-carrier balance
E$_B$	eV	Potential Barrier between LUMO and metal
N$_{p,n}$	eV^{-1}	Density of States
U$_{TFL}$	V	Trap Filling Voltage
ε_0	/	Dielectric Constant
Θ	/	Trapping Factor
N,P$_T$	cm^{-3}	Number of Trap States
k_B	eV/K	Boltzmann Constant
q	C	Electrical Charge on the Electron
n	/	Refrective Index
τ	s	Natural Radiative Lifetime
τ_r	s	Overall Lifetime

Materials

Alq_3	tris-(8-hydroxyquinoline) Aluminum
PEDOT-PSS	polyethylenedioxythiophene:polystyrenesulfonate
PFO	Poly(9,9-dioctylfluorene)
SY	Poly(phenylenevinylene) co-polymer
MEH-PPV	poly[2-methoxy-5-(28-ethyl-hexyloxy)-1,4-phenyl-enevinylene]
Al	Aluminium
Al_2O_3	Aluminum Oxide
ITO	Indium-Tin-Oxide
Ni	Nickel
Ti	Titanium
Cu	Copper
Ag	Silver
Au	Gold
N_2	Nitrogen
$CHCl_3$	Chloroform
Tol	Toluene
THF	Tetrahydrofuran
CB	Chlorobenzene
H_2O	Water

Chapter 1

Introduction and Motivation

More than 20 years ago, in 1987, Tang and V. Slyke reported the first efficient small molecule (SM)-based light emitting device using tris(8-hydroxyquinoline) aluminum Alq_3 *as active layer [1]. Three years later, a breakthrough for polymer light emitting diodes (PLEDs) was reached through the discovery of electroluminescence from poly(para-phenylene vinylene) polymers at the University of Cambridge [2]. Since then, developments of various polymer or small molecule materials [3][4] and a range of OLED architectures [5] have been investigated [6][7]. Just a few years after the above mentioned discoveries, the growing interest in industry and research opened a new market for the so-called organic electronics and, in recent times, this technology has shown its true potential for overcoming some of the limitations of inorganic semiconductor devices [8].*

Organic devices based on small molecules are already placed on the market. [9][10]. In 2002, Philips and Pioneer supplied OLEDs already in a commercial scale for mobile display applications. Only one year later, Kodak introduced the first AMOLED digital camera - the KODAK EasyShare LS633. Samsung's OLED production based on small molecules reached mass production in 2008 and this is basically due to the use of the OLED displays in their mobile phone applications. For displays, organics offer many advantages compared to the current technology of LCD and Plasma screens [11][12]. Apart from economic advantages and the requirement of simpler fabrication steps and technology, they also offer lower power consumption [13], a wider viewing angle[5] and faster response time [14]. However, there are still many challenges until OLEDs can be integrated in our daily life. Environmental conditions, such as high temperature *and high humidity, lower the operating lifetime due to the degradation of the organic material and the use of highly reactive electrode materials. Research work nowadays focuses on the increase of the device lifetime avoiding electrode materials like calcium or barium and improving the encapsulation. In addition, there is an ever growing impetus to avoid the use of less abundant and costly materials.*

In this thesis, novel metal combinations, such as ultrathin metal bilayer, are studied to replace ITO, which is still a bottleneck for the introduction of organic devices into the mass market due to its high cost and high process temperature, which is not compatible for the deposition on flexible substrates such as PET. ITO is a high cost material composition based on rare indium(III) oxide (In_2O_3) *and tin(IV) oxide* (SnO_2)*. Another disadvantage of ITO, looking at the device structure, is that most of the light is trapped inside the device due to the need of a relatively thick ITO layer as transparent bottom electrode. Various approaches for an improved light outcoupling have been proposed and successfully applied into the OLED structure [15]-[18]. Indeed, most of the presented solutions still use ITO as anode material with either a modified surface or capped with an additional metal layer. The study in chapter 3 addresses some of the approaches in this area, such as OLED manufacturing with low cost alternative semitransparent and highly conductive substrates [19]. Nickel (Ni) is widely studied as an ultra-thin layer in terms of transmittance, conductivity and morphology and then Ni is applied as anode material for OLEDs. Ni-OLEDs show reasonable efficiencies at a comparable brightness, in respect to the ITO reference device. It is demonstrated that pure Ni is very stable against temperature and humidity. Better electrical and optical properties can be measured for pure copper (Cu), however, it shows poor stability during environmental tests (humidity and temperature). An excellent trade-off between the Ni-stability and the optical and electrical properties of Cu is found by forming a double-layer based on Cu and Ni. The bilayered CuNi ultra-thin metal films (UTMF) show excellent stability against temperature and oxidation. When applied to OLEDs, the devices show high efficiency, almost as good as ITO-based devices with good operation stability over time. Thus, it is shown that Ni and NiCu are potentially better candidates as semitransparent anode material for OLED applications due to easy fabrication, use of low cost material, low material consumption and a reasonable OLED efficiency.*

A growing research and industry interest on solution processed OLEDs can be noticed despite the fact that the performance has not reached the one of vacuum deposited devices. However, solution processed OLEDs can be fabricated via different printing techniques. In the future, *it might be even possible to use roll-to-roll (R2R) processes on a continuous web, similarly to the printing process of newspapers. Such R2R-process tools include usually a Slot Die and/or Inkjet print-system for the deposition of the electrodes and the active material. The R2R process would decrease significantly the cost of the OLED fabrication, which could make OLED a serious competitor of lighting and display technologies. Small molecules became printable and the replacement of the commonly vacuum deposited electrodes with printable materials encourages the industrialization of solution processed OLEDs. A particular challenge of solution processed OLEDs is the preparation of multilayer devices. A concept for the preparation of solution processed multilayer devices is presented. The insertion of thin A2O3 layer prepared by atomic layer deposition protects the organic layer on the substrate against the solvent used in the deposition of the subsequent layer. [22]. Specifically, within this study,* Alq_3 *as electron-transport material is spin-coated onto an* Al_2O_3 *protected emissive polymer layer. The brightness of the device is furthermore significantly enhanced due to the presence of the electron transport layer and the avoided dissolution of the emissive polymer. This study proves successful the concept behind this idea and a further enhancement of the OLED efficiency can be very likely achieved by choosing a different material combination. However, such a process shows again the importance of the ALD-process integration into a R2R process due to its extended range of processing possibilities. The application of the ALD is therefore not only limited to the encapsulation process when used for organic electronics.*

Avoiding the intermixing of materials for solution processed multilayer structures is one of the main approaches in chapter 4. However, a careful intermixing of two or more polymer materials might lead also to an increase of the host polymer performance when choosing a proper guest-host relation. Usually an emissive hole-conductive host polymer is blended with a non-emissive electron conductive guest polymer [20]. In chapter 5, a different approach is presented based on an emissive polymer as host material doped with an emissive small molecule. MEH-PPV and Alq_3*, both emissive materials and commercially available, are blended successfully together without changing the emission spectra of MEH-PPV as host material. The energy transfer of MEH-PPV doped with* Alq_3 *varying the concentration is investigated in this chapter and such a blend is successfully applied as emissive layer into an OLED structure. Both concepts, the use of multilayer structures (chapter 4), and the blending of the host material are compared. The same emitter, MEH-PPV, is used and* Alq_3 *is either spin-coated or used as dopand. Both concepts show a significant increase of the OLED efficiency compared to the MEH-PPV reference OLED.*

The blended OLED shows still a higher efficiency and lower required voltage for the maximum light emission. Blending of the host with a charge carrier emitter shows a significant advantage compared to multilayer structure, due to lower process cost, since less process steps are needed. Furthermore, a multilayer device fabrication requires additional process steps (for instance, cross-linking or protection layer) to avoid intermixing of the solution processed layers.

Chapter 2

Fundamentals and experimental details of organic light emitting diodes (OLEDs)

Understanding the physics and process requirements of semiconducting polymers are crucial for the successful implementation of the polymer as emissive layer in (OLEDs). The fundamentals of conductive polymers as well as their optical and electrical characteristics are explained in the following chapter. The fabrication techniques used in this thesis are described and the process recipes are listed.

2.1 Theoretical background of organic light emitting diodes

Semiconducting conjugated polymers have attracted much interest recently. These materials combine the processability and outstanding mechanical characteristics of polymers with the ready-tailored electrical and optical properties of functional organic molecules. The electronic characteristics of these materials are primarily governed by the nature of the molecular structure, but intermolecular interactions also exert a significant influence on the macroscopic material properties. Polymer light emitting diodes consist of a stack of layers where an electrically excited fluorescent polymer is sandwiched between two conductive electrodes. At least one of the electrodes has to be transparent for the outcoming light; this can be either the anode or the cathode depending on the OLED configuration (standard or inverted). A simple OLED stack is shown in figure 2.1a with an emissive polymer sandwiched between two electrodes. A photograph has been taken and is shown in figure 2.1b from a fabricated working device. This device is the so-called bottom-light emitting diode configuration, meaning that the top-electrode (cathode) is opaque, so that the emission of light takes place through the glass substrate.

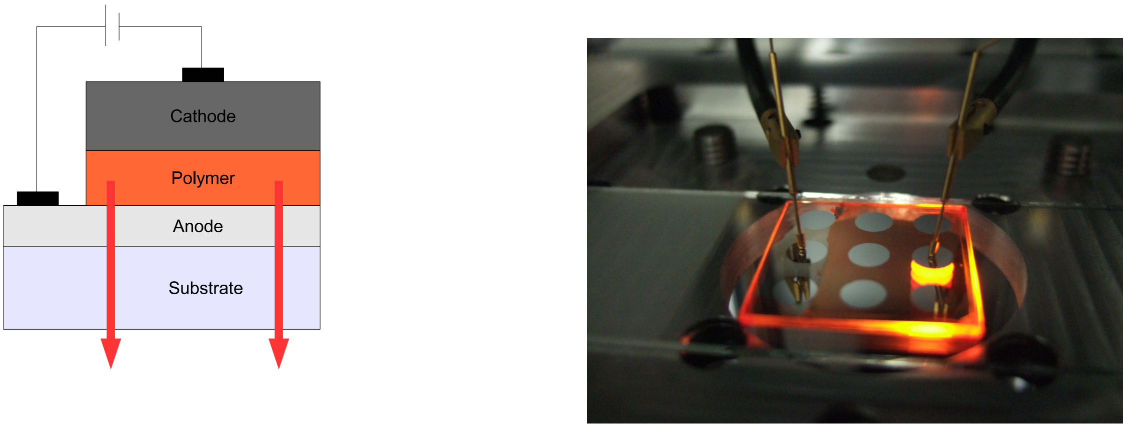

(a) (b)

Figure 2.1: a simple OLED stack (a) can be electrically excited for light emission (b)

A successful electrical excitation requires the injection of charges, the transport through the layers as well as a balanced amount of positive and negative charges within the active emissive material resulting in an effective formation of excitions for the radiative recombination. The following subchapters give an insight of some of the fundamental processes within the OLED structure.

2.1.1 Fundamentals of organic semiconductors

When two atoms interact to form a molecule, they form a chemical bond either by creating a bonding molecular orbital or an antibonding molecular orbital. A bonding molecular orbital is formed when the wavefunction of the two reacting electrons is in phase; an antibonding molecular orbital will be created when the wavefunction is 180° displaced forming a nodal point (amplitude = 0). Orbitals that lie along the bond axis are called σ-bonds and are very strong and highly localized in space. They do not allow mobile charge carriers and are largely responsible for the shape and the structure of the molecule. The π-bonds lie above and below the plane of the polymer backbone, are spatially delocalized over the entire conjugated segment, and are much weaker [21]. Electrons in the π orbital make this particular class of organic materials conductive. A π-bond and a σ-bond can form a double bond resulting in the formation of a combined orbital, the so-called molecular orbital. Normally, the highest occupied and lowest unoccupied molecular orbitals (HOMO and LUMO, respectively) in organic semiconductor molecules are π orbitals. The energy difference between the HOMO and the LUMO is then regarded as band gap energy with a typical energy between 1.5 eV - 3 eV [22][22], as schematically shown in figure 2.2. Therefore, the HOMO corresponds to bonding π and LUMO to anti-bonding π^* orbitals which have higher energy. In a simplified analogy, the HOMO and LUMO levels are to organic semiconductors what valence and conduction bands are to inorganic semiconductors. By adding more conjugated double bonds into the system, more molecular orbitals will be created leading to a decrease of the energy gap between the highest occupied molecular orbital (HOMO) and the lowest unoccupied molecular orbital (LUMO). As a result, light with a longer wavelength will be absorbed.

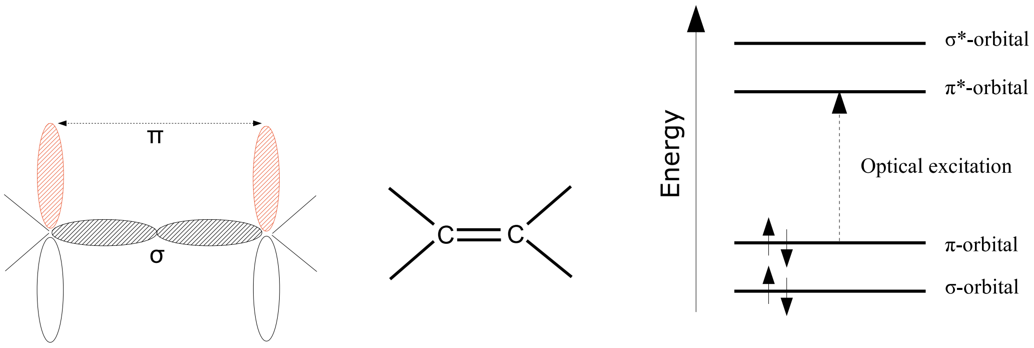

(a) (b)

Figure 2.2: molecular orbital of Ethylene (a) and the corresponding band splitting (b)

A consideration of the HOMO and LUMO level is mandatory for a well-balanced injection of positive and negative charges when using conjugated polymers in OLED devices. The electrodes (anode and cathode) are usually defined by the workfunction which should be aligned to the HOMO and LUMO level. Assuming a proper injection and transport of the charges towards the polymer center, an exciton (a bounded state of an electron and a hole) will be formed creating an excited state. Indeed, two processes are in charge of the formation of an exciton. The first process is also known as Langevin recombination where an exciton is formed due to the recombination of an electron-hole pair. This recombination mechanism is dependent on the injection and the transport of the charges and is more efficient for a well-balanced number of positive and negative charges. The second process is related to the photon absorption via optical excitation where an electron of the ground state will be excited towards the HOMO molecular orbital. For both processes, the excited molecule keeps this gained energy for a very short time, approximately 10^{-9} to 10^{-7}s until it falls back to the ground level by releasing its energy.

The Jablonski-diagram (figure 2.3) illustrates the electronic states of a molecule and the transitions between them. The singlet ground state S_0 and the excited singlet states S_{n+1} with n > 1 as well as the triplet states T_1 and T_2 are shown in the diagram. The ground state can only be a singlet state regarding Paulis exclusion principle. Therefore, only the singlet state can be excited via photoabsorption. The excitation of an electron from the ground state S_0 by photoabsorption generates an excited state in S_{n+1} with n > 1 [24]. The radiative recombination from S_n to S_0 is known as fluorescence. A radiative decay from the triplet state to the ground state is spin forbidden. Such a radiative decay is called phosphorescence and has a much smaller recombination rate than for the fluorescence [22][29].

However, the emission probability for each molecule is time-independent and the emission intensity depends in fact only on the number of molecules in the excited state. The ideal exponential decay of the fluorescence intensity of the excited molecule can be described with the following law:

$$I = I_0 e^{-k_0 t} \tag{2.1}$$

I_0 and I describe the intensity of the emitted radiation directly after the excitation and after passing the time t. k_0 is known as velocity constant and can be calculated from the average lifetime of the excited state (equation 2.2).

$$k_0 = \frac{1}{\tau_0} \tag{2.2}$$

The lifetime τ_0 is almost temperature independent, but it depends on environmental conditions and also the used solvents. The estimated value for the rate constant for the fluorescence is between $k_F = 10^6 - 10^9\, s^{-1}$. The phosphorescence process is forbidden by nature so that the velocity constant with $k_P = 10^{-2}$ - $10^4\,s^{-1}$ is much smaller than for the fluorescence [26].

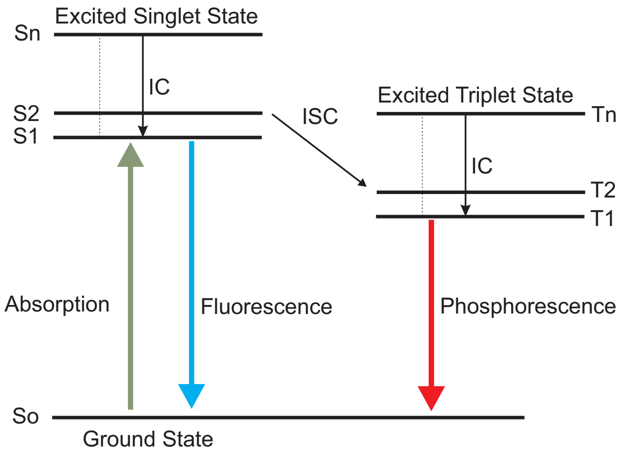

Figure 2.3: energy transfers and recombination mechanism explained by the Jablonski diagram

The electrical excitation is different from the photoexcitation and involves basically the charge transfer and the diffusion of the electrons and holes in the polymer material until they are attracted by their mutual coulomb force and recombine either to form a singlet or a triplet state. The 3:1 law occurs in that case where many more triplet states are formed and the intersystem crossing from singlet to triplet can still happen. The internal conversion (IC) is the transfer with the same spin-multiplicity. Such a non-radiative transition occurs between higher excited states S_{n+1} to S_1. On the other hand, electron transfer between states of different multiplicities via spin-inversion is called intersystem crossing, which is basically the conversion from the triplet state to the singlet state or vice versa [25]. Only 25 % of all excitons created in this described way are singlets and 75 % are triplets according to the quantum mechanical rules (also known as 3:1 rule) which limits the internal quantum efficiency of OLEDs. The limitation of the internal quantum efficiency is due to the low probability of a radiative recombination of triplet excitions. Therefore, only the radiative recombination of singlet excitons contributes to the emitted light [21]. The electroluminescence efficiency is normally lower than the photoluminescence efficiency since not all the injected holes and electrons recombine to form excitons and only a fraction of these are in the singlet state [27].

The presence of molecules from different species might lead to either a fluorescence enhancement or a fluorescence quenching due to the possible energy transfer between the molecules. The presence of a donor molecule might result in a change of the polymer chain aggregation of the host polymer. It has been described that MEH-PPV chains are expected to coil more tightly in $CHCl_3$. The figure 2.4 just illustrates the possible influence of the Alq_3 dopand on the MEH-PPV aggregation. The size of the MEH-PPV (hydrodynamic radius) has been reported to be between 10 and 30 nm depending on the solvent and on the molecular weight, whereas the size of the small molecule Alq_3 is around 2 nm. The energy transfer between the acceptor (in the presented case MEH-PPV) and the donor (in this example, Alq_3) becomes more dominant for a high donor concentration compared to the energy transfer between polymer chains from the same species. Such an energy transfer might lead to a significant emission enhancement when the molecules (donor and acceptor) are properly chosen. A schematic example for the donor and acceptor behavior is shown in the following figure:

(a) MEH-PPV polymer chains

(b) MEH-PPV doped with Alq_3

Figure 2.4: MEH-PPV polymer chain with schematically shown interchain energy transfer (a), MEH-PPV doped with Alq_3 and the corresponding energy transfer between the polymer chain and the molecules.

The energy transfer of the excitons in figure 2.4 is indicated as red arrows. Excitons can transfer energy from an excited donor species D^* to an acceptor species A. In that case, a non-radiative energy transfer may occur, the so-called Förster transfer or the Dexter transfer [28][29]. The principle is schematically shown in figure 2.5.

An explanation for the energy transfer by the Dexter process can be found for a very short distance in the order of 10 Å or below with a significant overlap of the molecular orbitals. The Dexter process is based on the electron exchange between the donor and the acceptor with a decreased energy transfer probability for larger distances between them. A strong overlap between the absorption and emission spectrum of the donor and acceptor is not required, however, the exciton energy of the acceptor should be lower than that of the donor molecule for an efficient transfer [26]. The Dexter transfer allows both singlet-singlet and triplet-triplet transitions [30].

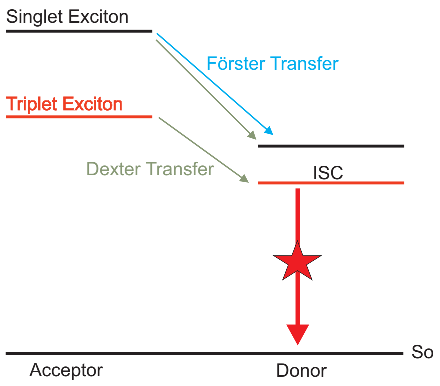

Figure 2.5: schematic of an Förster (long range) and Dexter (short range) transfer

The Förster process explains the energy transfer for an intermolecular distance lower than 100 Å. The excited electrons (donor molecule) act as an oscillating dipole resulting in an alternating electric field which again creates an oscillating dipole in the acceptor molecule. Only singlet-singlet energy transfer is created by the Förster process since the spin state of the donor and acceptor is the same. An example of a strong overlap between the emission spectrum of the donor and the absorption spectrum of the host polymer have been shown in figure 2.6 with an overlap between 450 nm and 575 nm of absorption spectrum of MEH-PPV and the emission spectrum from Alq3.

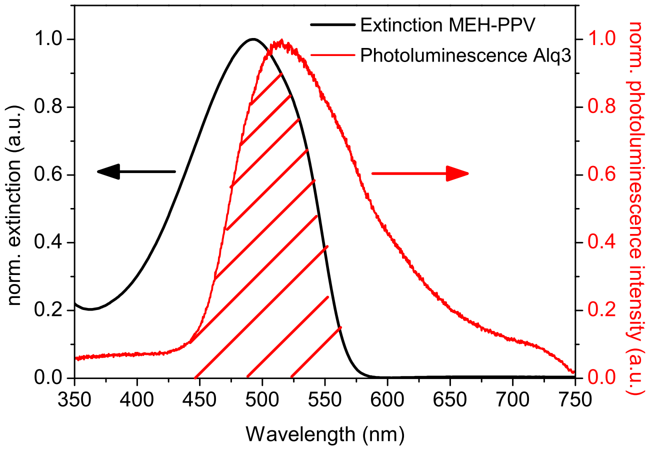

Figure 2.6: absorption spectrum for MEH-PPV and photoluminescence spectrum for Alq$_3$, strong overlap between 450 nm and 575 nm.

If one monomer is in an excited state, the intermolecular interaction is described as excimer. The term excimer refers to the interaction of equal monomers in which one is originally in the excited state and the other is in the ground state. The excited state interaction of different monomers is known as exciplex. Bimolecular excited states can be formed via electron-transfer from donor to acceptor using blends consisting of at least two components. In that case, exciplexes can have either singlet or triplet character dependent on the acceptor. An exciplex is therefore similar to an exciton with electrons and holes on different molecules.

Excimer and exciplex emission is typically broad and unstructured and shifted to lower energies with respect to the emission of the monomer. Both charge-carriers are able to form either excimer or molecular emissive states when injecting holes and electrons via electrical excitation. Therefore the PL and EL spectrum might differ due to the various types of excimer (singlet and triplet) which can be formed via electrical excitation [31]. Note that excimer and exciplex can be observed in both, the PL and the EL spectrum [30][32].

2.1.2 Charge injection and transport processes

The current-voltage characteristic for organic light emitting diodes is characterized mainly by two effects, the injection of the charge carriers from the electrodes into the devices and the charge carrier transport within the device structure limited by the organic material properties. This subsection gives an overview of the commonly applied injection processes of OLEDs and the current voltage behavior defined by its characteristic regions.

Charge carrier injection mechanism

The OLED device performance is strongly related to a balance injection of negative (electrons) and positive (holes) charges. When applying a voltage, negative and positive charges have to overcome the energy barrier between the electrodes and the organic material. This energy barrier is the result of the difference of the metal workfunction and the HOMO or LUMO level of the polymer. Two main processes are involved in the injection of charges, the Fowler-Nordheim tunneling (FN) and Richardson-Schottky (RS) thermionic emission (figure 2.7).

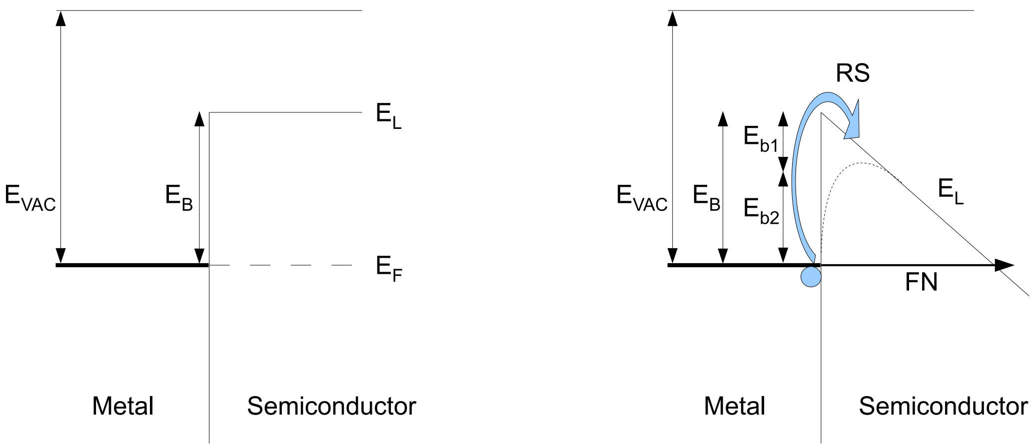

Figure 2.7: metal-semiconductor contact without an applied electric field (a), Richardson-Schottky (RS) and Fowler-Nordheim (FN) injection mechanisms after applying a voltage V with the electric field E (b)

The first model, the FN tunneling mechanism, describes the tunneling principle of charges from the metal electrode through a triangular barrier into the polymer material, independent of the temperature [33]. The triangular potential barrier results from the applied electrical field and the tilt of the energy levels of the semiconductor. The slope of the tilt depends on the electric field strength and thus the barrier width becomes field dependent. In equation 2.3 it can be seen that the injection current is limited by the potential barrier E$_B$ between the electrode and the polymer material and the electric field E [34][35].

$$J_{FN} = \frac{2,2\,(qE)^2}{8\pi h E_B}\,exp\left(\frac{-8\pi\sqrt{2qm^*}\,E_B^{\frac{3}{2}}}{3hE}\right) \tag{2.3}$$

The second mechanism for the injection of charges is known as the Richardson-Schottky (RS) thermionic emission [36][37]. Three effects are important for this model [38]. The first effect is the potential difference E$_B$ between the workfunction of the electrode metal and the LUMO energy level for the electrons of the polymer material. For the second effect, the applied electrical field manipulates the characteristics of the potential, which results in the typical triangular potential barrier. The last effect results from the image potential of the injected charges. The magnitude of the electrostatic force E$_L$ between two point charges can be calculated by coulombs law and is inversely proportional to the square of the distance between the charges. The total potential as a function of the distance is the result of the superposition of those three potentials. The potential difference E$_B$ will be therefore lowered due to the resulting electrical field of the image force. This lowering of the potential is the so-called Schottky-effect. We obtain the total current as the final result. As described by equation 2.4, the current depends on the temperature, the applied electrical field and the lowering of the potential barrier at the electrode-polymer interface through the image force [39].

$$J_{th} = \frac{4\pi q m^* \left(T k_B\right)^2}{h^3} exp\left(\frac{E_{b1} - E_B}{k_B T}\right) \tag{2.4}$$

To summarize, several effects increase the injection of the charge carrier into the OLED when looking at equations 2.3 and 2.4. Increasing the applied electric field increases also the injection of charges due to the lowered potential difference. However, a low applied electric field (low turn-on voltage) is required for commercial OLED application. A key element for tuning the charge carrier injection is lowering the potential difference E$_B$ by aligning the workfunction of the cathode to HOMO energy level of the Polymer for an increased injection of the holes and also aligning the workfunction of the cathode to the LUMO level of the polymer for an increased injection of electrons.

Space-charge-limited current (SCLC) model

The current-voltage behavior curve of the OLEDs can be described with the space-charge-limited-currents (SCLC) model. The SCLC model includes the material properties, the charge-carrier-mobility and also the intrinsic charge-carrier concentration of the polymer semiconductors [40]. Four regions can be distinguished in the I-V curve as it is schematically shown in figure 2.8:

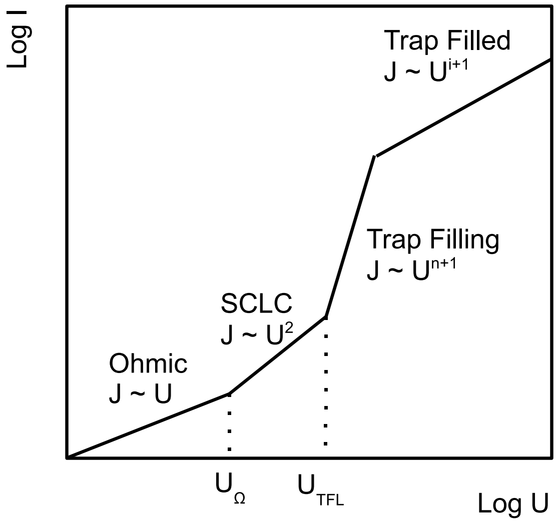

Figure 2.8: current-voltage behavior with traps, ohmic and SCLC transition, with n > i

A perfect single layer device with two symmetric, ohmic contacts, free of traps and a free charge carrier mobility has been assumed. The diffusion current as well as the charge carrier densities at the thermal equilibrium has been neglected in this assumption. The thermally generated free holes override the square law at low electric field where the number of injected holes is quite low. This so-called ohmic region occurs until the average density of injected excess free charges becomes comparable with the thermally generated one. The description of the ohmic region can be found in equation 2.5 [41]:

$$J = q n_0 \mu \frac{U}{d} \tag{2.5}$$

The current density is proportional to the applied voltage and to the thermionic intrinsic charge carrier density n_0. When the applied voltage is high enough, more charge carriers are injected than are present during the transport process within the polymer layer. Taking $x = d$ and $V = V(d)$ and taking into account the boundary condition ($E(x = 0) = 0$), we obtain the current voltage characteristic, also known as the trap-free square law, the Mott-Gurnay square law as described in equation 2.6 [35][36]:

$$J = \frac{9}{8}\frac{\varepsilon\varepsilon_0\,\mu\,U^2}{d^3} \tag{2.6}$$

A perfect organic single layer device is not a realistic object, but the equation 2.6 can be used when the applied voltage is high enough. At high voltages, the total number of injected holes is substantially higher than the total number of empty traps in the material. The number of free charges will be reduced at lower injection levels by the presence of charge traps, which can be impurities or structural defects. Those empty traps will capture a number of free charges and therefore the current through the device will be limited. The characteristic range of voltage where the current abruptly increases is called the trap-filled limit, and U_{TFL} is the characteristic voltage to reach trap filling. The position of this crossover for discrete levels of traps is roughly estimated from the formula in equation 2.7 [41]:

$$U_{TFL} = \frac{q\,p_T\,d^2}{2\varepsilon} \tag{2.7}$$

As the current flow grows with applied bias, the quasi-Fermi level moves closer to the valence band and may eventually cross the energy level of the trap. At this point, the traps will become essentially filled and further injected free carriers will, therefore, not be trapped.

2.1.3 Optical losses within the OLED structure

Optimizing the light extraction of OLEDs is a particular interest in research nowadays. The external efficiency η_{ext} is related to the internal quantum efficiency η_{int} of the organic material and the out-coupling efficiency η_{out} of the multilayer planar structure as shown in equation 2.8:

$$\eta_{ext} = \eta_{int}\,\eta_{out} \tag{2.8}$$

It has been shown that 40 - 50 % of the generated light of the light emissive polymer is trapped within the ITO-layer and/or absorbed as surface plasmon on the metal-polymer interface [42]. Part of the light (20 - 30 %) is totally reflected on the interface between the substrate and air and will be therefore guided to the lateral faces of the device. This part of the light is basically not lost since it can be directed orthogonal to the surface using optical systems [43]. A maximum external efficiency of around 20 - 30 % can be therefore achieved [44].

An OLED stack consists of different organic and inorganic layers with their specific optical properties. The transmission, absorption, reflection as well as the optical coefficient n and extinction coefficient k of these materials are wavelength dependent. A common methodology for optimizing the OLED stack in respect to the emission wavelength of the polymer can be found using the transfer-matrix analysis (appendix C). The optical properties of the OLED stack will be therefore described as a matrix where the wavelength dependence of the optical parameters is considered. The characteristics of the optical properties of each material are given by the complex refractive index which can be described with the following formula:

$$N(\lambda) = n(\lambda) - ik(\lambda) \tag{2.9}$$

The complex refractive index is wavelength dependent and can be either measured for a known layer thickness using the spectroscopic ellipsometry or calculated from the optical properties. A simplified method for the calculation of the complex refractive index n of a thin film with a low absorption has been already described in 1975 by J. C. Manifacie *et.al.*[52]. In this thesis, the refractive index and the absorption coefficient have been calculated from the transmission and reflection measurements. The imaginary part of the index of refraction is related to the absorption coefficient α and the wavelength of light λ, shown in equation 2.10:

$$k = \frac{\lambda\alpha}{4\pi} \tag{2.10}$$

The absorption coefficient can be determined by the optical transmission measurement and the thickness of the measured film. This parameter is also known as optical density (OD) with the following relationship:

$$\alpha = \frac{OD\, ln(10)}{x} \tag{2.11}$$

The incoming light intensity is given by I in equation 2.12:

$$\frac{I}{I_o} = e^{-\alpha x} \tag{2.12}$$

The remained light intensity after passing through a film with a thickness x is named with I_o . Basically, the transmission decay through an absorbing medium has been described in equation 2.12. Using these equations and the Matrix Transfer formulation, the refractive index n and the absorption coefficient k can be calculated over the wavelength and with these results, the out-coupling efficiency can be evaluated under the consideration of losses due to the formation of optical modes within the dielectric stack. Layer thicknesses between a few nm and 150 nm are very common within the OLED stack structure leading to electromagnetic waves or modes; TE - and TM modes. TE-modes: the electric field is transverse to the direction of propagation (no longitudinal electric field component) while the magnetic field has both transverse and longitudinal components (Ez = 0, Hz $\neq$ 0). TM-modes, the magnetic field is transverse to the direction of propagation (no longitudinal magnetic field component) while the electric field has both transverse and longitudinal components (Hz = 0, Ez $\neq$ 0). Various localized intensity maxima of the TE or TM modes might occur due to the difference of the thickness and refractive index for each layer. The out-coupling of such modes can be realized using for example either periodic or non-periodic nanostructures [49]. A simplified OLED structure is shown in figure 2.9.

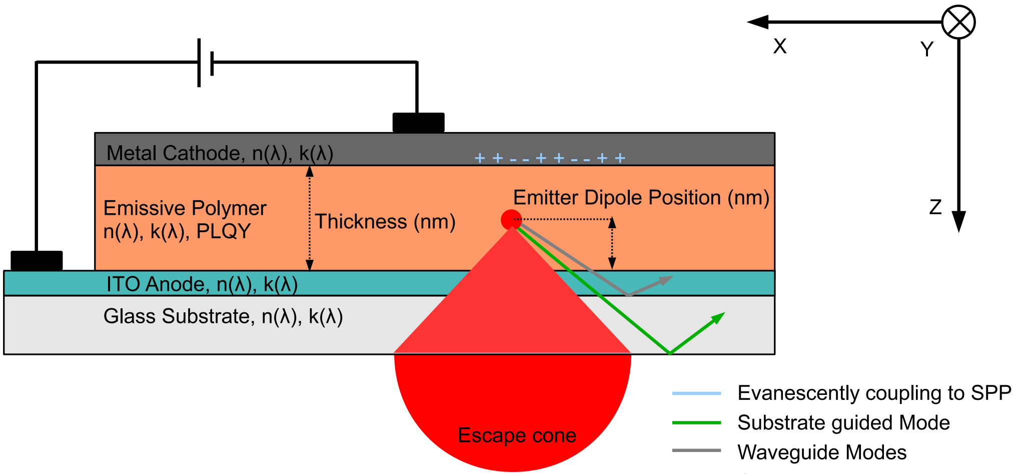

Figure 2.9: The OLED stack consists of various layers with different thicknesses, each of the layers have their unique optical constants n and k as a function of the wavelength. Waveguiding and substrate guided modes are indicated as arrows. The emitter dipole position defines the optical paths for the emitted light and possible losses due to the coupling to the metallic cathode.

The arrows indicate the out-coupling losses due to substrate guided mode (green), waveguiding modes (grey), and power evanescently coupled to surface plasmons and charge density fluctuations (light blue). Additionally losses due to the absorption properties of the organic layers and non-radiative losses (for a quantum efficiency of less than 1) are very likely to occur. Figure 2.10 shows an example of the power fraction of the calculated modes within the OLED stack between 500 and 700 nm using the Setfos 3.3 Software and as a function of the relative emitter dipole position within an emissive polymer with the thickness x ("‘0"’ = metal cathode - polymer interface, "‘1"’ = PEDOT:PSS - polymer interface). The software calculates the outcoupled fraction of the total emitted power by the emitter dipole (red) within the escape cone, as schematically shown in figure 2.9. The graph shows the fractions of the total power, which is outcoupled (red), coupled to substrate guided modes (blue), absorbed in the organic stack (yellow), waveguided modes (violet), evanescently coupled to surface plasmons and charge density fluctuations (light blue), and lost non-radiative, for instance in terms of a PL quantum efficiency lower than 1 (pink). The intensity of the optical modes depends on the thickness of each layer and furthermore the position of the emissive dipole due to its influence on the optical path of the emitted light.

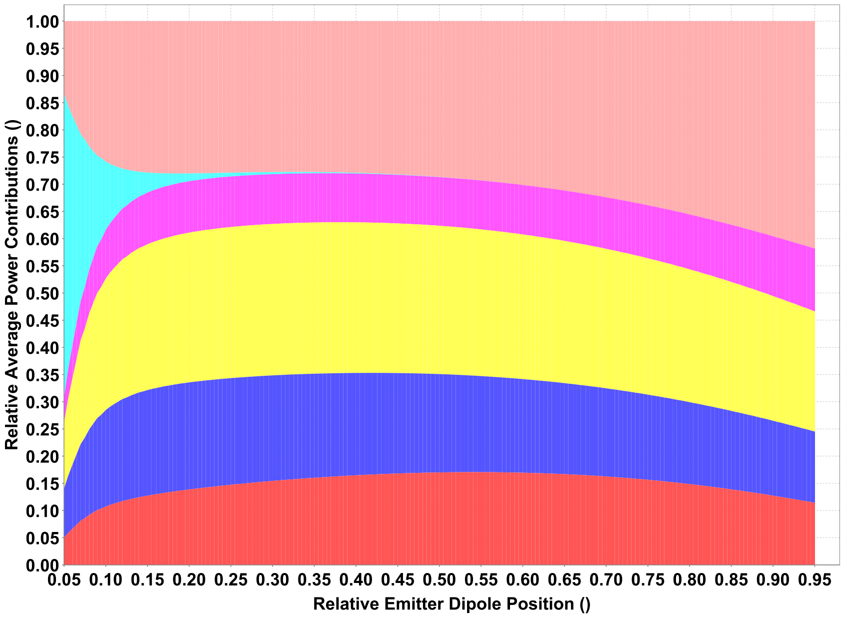

Figure 2.10: Simulated exampled for an OLED device with the following structure; ITO (150 nm), PEDOT (25 nm), emissive polymer (70 nm) and Ag (nm). A PL quantum yield of 75 % for the polymer has been considered for the simulation.

A simulated example for the dependence of the shape and the intensity of the emission spectrum by varying only the thickness of the emissive layer is shown in figure 2.11. Only the thickness of the emissive polymer has been changed and the emission zone has been always kept in the center of the polymer. The calculation of the outcoupled emission spectrum has been done using the Fluxim Setfos emission module with the following results (figure 2.11). It is quite evident that the outcoupling intensity varies depending on the position of the dipole and depending on the stack parameters. Additionally the shape of the emission changes by varying the thickness of the emissive polymer layer (figure 2.11). Looking at the normalized emission, a shift of the emission spectrum is also visible.

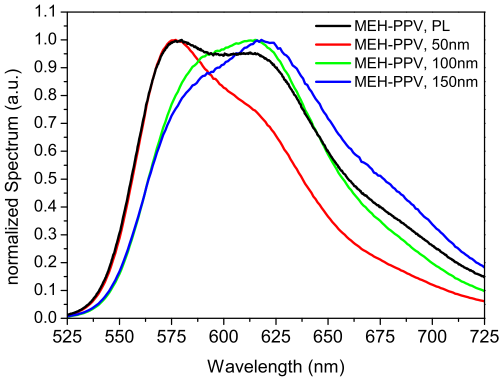

Figure 2.11: outcoupled emission varying the thickness of the emissive polymer MEH-PPV

Therefore, when designing an OLED, it is important to take into account not only the desired electrical properties, but also the optical parameters in order to enhance the light emission due to the improved out-coupling and to guarantee the desired emission spectrum.

2.2 Deposition techniques and processing procedure of OLED devices

The fabrication of OLEDs includes cleaning processes of the substrate, different deposition techniques for the thin organic and inorganic layers such as spin-coating, printing and the evaporation of metals or oxides as electrode or interfacial layer. The atomic layer deposition (ALD) is well known from semiconductor fabrication because of its ability to deposit highly packed and dense oxides in a very controlled process. In this section in particular, the ALD deposition is explained in detail because this technique is going to be extensively used in chapter 4. The fabrication procedure of the different OLEDs devices processed within this research work is described as well.

2.2.1 Atomic layer deposition

The Atomic layer deposition belongs to the chemical vapor deposition and is based on a self-limiting surface reaction. The semiconductor industry is the main motivation for the recent ALD development; however, there is a growing interest for the use of thin ALD deposited oxides as encapsulation layer for organic devices. The ALD thin film deposition technique has been widely used for example for the deposition of high dielectric constant gate oxides in MOSFET structures. The advantage of ALD is the precise thickness control at the Ångstrom or monolayer level. The self-limiting aspect of ALD leads to excellent step coverage and conformal deposition on high aspect ratio structures [53]. ALD can be used to deposit several types of thin films, including various oxides (e.g. Al_2O_3, TiO_2, SnO_2, ZnO, HfO_2), metal nitrides (e.g. TiN, TaN, WN, NbN), metals (e.g. Ru, Ir, Pt), and metal sulfides (e.g. ZnS) [54][55]. An example of the excellent coverage of the ALD deposition is given in figure 2.12.

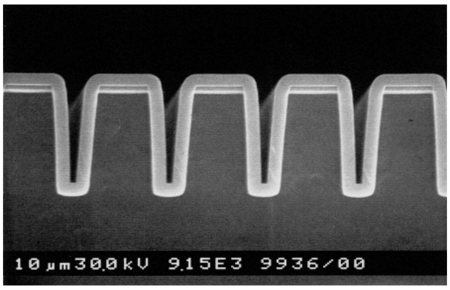

Figure 2.12: SEM image of a 300 nm Al_2O_3 film on a Si wafer taken from reference [56], courtesy of S. M. George

A commercial ALD reactor (the Savannah 300, Cambridge NanoTech) has been used for the deposition of the Al_2O_3 layer. The deposition of a thin ALD layer typically involves basically 4 steps as explained for the deposition of the Al_2O_3. The precursor Trimethylaluminum (TMA) will be injected into the vacuum reaction chamber resulting in a reaction with the available surface groups of H_2O. The self-limiting mechanism prevents further reactions on the surface due to a high amount of precursor and/or due to the purging mechanism. The reaction chamber will be purged by a gas N_2 in the next step for removing all rest-products. After pumping the residues, the second injection of a precursor takes place again resulting in a chemical reaction with the new groups on the surface. Another purging step concludes the ALD cycle, removes all the volatile reaction byproducts and the excess of precursor present in the chamber. After one ALD cycle (including the 4 steps) a monolayer of material is formed onto the substrate surface with identical surface groups so that the same reaction can be started again.

The stabilization of the growth rate depends on the dose of the precursor. Initially the growth rate is very low due to the low injection of the precursor and it increases when more precursor is injected up to the self-limiting character. A stable deposition growth rate requires a very specific temperature window, the so-called ALD window. Lower temperatures lead to higher growth rates due to condensation of the precursor or even lead to lower growth rates due to insufficient thermal energy as a requirement for the surface reaction. In the opposite way, higher temperatures might lead to higher growth rates caused by increased gas phase reaction or eventually to lower growth rates due to the partial decomposition of precursor molecules.

Despite this broad application field, there is still a lack of understanding of the nucleation and growth of Al_2O_3 ALD on polymers. ALD processes can be performed at relatively low temperatures compared to standard CVD processes, thus significantly enlarging the range of applications especially in the field of polymer-based devices. It has been shown that Al_2O_3 can be also deposited at temperatures as low as 30 °C keeping most of the material properties, except the density, which decreased significantly from 3.5 g/cm^3 to 2.5 g/cm^3 [57]. A longer cycle time is required at lower process temperatures due to the slower reaction rate and lower vapor pressure of the precursors. An increased purge is required in order to remove the remaining H_2O in the reaction chamber. The mechanism of the nucleation of the ALD layer has been investigated in several studies, especially when depositing on organic layers [56][58]. J. D. Ferguson *et. al.* observed a migration of $Al(CH_3)_4$ reactant into polyethylene [59]. It has been proven furthermore that the polyethylene particles are covered with an ALD film after 40 cycles. The diffusion effect of the TMA into polymethylmethacrylate (PMMA), polypropylene, polystyrene, polyethylene, and polyvinylchloride during cycling was extensively investigated in the work of C. A. Wilson *et. al.* in 2005 [53]. The diffusion of the TMA is stronger during the first cycles and will be hindered when the ALD begins to form a continuous film. The following picture illustrates the migration of the ALD precursors into the organic layer (figure 2.13a), followed by the partial coverage (figure 2.13b) until the ALD film prevents further migration (figure 2.13c) and finally when a closed dense ALD layer has been grown (figure 2.13d).

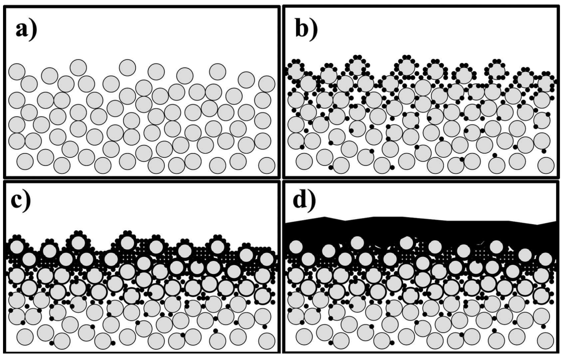

Figure 2.13: Schematic ALD deposition on polymer films, a.) polymer chains at the surface, b.) Al_2O_3 nucleation clusters, c.) growing of a closed ALD film, d.) formation of a dense Al_2O_3 film (taking from [60], courtesy of S. M. George)

The ALD process tool Savannah S300 from Cambridge Nanotech has been used throughout this thesis. The Savannah is known as flow type reactor with a single gas injection and a single outlet through which the reaction gases are pumped continuously. However, such a reactor might also create a non-uniformity of the layer thickness since the gas flow is extremely directional atop the substrate. The process of the atomic layer deposition takes place, as described before, in cycles where each cycle is supposed to deposit 1.1 Å. The recipes for the process and for each temperature are discussed and given by Cambridge Nanotech and shown in table 2.1.

Process	Purge H_2O	Stop	Purge TMA	Stop
80 °C	0.015 s	30 s	0.015 s	30 s
150 °C	0.015 s	20 s	0.015 s	20 s
235 °C	0.015 s	5 s	0.015 s	5 s

Table 2.1: ALD process recipes for Al_2O_3 and one cycle

2.2.2 Measurement techniques

The thickness and the quality of the layers and their morphology and roughness have to be controlled during the fabrication process using profilometer from KLA Tencor Alpha-Step IQ and atomic force microscopy (AFM) from digital Instruments, Dimension D 3100S-1. The profilometer is used to measure the thickness of the layer and to evaluate the quality, in terms of roughness. In the case of the AFM, a tiny silicon needle is mounted on the cantilever. A deflection of the needle takes place too and it is measured by a piezoelectric crystal. The AFM analyzes the roughness as well as the morphology of the deposited layer. The AFM provides a true three-dimensional surface profile allowing to obtain high resolution images, without requiring any special treatments of the surface (such as metal/carbon coatings) that would irreversibly change or damage the sample. The values for the roughness should be as low as possible in order to avoid short circuits between layers and to obtain a uniform layer.

The optical properties of the organics are obtained by performing photoluminescence, absorption, reflection and transmission measurements. The optical bandgap of the polymer can be obtained by measuring the absorption spectrum. Once this is known, the polymer can be excited at the exact wavelength in order to obtain photoluminescent light emission. Such measurements are also very important when trying to characterize polymer blends where optical interaction might take place between the two entities of the blend. An example for this will be discussed in chapter 5. Photoluminescence measurements (PL) were done using a setup from an Olympus Microscope (model BX51M). Various filters were used to select the specific wavelength regime of the white light source. This wavelength regime corresponds to the specific absorption spectrum of the polymers used in this thesis. The emitted light was then collected through an objective with 50 x magnification, then into an optical fiber coupled to a HR2000 spectrometer from OCEAN OPTICS. An example of a photoluminescence and absorption spectrum is given in the following example in figure 2.14:

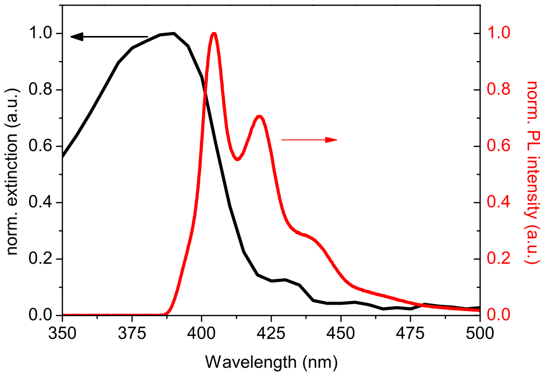

Figure 2.14: example of an optical absorption and photoluminescence spectrum

Transmission, reflection and absorption measurements have been used in combination with the layer thickness for the calculation of the complex refractive index N = n - ik. The measurements have been performed using the Varian Cary 5000 UV-Vis-NIR spectrometer with an attached Ulbricht sphere for the measurement of the total emission.

An important parameter for light emitting organic materials is their quantum efficiency (quantum yield), which is given by the ratio of the number of emitted photons to the number of photons absorbed by the material. The quantum yield measurements were performed using the quantum yield measurement system (C9920-02 from HAMAMATSU), for spin coated organic layers on quartz substrates. The system is made up of an excitation light source that uses a xenon lamp and a monochromator, an integration sphere and a multi-channel spectrometer. The integration sphere is basically a hollow spherical cavity where the inside is covered with a diffuse reflective coating. A detector which is attached on the sphere measures the emitted light without the effects of beam shape, incident position and incident direction.

Electrical characterization allows to obtain the efficiency or performance of the fabricated devices. The light intensity of a light source as perceived by the human eye is included when referring the luminous intensity (photometric unit) measured in candela (cd). The maximum spectral intensity of the human eye is described with 555 nm under daylight and shifts to 507 nm under night light. Candela is a base unit defined as: a monochromatic light source emitting an optical power of (1/683) W at 555 nm into the solid angle of 1 sr, which has a luminous intensity of 1 cd. The luminous flux (known as the light power) is measured in lumen (lm) as is defined as: a monochromatic light source emitting an optical power of (1/683) W at 555 nm has a luminous flux of 1 lm. This means that 1 cd equals 1 lm/sr. An isotropic emitter with a luminous intensity of 1 cd thus has a luminous flux of 4π lm. Furthermore, the luminance of an OLED (any surface source) is defined as the ratio of the luminous intensity in a certain direction divided by the projected surface area of that direction (cd/m^2).

An example of the measured current density and luminance as a function of the applied voltage is shown in figure 2.15a. The efficiency of the measured OLED can be then calculated from the current density and the luminance (2.15b).

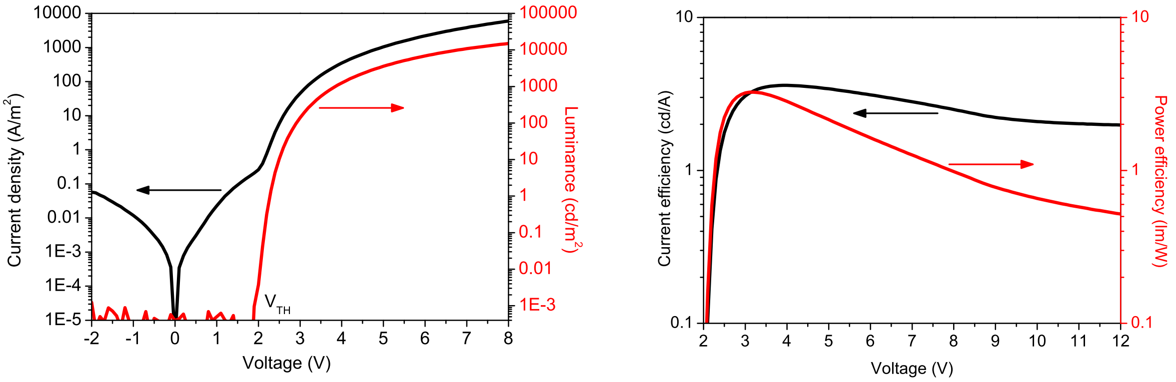

(a) (b)

Figure 2.15: I/V and L/V characteristic (a), current and power efficiency (b)

The electrical characterization was done in a glove box system to protect the OLED from air as the devices are not encapsulated. The devices were measured with a Keithley 236, 237 Source Measure Units and a photodiode coupled to a Keithley 6485 picoampmeter, using a luminance meter Minolta LS100 to calibrate the photocurrent. Two needles were contacted with the anode and the cathode of the OLED and a voltage between -2V up to 20 V was applied. Both, the current density (A/m^2) and luminance (cd/m^2) versus voltage curves were measured simultaneously. The threshold voltage V_{TH} is defined as the voltage where the OLED starts to emit light (see figure 2.14a).

The electroluminescence spectrum was measured with a HR2000 spectrometer from OCEAN OPTICS. The optical simulations have been performed using the emission module from Fluxim Setfos package 3.3. All the materials used in this thesis have been characterized by their transmittance and reflectance. The measured characteristics have been used for the calculation of the refractive index n and absorption coefficient k using software developed by the University of Potsdam (department Prof. Neher). The calculated constants have been included in the material database of the simulation software. The software uses an algorithm based on the transfer-matrix formalism for the simulation of the optical properties of the stack (see appendix).

Chapter 3

Ultra Thin Metal electrode for OLEDs

Nowadays ITO is widely used in research and industry as a semitransparent conductive electrode material for OLEDs and solar cells. A semitransparent conductive electrode material requires a low sheet-resistance, a high transmittance in the visible light spectrum, a work function, suitable for efficient charge injection. Fulfilling such requirements is complicated and although ITO achieves most of them, it has also many drawbacks. It is well known that most of the light is trapped inside the ITO layer which makes the light-outcoupling less efficient. Furthermore, ITO contains indium, which is a rare and expensive material. The deposition on flexible plastic substrates is problematic since ITO requires temperature treatments higher than 400 °C for achieving a low sheet-resistance and high transmittance. Typical plastic substrates cannot be treated at temperatures as high as required to achieve high quality ITO. Flexible substrates require mechanically stable materials, but ITO is brittle and breaks upon bending. Using flexible transparent substrates, however, is a strong motivation for the commercialization of OLEDs.

Various types of doped oxides which do not contain cost intensive indium have been recently investigated; among them, aluminum doped zinc oxide (AZO) [66] and gallium doped zinc oxide (GZO) [67], which have promising material properties in terms of electrical conductivity, transmittance, sheet resistance and the same efficiency has been reached as for ITO-based OLEDs [68]. The light trapping mechanism [61], derived from the difference in refractive index between the polymer/ ITO layer and the glass substrate, has been lowered through various approaches. Nano-imprinted [62], nano-structured layers [62][63] or micro-lenses [64] have been shown to decrease the high refractive index of the ITO resulting in an increased outcoupling [65]. Oxide *based electrodes have to be relatively thick due to the required low sheet resistance. However, using thick layers usually leads to a lower outcoupling efficiency. As proposed by a number of research groups [69][70][71], carbon nanotubes (CNTs), when processed as thin films, are suitable for replacing ITO in OLED technology for flexible applications, because CNTs hold key properties such as flexibility and transparency. Overcoming the relatively high sheet-resistance, reproducibility and the quite complex surface functionalization is a focus of the research nowadays. A complete oxide and indium free anode has been proposed by Meiss et al [72] where a multilayer contact made of ultra-thin thermally evaporated Al and Ag films was used for organic solar cell application with an achieved efficiency up to 2.2 % . A solution for an ITO and TCO free device was presented by H. Peng et al [74] where they proposed a simple thin silver (Ag) layer as semitransparent anode contact.*

Ni as ultra-thin metal for optoelectronic applications has been developed [75]. It was shown that a similar device performance can be obtained when using Ni as anode material instead of ITO [76], even though the transmittance of the ultrathin Ni layer is poor when compared to ITO. A further improvement in terms of transmittance and sheet resistance for the metal anode has been obtained when using Cu capped with Ni, combining the low sheet-resistance and high transmittance of Cu with the high work-function and stability of Ni [77].

3.1 Experimental details

For the OLED fabrication, glass plates either covered with Indium-tin-oxide (100 nm ITO with 13 Ω/sq, Labor für Bildschirmtechnik, University Stuttgart) or metal such as Ni, CuNi, Cu (ICFO, optoelectronic group led by V. Pruneri) were cleaned for 10 min in Methanol using an ultrasonic bath. The deposition was performed with a DC voltage sputtering machine Kenosistec Dual Chamber at room temperature and in pure Ar atmosphere on double-side optically polished UV grade silica substrates. In all cases a DC power of 200 W and a pressure during deposition of 8 x 10^{-3} Torr have been used. The thickness was calculated based on the deposition rate, which in turn was determined by an MCM-160 quartz crystal. The resulting deposition rate for the single Ni layer was 1.6 Å/s. The deposition rates for the CuNi double layer were 1.5 and 0.57 Å/s for Cu and Ni, respectively. Afterwards, the samples were first rinsed in water, then dried with Nitrogen and finally heated and dried for 10 min at 120 °C. The samples were exposed by an ozone treatment for 10 min just before the deposition of the PEDOT:PSS (Clevios P VP

Al 4083) hole injection organic film. The measured thickness of the PEDOT:PSS layer was 25 nm using a spin-coating recipe with no ramp time and 6000 rpm for 40 s followed by a postannealing process for 30 min at 120 °C. Two polymers (SY and PFO) as emissive layer have been sandwiched in the device structure, while the transparent conductive bottom electrode material has been varied. Poly(phenylenevinylene) co-polymer (SY), from MERCK, was dissolved in Toluene (5 mg/ml) and stirred overnight. Poly(9,9-dioctylfluorene) (PFO) was purchased from H. W. Sands and dissolved with a concentration of 7 mg/ml chloroform ($CHCl_3$) and finally filtered with a 1 μm filter. The samples spin-coated with SY were additionally heated for 10 min at 120 °C due to the higher boiling point of Toluene (111 °C). The spin-coating recipe and the corresponding thickness vary depending on the concentration and material used. The recipes are summarized in table 3.1.:

Polymer	Concentration	Solvent	Spincoating Recipe	Thickness
PFO	7 mg/ml	$CHCl_3$	-/1500/20	70 nm
SY	5 mg/ml	Toluene	-/2500/20	80 nm

Table 3.1: Polymer solution concentration, spin-coating recipe and resulting thickness

Different electrodes have been used in this study. Thermally evaporated (<5 x 10^{-6} mbar) Al or CaAg films (100 nm) were used as single or double layer cathodes for the devices. A shadow mask with a circular electrode has been used (12.6 mm^2). The following device architectures have been used in this chapter:

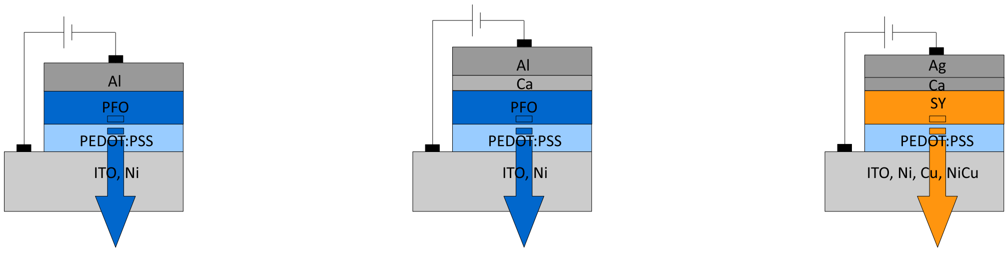

(a) (b) (c)

Figure 3.1: (a) Variation of the Ni thickness for PFO-based OLEDs, (b) with PFO and Ca as electron injection layer and (c) SY-based OLEDs with ITO, Ni, Cu, CuNi as anode (thickness of 8 nm)

3.2 Characterization of the ultra thin metal electrodes

Metal films as bottom electrode contacts have excellent electronic properties due to high conductivity. Metals can be easily processed and patterned by various techniques. Despite all advantages, metal films with a thickness of only 20 nm are mostly opaque. L. Martínez *et.al.* [78] demonstrated that ultrathin-Ni films show promising results in terms of film continuity and sheet-resistance, although the transmittance was lower than for the ITO. In this section, the ultrathin Ni-films have been studied in detail and applied as semitransparent anode in OLEDs. Four different deposition times for the Ni process were chosen in this section and the resulting thickness was calculated from the deposition rate and the deposition time; 6 nm (75 s), 7.2 nm (90 s), 8.5 nm (105 s), 9.5 nm (120 s). The conductivity and transmission of ultrathin Ni-films have been compared to those of commercially available ITO. The sheet-resistance is shown as a function of the Ni thickness in figure 3.2.

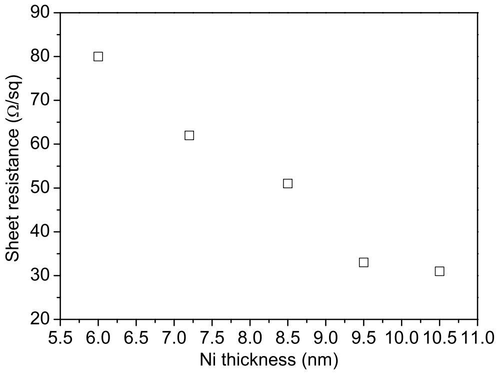

Figure 3.2: Sheet Resistance vs. layer thickness of the Ni layer (Courtesy of D. S. Ghosh)

The sheet resistance was higher for the best Ni-film (30 Ω/sq) than for ITO (14 Ω/sq) [78] film. It can be also seen that the sheet resistance is lower for thicker Ni layers. The sheet resistance is analogous to resistivity when using a three-dimensional system with a planar current flow. The resistance can be therefore written as shown in equation 3.1:

$$R = \frac{\rho L}{t W} = R_s \frac{L}{W} \tag{3.1}$$

where R is the resistance, L is the length, t is the thickness and W refers to the width of the cross sectional area. A common term for the definition of the electrical properties is Ω/sq, which is dimensionless and is exclusively used for sheet resistance (with L = W and R_s = R) [79]. The transmittance and reflectance of Ni layers with a thickness of 8.5 nm and 9.5 nm have been compared with the reference 100 nm thick ITO layer as a function of the wavelength (figure 3.3).

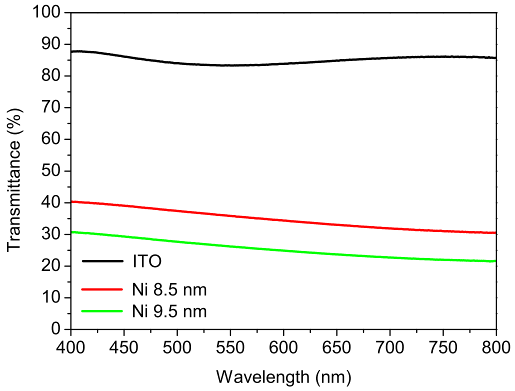

(a)

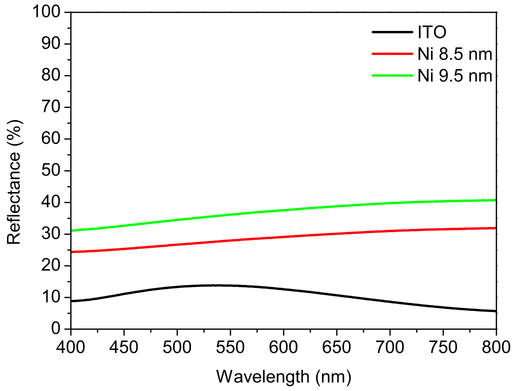

(b)

Figure 3.3: Transmittance (a) and Reflectance (b) for ITO (100 nm) and Ni films (thickness 8.5 nm and 9.5 nm) as a function of the wavelength deposited on 1.1 mm corning glass

A lower transmittance over the visible light spectrum with a slight increase for shorter wavelengths was measured for the Ni-films compared to ITO. In figure 3.3b the results of the reflectance measurements with higher values for the Ni are shown. In chapter 2.1.3 it has been explained that most of the light is trapped within the OLED stack due to internal reflection and the different dielectric constants of the materials used. It is therefore mandatory to keep the reflectance of the semitransparent electrode as low as possible so that the outcoupling of the light is not hindered [80].

The surface roughness has to be kept below the thickness of the layer, otherwise films could be discontinuous and thus non-conductive. Impurities and contaminants are likely to be the most important source of defects. The fabricated Ni thin layers were characterized by atomic force microscopy (AFM). The analysis revealed that the surface of the Ni layer is homogeneous and flat for all thicknesses (figure 3.4). In general, the roughness of the Ni layer increases with thickness and is for each film thickness higher than that of ITO, which is around 0.5 nm.

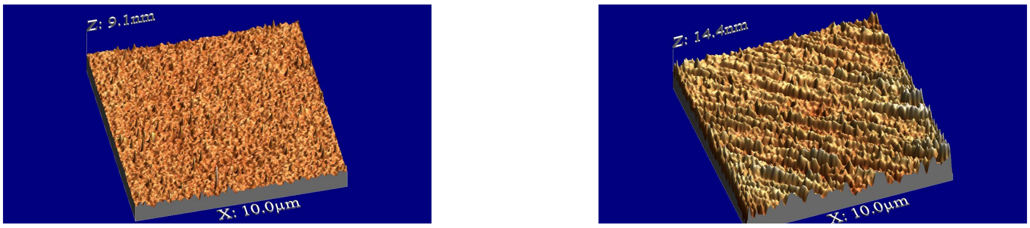

(a) (b)

Figure 3.4: AFM pictures from ITO (a) and Ni = 9.5 nm (b)

The measurement of the work-function of the Ni films was also carried out and listed in table 3.2. A work-function of 5 eV for the ITO film and a work-function of 5.4 eV for the 6 nm and 5.1 eV for thicker layers have been measured by ultraviolet photoelectron spectroscopy (UPS). Hung *et. al.* demonstrated that the workfunction might change for ultrathin metal film due to the irregular islandic growth of metals. The workfunction for layer thicknesses close to the percolation thickness of around 2 - 5 nm differs therefore, compared to the continuous film [81], which explains probably the higher workfunction of the lowest Ni thickness. The percolation of metals ranges between 2 and 6 nm depending on process and process conditions. Another explanation has been found for double metal layers [82] The dependence of the workfunction has been attributed to interfacial issues due to resistivity differences of the metallic films. This is even more significant in the case where the film thickness is close to the percolation thickness.

Material and Thickness (nm)	ITO (100)	Ni (6)	Ni (7.2)	Ni (8.5)	Ni (9.5)
Transmittance (%)	86	40	35	31	29
Rs (Ω/sq)	14	80	62	51	33
$\varphi = \frac{T_{Av}^{10}}{R_S}$	15.8 x 10^{-3}	1.31 x 10^{-6}	0.44 x 10^{-6}	0.16 x 10^{-6}	0.13 x 10^{-6}
Workfunction (eV)	5.0	5.4	5.1	5.1	5.1
RMS (nm)	0.5	not carried out	1	1.5	2.2

Table 3.2: Mean optical transmission and sheet resistance with deposition time of the nickel films. The Haacke figure of merit was calculated from the average transmittance and the sheet resistance [83]

The values in table 3.2 show, the best figure of merit for the Ni layer is obtained for the highest transmittance even though the sheet resistance is the lowest. It is therefore important to increase the transmittance to reach a better figure of merit.

To summarize, Ni as ultra-thin metal film shows good material properties in terms of low sheet-resistance and low roughness. The films were shown to be continuous by AFM. Furthermore, it was found that the work function matches quite well the workfunction of the commonly used ITO electrode material. The transmittance is constant in the visible spectrum although the transmittance is lower than for the ITO. The reasonable electrical properties of the ultra-thin Ni film might be useful for the application of such metal films as semitransparent electrode for OLED application even though the transmittance is rather low. The outcoupling efficiency depends on both, the transmittance and the thickness of the layer. The single Ni layer is therefore applied as conductive and semitransparent electrode in the following subchapters in order to investigate the influence of the UTMF on the outcoupling and finally on the overall OLED performance. Further work is conducted in the subchapter 3.4 to decrease the sheet resistance and to increase the transmittance.

3.3 Nickel UTMF as bottom anode for OLEDs

The UTMF-Ni layer was characterized in the previous section and is applied as semitransparent electrode material in bottom-emitting OLEDs in the following section varying the thickness of the Ni-film. The OLEDs were optimized further, depositing a commonly used electron injection layer (Ca) between the polymer and the cathode. OLEDs based on blue (PFO) and red (SY) emitting polymers were fabricated and characterized.

3.3.1 Influence of the Ni layer thickness on the performance of OLEDs

The variation of the electrical and optical properties with the thickness of the ultra-thin-Ni layer has been studied in the previous section. Now the influence of the metal anode thickness on the OLED performance has been investigated. Ultra-thin Ni layers have been used as semitransparent anode material in a bottom light emission OLED configuration. The used device structure (ITO,Ni/PEDOT:PSS/PFO/Al) and the corresponding energy levels are shown in figure 3.5.

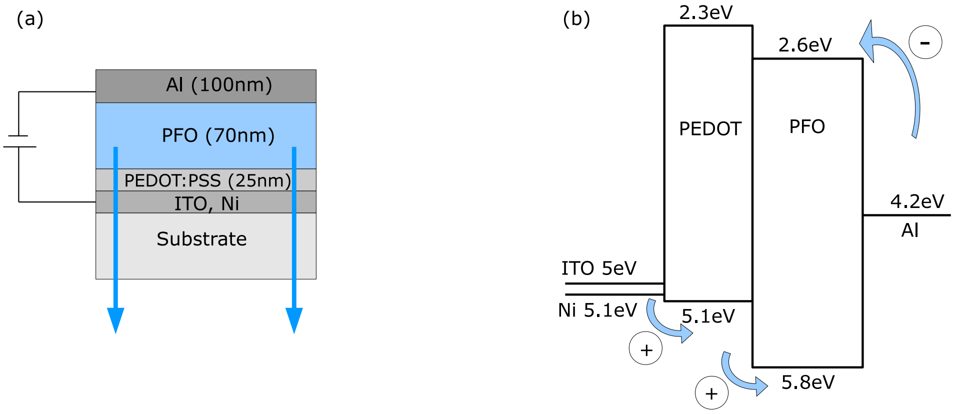

Figure 3.5: OLED schematic (a) and energy band diagram (b)

The device structure in figure 3.5 favors holes as majority charge carrier because of the large energy gap between the Al-cathode and the LUMO level of the polymer. Thus, the injection of the electrons is hindered (figure 3.5b). The device efficiency is therefore expected to be low. As mentioned in the introduction, the main focus of this thesis is to find new concepts (and not to point efficiency records).

Photoluminescence measurements are mandatory in order to check the quality of the spin-coated polymer film and whether the Ni-roughness affects the morphology of the deposited polymer layer. The PL spectra of the ITO and the Ni OLED have been measured at different positions at the device configuration due to the difference in reflectance and transmittance spectrum of the ITO and the Ni. The positions for the measurements are shown in figure 3.6.

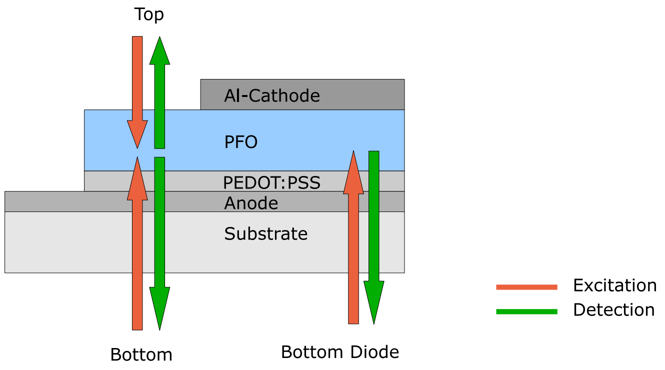

Figure 3.6: Positions of the PL measurements position

The figures 3.7 below show the emission spectrum from the PFO film spin coated on ITO and on Ni (8.5 nm). The emission spectra are very similar and show three sharp peaks at 440 nm, 470 nm and 490 nm. Those values correspond to the singlet intrachain excitons where the most intensive first peak at 440 nm refers to the electronic $\pi^* - \pi$ transition [84].

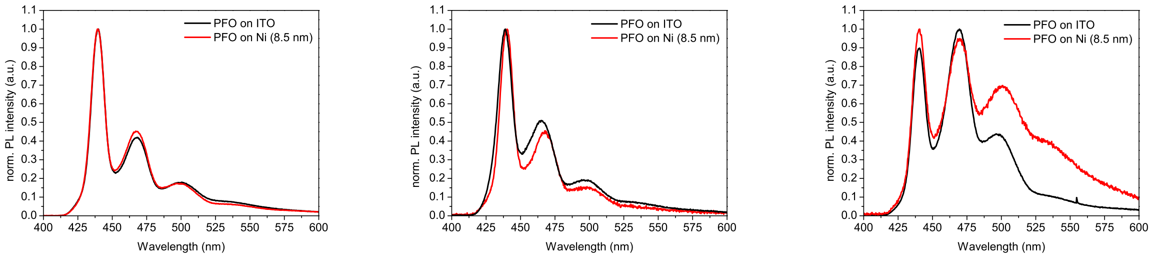

(a) PL spectrum from the Top (b) PL spectrum from the Bottom (c) PL spectrum below Al-cathode

Figure 3.7: PL spectrum for Ni/ITO OLED has been taken from the top (a), from the bottom (b) and from the bottom just below the cathode of the OLED (c)

However, the emission wavelength is not only regarded to the emission of the polymer, but also to the optical characteristic of the stack. Therefore, the outcoupled spectrum might differ from the pure emission spectrum of the polymer which has been also described in equation 2.13 in the theoretical chapter. Almost no difference can be observed when measuring the PL spectrum from the top (figure 3.7a), since the effect of the reflection coming from Ni and ITO on the emission spectrum of the polymer is very low. The PL spectrum has been taken from the top, which means the measured light does not have to travel through a stack of layers with different optical properties for each layer as it was observed for the measurement configuration in figure 3.7b. The refractive index as well as the absorption coefficient varies in dependence to the wavelength. For the PL spectrum (and later for the EL spectrum) all these parameters have to be considered when evaluating the Ni-anode as possible replacement for ITO. The recorded PL spectrum looks different, which might be due to the influence of the optical stack on the emission of the polymer. The emitted light has to travel from the PFO through the PEDOT:PSS (25 nm), the anode material (either ITO (100 nm) or Ni (8.5 nm)) and through the glass substrate (1.1 mm). The low outcoupling efficiency of OLEDs has been explained in the theoretical chapter with the result that most of the light will be trapped inside the OLED stack and guided either to the edges of the OLED or absorbed within the stack. The different modes are wavelength dependent and they are related to the reflectance, absorbance and transmittance characteristic over the wavelength for each material used in this OLED stack [85]. An even stronger difference of the emission spectrum for the ITO and Ni has been observed in figure 3.7c. The emitted light will be nearly 100 % reflected by the Al-back electrode and will travel again through the stack overlapping the pure emission spectrum coming from the polymer. Such a behavior is closely related to the guidance of the light when the OLED is electrically excited. It is therefore expected that the out-coupled electroluminescence spectrum will differ from the photoluminescence spectrum, especially for the vibronic replica.

The current density, luminance and the power efficiency as a function of voltage have been measured for the uncapsulated OLEDs (figure 3.8a-c). The injection of electrons is unlikely to be efficient given the estimated energy gap of 1.6 eV between the work-function of the Al and the LUMO level of the polymer. Apart from the thickest Ni layer device (9.5 nm), in general, the Ni-based devices show lower current densities and higher voltage thresholds than the ITO-based device (figure 3.8a). In general, the Ni layers show a higher sheet resistance than ITO resulting in higher required threshold voltages. It has been reported that the current density in the ohmic regime at low voltages is determined by the anode contact properties rather than by organic bulk properties [86]. The surface roughness influences also the current density by changing the total effective area of contact [87]. Y. - R. Jeng *et. al.* [87] has shown that this additional effect plays a more significant role at initial and low voltages. The higher sheet resistance for low Ni thicknesses limits therefore the device performance in terms of threshold voltage and the voltage at maximum brightness.

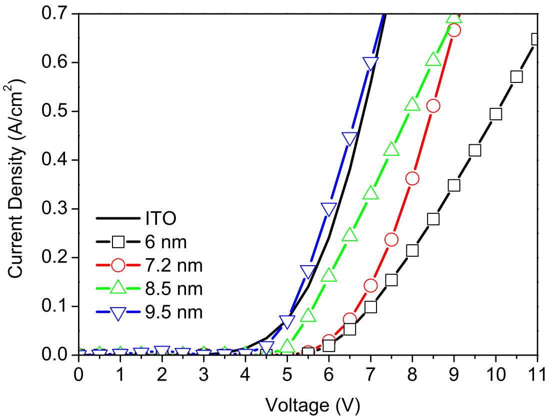

(a) Current density versus voltage of the Ni diodes

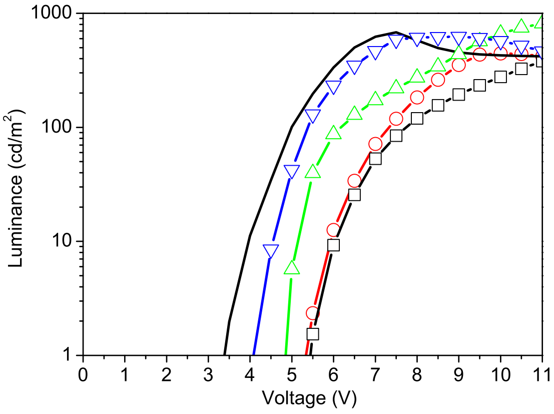

(b) Luminance versus voltage of the Ni diodes

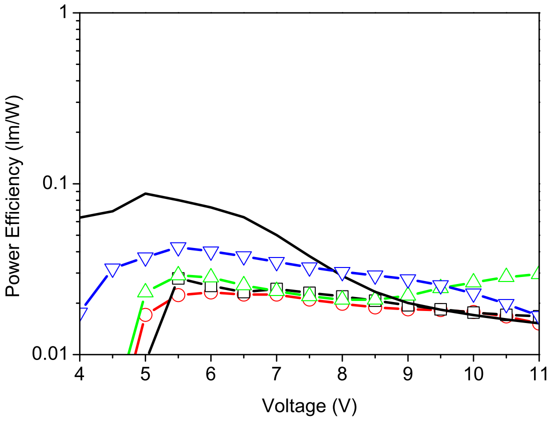

(c) Efficiency versus voltage of the Ni diodes

Figure 3.8: Current density (a), luminance (b) and efficiency (c) versus voltage of the PFO-based diode with ITO (-) and Ni as the anode material, for various Ni thicknesses below 9.5 nm.

The maximum brightness of the ITO device, about 680 cd/m^2, is reached at 7.5 V, while the maximum brightness for the Ni-based devices is reached at higher voltages between 8.5 and 12 V (figure 3.8b). Higher driving voltages are required in device structure where the charge injection or the charge transport is hindered. An energy level mismatch of the polymer and workfunction of the anode/cathode usually leads to a hindered charge carrier injection while the material properties themselves influence the charge carrier transport. The workfunction of the Ni-electrodes and the ITO is very similar. Actually, the device with Ni 9.5 nm as anode even shows an almost similar voltage threshold as the ITO-based device while showing the highest RMS roughness value. These results indicate an interplay between effects related to the roughness and those associated with the sheet resistance of the Ni anode, which increases for lower thicknesses. Indeed, the power efficiency (lm/W) is still lower for the Ni-OLEDs due to the high current density and higher required voltage at the maximum brightness (figure 3.8c). However, Ni shows potential as anode material due to similar measured luminance levels. The optical and electrical properties are very promising and applying Ni as anode does not require any complicated deposition or further treatments in order to achieve reasonable efficiencies.

All the parameters of the OLEDs are summarized in table 3.3:

Material	ITO	Ni 6 nm	Ni 7.2 nm	Ni 8.5 nm	Ni 9.5 nm
Current Density$_{max.L}$ (A/cm^2)	0.78	0.21	0.36	0.51	0.79
V$_{TH}$ / V$_{max.L}$ (V)	3.5/7.5	5.5/12	5.5/10	4.5/11	4/8.5
Luminance (cd/m^2)	680	471	444	815	623
max. Efficiency (lm/W)	0.09	0.03	0.02	0.03	0.04

Table 3.3: Performance data of OLEDs with ITO and Ni as bottom anode.

The electroluminescence (EL) spectrum obtained for each device is very similar, showing a three peak structure centered at 440 ($\pi^* - \pi$ transition), 470 and 500 nm with a small bump at around 550 nm, which is typical for the EL spectrum of PFO-based devices (figure 3.9a). Passive optics simulations have been carried out in order to understand the influence of the ultrathin Ni-metal layer on the outcoupling efficiency. The simulation is purely based on the optical interaction within the device stack. As a difference, the intensity of the first spectral peak is significantly higher when simulating the EL spectrum and comparing with the measured results. In order to obtain better agreement with the experimental data, it would be necessary to fully take into account the charge injection, charge transport, and exciton diffusion in modeling the emitted spectra. Additionally it would be necessary to integrate experimental factors such as defects, pinholes and emissive layer degradation and moreover the exact positions of the emissive dipole due to the charge carrier transport properties within the OLED stack. The thermal deposition of the metal cathode onto the PFO under high vacuum might have influenced the EL spectrum additionally due to the occuring temperature which has been already observed for the Pl measurements in figure 3.7c [84].

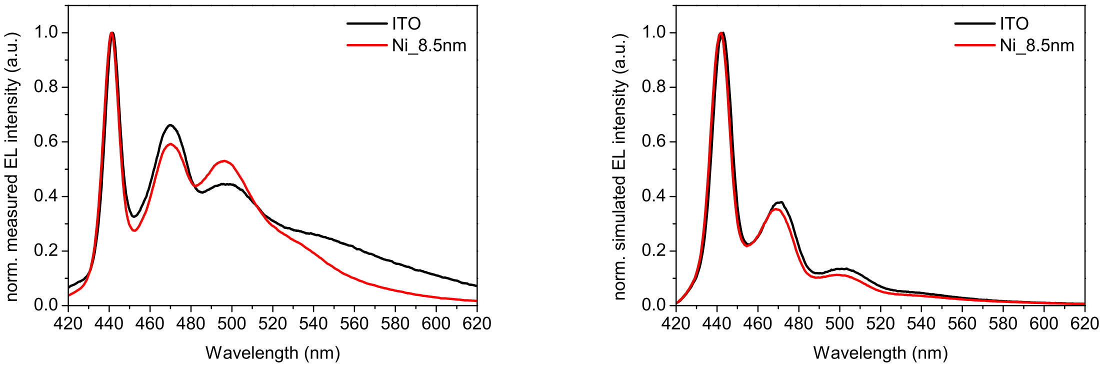

(a)

(b)

Figure 3.9: measured EL spectrum (a) and simulated EL spectrum (b) for PFO-based OLEDs on ITO and Ni (8.5 nm)

The increase of the brightness can be explained looking at the optical properties of the OLED structure. The typical OLED consists of a multilayer sandwich of a planar glass substrate (t_{Sub} = 1 mm, n_{Sub} = 1.51), a layer of ITO (t_{Sub} = 100 nm, n_{ITO} = 1.8), one or more organic layers (t_{Org} = 20 - 100 nm, n_{Org} = 1.6 - 1.8) and a reflecting cathode (Al, Ag or Au), where t refers to the layer thickness and n to the real part of the complex refractive index. In the case of using Ni as anode, the parameters would be $t_{Ni} < 10$ nm. The complex refractive index for each material in this OLED configuration has been calculated from the transmission and reflection measurements (A.1 = PEDOT:PSS, A.2 = PFO, A.11 = Ni). The outcoupled power (figure 3.10a) and the guided mode (relative dipole emitted power guided in the organic layer) (figure 3.10b) have been calculated for the device structure using commercial software based on the Transfer-Matrix algorithm.

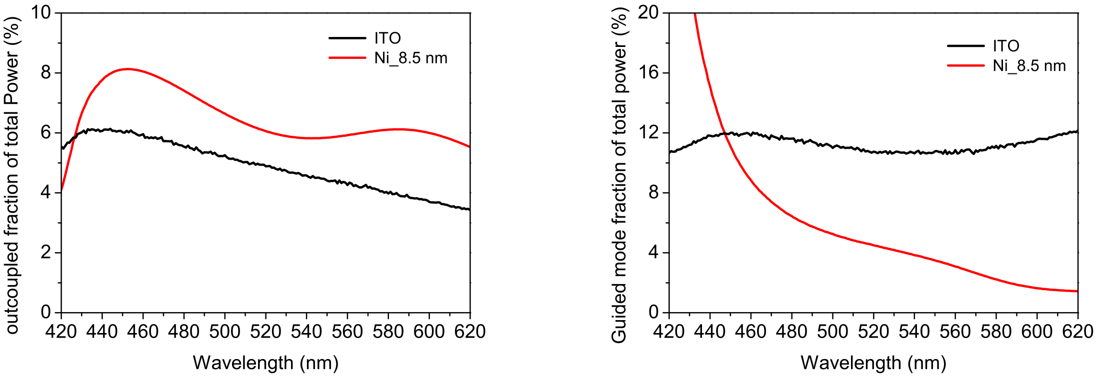

(a) (b)

Figure 3.10: out-coupled (a) and guided mode (b) fraction of the total emitted power for ITO and Ni OLED

The average outcoupling and guided mode fraction of the total emitted power by the dipole have been calculated using the photoluminescence spectrum of the PFO between 420 and 620 nm. The calculated outcoupled fraction of the total power for the ITO-OLED for the given wavelength range is around 5.6 % which is significantly lower than for the Ni-OLED (Ni thickness 8.5 nm) with 7.3 %. Figure 3.10a does not explain the reason for the lower outcoupling efficiency of the ITO-OLED, but shows the variation of the outcoupling power over the wavelength as a result of the wavelength dependence of the refractive index. Figure 3.10b demonstrates the possible reason for the increase of the outcoupling efficiency of the Ni layer even though the transmittance is much lower. It shows a significant drop of the guided mode intensity defined as the relative dipole emitted power guided in the organic layers due to the refractive index difference between the organic layer and the electrode.

Very significant for the lower outcoupled power of the ITO is difference of the dipole emitted power lost in guided modes. The simulated guided modes are relatively constant over the emission wavelength of the polymer even with a slight increase for longer wavelength. The opposite behavior has been observed for this particular device configuration for the Ni device. The power lost into guided modes drops from an initial high value at shorter wavelengths to very low values. The ITO outcoupling efficiency suffers therefore due to the presence of high losses due to the guided modes, in particular at the emission wavelength of the PFO as active material. Again, the outcoupling efficiency has to be calculated and optimized for each specific device structure and each specific emissive polymer since the optical properties of the stack are wavelength dependent. The electrical properties in terms of workfunction and dipole position have been considered to be the same for all the devices.

The outcoupled power as a fraction of the total power emitted by the dipole has been simulated for a Ni layer thickness between 3 and 20 nm (figure 3.11). The device configuration including the simulation parameters (dipole position, quantum efficiency of the polymer) was identical as before. The thicker the Ni electrode, the lower the outcoupled power. The highest outcoupled power has been simulated for the emission wavelength regime of the polymer, between 430 and 490 nm, and a Ni layer thinner than 10 nm, which again confirms the previous results.

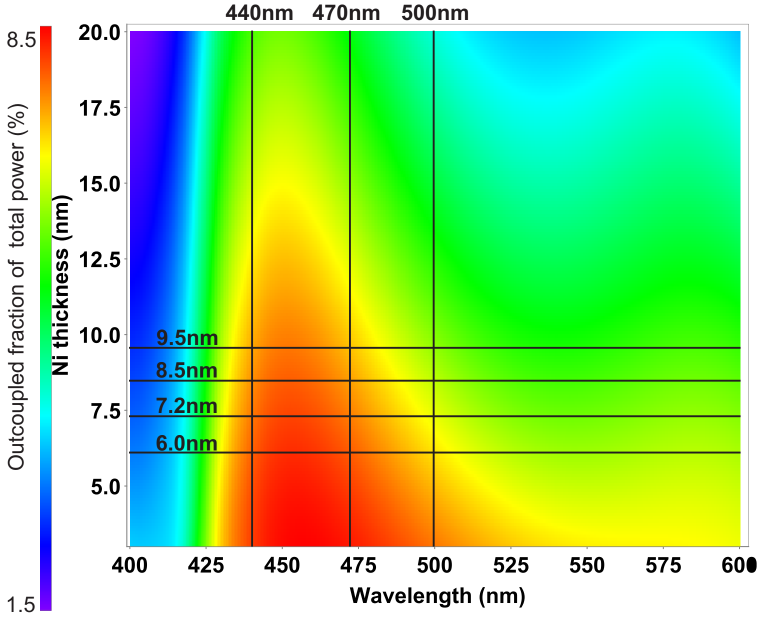

Figure 3.11: outcoupled fraction of the total emitted power in dependence of the Ni thickness for the emission spectrum of PFO, the used Ni thickness and the characteristic maxima at 440 nm, 470 nm and 500 nm for the PFO emission are indicated

To conclude, it has been demonstrated that ultrathin Ni films can be easily fabricated without having any post process and still reach reasonable values in terms of electrical and optical properties. Ultrathin Ni-film have been applied as semitransparent conductive anode contact for bottom light emitting OLEDs. Despite the fact that thin Ni-layers have a lower transmittance, higher roughness and a higher sheet resistance compared to ITO films, the device efficiency was reasonably good when compared to that of the ITO-based device showing the potential of Ni as anode material. The simulation has shown that the outcoupling intensity of the Ni-based OLEDs is higher than for the ITO due to a low guided mode intensity, which explains the *similar luminance level even though the transmittance of the Ni layer is lower. Ultrathin Ni films show therefore a significant potential as low cost and easy processable semitransparent anode material.*

3.3.2 Increased efficiency of Ni-OLEDs due to improved electron injection

The charge injection is very crucial for an efficient functioning of OLEDs with the aim of obtaining a balanced charge injection for both, holes and electrons. Usually calcium (Ca), magnesium (Mg) or barium (Ba) are used as interfacial layer between the polymer and the metal electrode to improve the electron injection [89]. A poor electron injection might have lead in the previous section to an unbalance of electrons and holes resulting in a poor OLED efficiency. Therefore, a 20 nm thin Ca layer was deposited as interfacial layer between the polymer and the cathode metal to improve the overall efficiency. The device architecture (Anode/ PEDOT/ PFO/ Ca/ Ag) and the proposed band diagram are shown in figure 3.11.

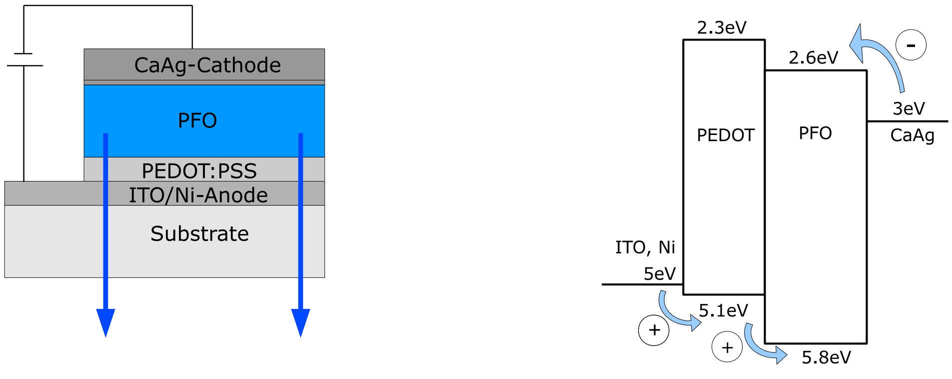

(a) (b)

Figure 3.12: Schematic of PFO-based OLEDs (a) with Ca as interfacial layer and corresponding band diagram (b)

As expected, the overall efficiency is higher for the OLEDs with calcium as interfacial layer due to the improved charge carrier balance since more electrons are injected. The current density is lower and furthermore the threshold voltage has been significantly decreased, as represented in figure 3.12.

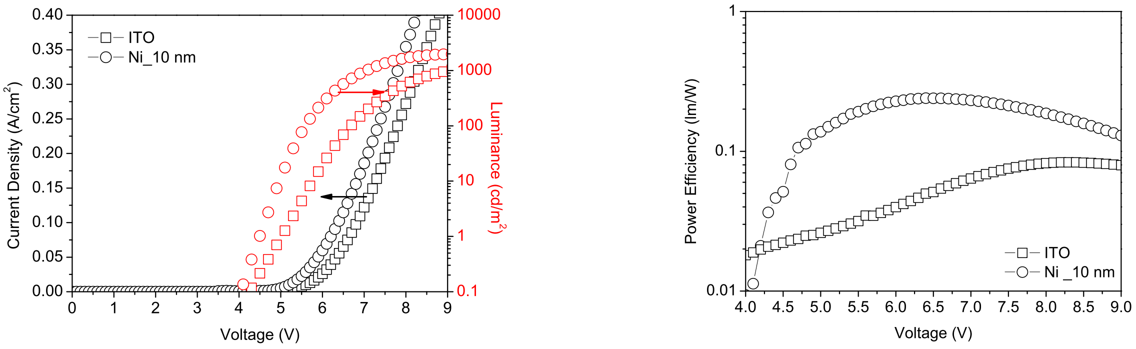

(a) (b)

Figure 3.13: measured OLED characteristics for devices with PFO as active polymer and CaAg cathodes, current density and luminance level (a) and power efficiency (b)

The measured brightness for the Ni-based OLED is indeed up to 45 % higher than for the ITO-OLEDs. Also the threshold voltage (measured at 1 cd/m^2) has been improved and is with 4.5 V slightly lower than for the ITO (5 V). The required voltage at the maximum light emission for the best Ni-OLED is also 0.6 V lower than for the ITO. Those two factors have a significant influence on the power efficiency resulting in a strong increase of the power efficiency for the Ni-OLED, almost 3 times of that one of the ITO. The table 3.4 shows the measured values for all Ni-based OLEDs; the applied voltage at the maximum brightness, the threshold voltage for light emission at 1 cd/m^2, the maximum brightness and the calculated power efficiency.

	ITO	Ni 6 nm	Ni 8 nm	Ni 10 nm
max. Luminance$_{max.J}$ (cd/m^2)	1317	1106	1165	1970
Current Density$_{max.L}$ (A/m^2)	0.59	0.41	0.45	0.55
V$_{TH}$ / V$_{max.L}$ (V)	5/9.7	5.1/11.8	5.3/10.3	4.5/9.1
max. Efficiency (lm/W)	0.08	0.15	0.14	0.24

Table 3.4: Performance data of the PFO-OLEDs with ITO and Ni anode and CaAg as cathode. The current density$_{max.L}$ and V$_{max.L}$ has been measured at the maximum luminance before the OLED starts to degrade. The current density and luminance differ at the in the table given maximum efficiency.

As indicated, the supposedly increased injection of electrons might shift the recombination zone away from the cathode towards the center of the polymer [90]. The emitter dipole position within the emissive layer has been calculated taking into accout the device stack parameters and the measured PL/ EL spectrum. The simulation proves that the recombination zone is shifted from the position close to the CaAg - cathode towards the PEDOT:PSS - PFO interface. A dipole position at around 61 nm (close to the Al-cathode) has been calculated for the previous OLED structure without Ca while the dipole position is shifted to be at 19 nm (close to the PEDOT:PSS-PFO interface) for the present configuration. Shifting the emitter dipole away from the metal cathode leads to lower losses due to evanescently coupled modes. The simulation in figure 3.14 shows the calculated fraction of power lost in the device due to evanescently coupled modes, waveguiding modes, absorption losses and non-radiative power losses (measured PL quantum efficiency of 57 %) and the finally outcoupled power as a function of the emissive dipole position. The highest outcoupling intensity can be obtained when the emissive dipole is close to the center of the emissive polymer. The electrical parameters, such as V_{TH} and current density, are mostly influenced by the improved injection and improved charge carrier balance. Both effects together increase the power efficiency (lm/W) of the OLED device.

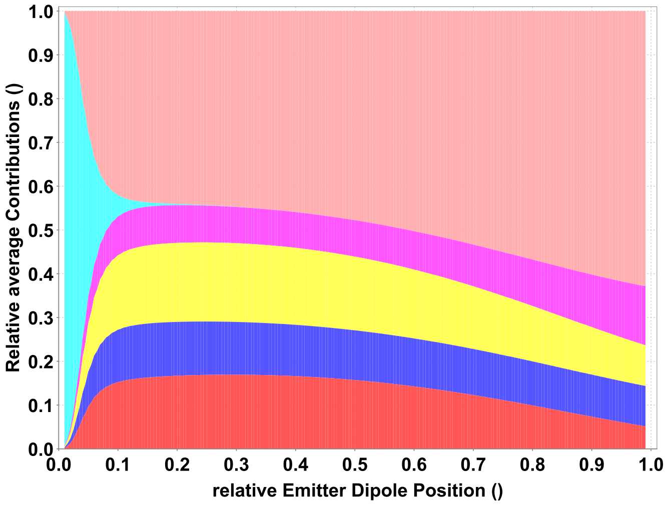

Figure 3.14: relative average power contribution, outcoupled power (red), substrate guided mode (blue), absorption losses in the organic stack (yellow), waveguiding modes (violett) and non-radiative losses (pink) depending on the relative emitter dipole position. An emitter dipole position of "‘0"’ indicates a position at the PEDOT:PSS polymer interface while a relative position of "‘1"’ refers to the Polymer - CaAg cathode interface

The shift of the emissive dipole towards the PEDOT:PSS-PFO interface influences additionally the outcoupled emission spectrum. A significant change can be seen for the electroluminescence of these OLEDs compared to the previous study shown in the recorded electroluminescence spectra. The comparison can be seen in figure 3.15.

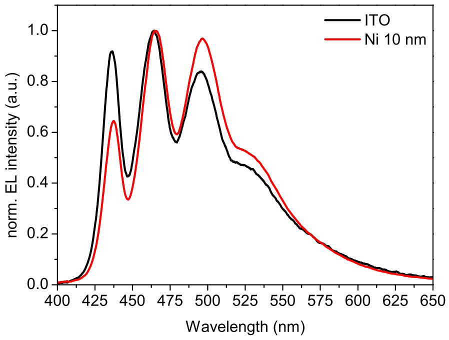

Figure 3.15: comparison of the normalized electroluminescence spectrum for Ni and ITO-OLEDs

The three characteristic peaks for the EL emission have the same intensity which has not been observed in the previous study. In the previous study the first peak was measured to be the most intense followed by the second and the third peaks. The same behavior has been observed for the Ni and the ITO-based OLED. A shift of the recombination zone is often related to a spectrum shift or even a change of the spectrum shape. Simulations have been used for a better understanding of the optical characteristics of such a device structure (figure 3.16). The previously measured optical parameters have been included into the software simulation tool so that the optical effects and their influences on the emission spectrum of the OLED can be evaluated [91]. The emission color and in particular the CIE(Y) component is related to the emitter dipole position. The more green-shifted emission of the Ni OLED might contribute additionally to an efficiency enhancement due to the wavelength dependent sensitivity of the human eye and the derive photometric quantities.

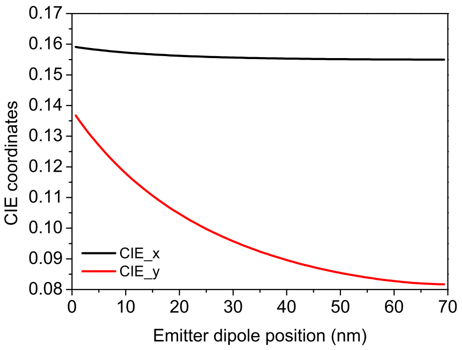

Figure 3.16: CIE coordinates as a function of the emitter dipole position

It would require more work to optimize the device structure in terms of layer thickness, process conditions (solvents, annealing) and/or material parameters. An important result was to show the potential of Ni as semitransparent conductive anode material as replacement for the ITO and it was not the intention to achieve the highest possible efficiencies. However, in order to show the potential of Ni, Ni has been additionally tested in a different OLED configuration using SY polymer. This polymer is known to be stable with high efficiencies in OLED configuration and it was expected to achieve higher OLED efficiencies for both the ITO and the Ni-OLED. The proposed OLED structure and proposed band diagram are shown in figure 3.17:

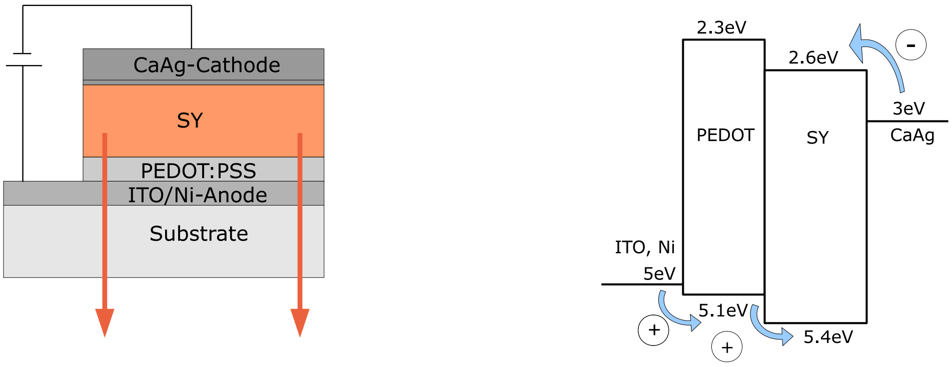

(a) (b)

Figure 3.17: Schematic of SY-based OLEDs with Ca as interfacial layer (a) and corresponding band diagram (b)

The luminance is significantly higher for both devices using SY as emissive layer (figure 3.18a). A significant increase of the OLED efficiency has been calculated from the measurements with a maximum efficiency of 2.1 lm/W at 4 V and 840 cd/m^2 for the ITO-OLEDs and 1.1 lm/W at 3.9 V and 143 cd/m^2 for the Ni OLED. The lower efficiency for the Ni is related to the lower outcoupling efficiency of the Ni-OLED compared to the ITO resulting in higher required driving voltage as shown in figure 3.18a. The lower outcoupled power can be attributed to the difference in the refractive index of the SY and PFO polymers which influences significantly the optical interaction within the OLED stack. An outcoupled fraction of the total emitted power of 8.3 % was calculated for the PFO-based Ni device while the outcoupling power of an OLED based on SY would be around 2 % considering the identical device structure and shift of the emissive dipole position.

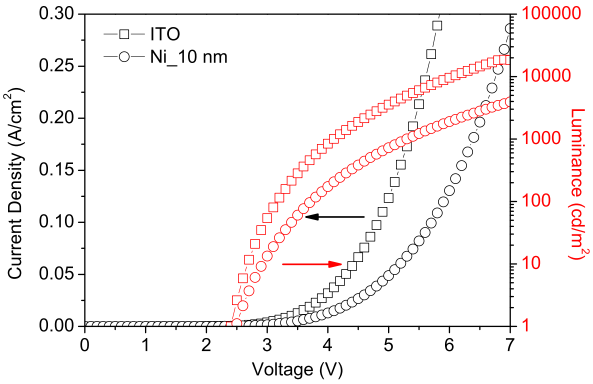

(a) Current density and luminance versus applied voltage

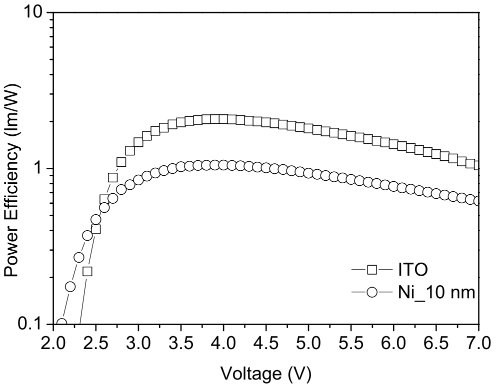

(b) Power efficiency versus applied voltage

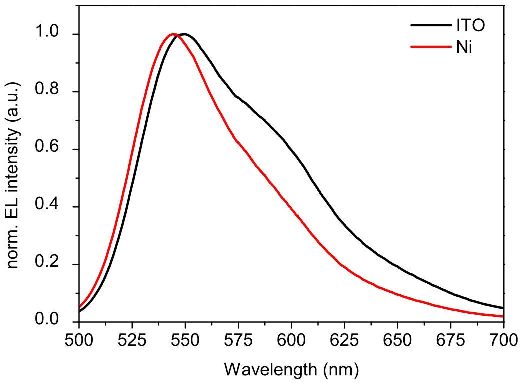

(c) Electroluminescence spectrum for ITO and Ni OLEDs

Figure 3.18: measured OLED characteristics for devices with SY as active polymer and CaAg cathodes, (a) current density and luminance level, (b) power efficiency and (c) electroluminscence spectrum

The presented device structure will be investigated in detail in section 3.4.2., during the analysis of different metal anodes. The threshold voltage (at 1 cd/m^2) is very similar for both devices. G. G. Malliaras *et.al.* [92] described theoretically that the layer properties (sheet resistance and roughness) have a stronger influence when having a lower HOMO level and workfunction difference while, for a high difference, the contact will be injection limited and the layer properties will play a secondary role. Furthermore, the position of the recombination zone is not optimized yet and leads additionally to an unbalance of electron and holes. To optimize the OLEDs, the thickness has to be aligned for achieving the best possible outcoupling intensity and to shift the recombination zone towards the center of the emissive layer. The measured EL spectrum looks different when comparing the Ni and the ITO OLED (figure 3.18c). This phenomenon is probably related to the difference in the optical constants as well as in the thickness difference of Ni and ITO.

To conclude, the potential of Ni as ITO replacement has been further corroborated. Adding an electron injection layer obviously increases the presence of electrons, leading to a higher recombination rate. Additionally, the evaluation of the EL spectrum has shown that the recombination zone for the PFO-based OLEDs is shifted away from the electrodes. Using the well-known SY as emissive polymer leads to more efficient OLEDs and shows that the Ni-anode can be applied in different OLED configurations. The easy processable Ni shows a true potential in both cases and further optimizations in terms of layer thickness or different hole/electron injection materials should result in even higher efficiencies.

3.3.3 Influence of the oxidation of the UTMF on device performance

The activation of ITO, which is basically understood as surface oxidation, is widely used in the fabrication process of OLEDs in order to improve the hole injection from the ITO into the organic layer [93] due to the increase of the workfunction of the ITO. A significant increase of the efficiency of OLED devices has been observed and such a treatment is widely accepted as pretreatment process for OLEDs and OPV devices. The activation of the ITO layer is usually done by plasma treatments or UV ozone processes. Furthermore, UV ozone has additionally become a simple, inexpensive and fast method of obtaining ultra-clean surfaces for the manufacturing of OLEDs. It has been also shown that the contact angle has been modified using these methods so that the polymer materials will form a uniform layer on top [94].

Many metals are known to be easily corroded. It is therefore likely that the surface treatment or even the exposure of metals to air might influence the properties of the metal film especially when using thicknesses of 10 nm or even less. The effect of the oxidization of Ni when stored under ambient condition and when treated with UV-ozone has been studied in this section. Ni-films on a glass substrate were left for two months under ambient conditions (naturally oxidized) and a second Ni-film sample was treated under UV-ozone. OLEDs have been fabricated using the following structure: Ni/PEDOT/SY/CaAg and the OLEDs with the treated Ni-layers have been compared with a pristine Ni-based OLED.

In figure 3.19, the effect of the oxidation on the Ni samples by using the contact angle measurements can be clearly seen. The newly prepared Ni-film shows a contact angle of around 63 ° while the contact angle was significantly increased to 81.5 ° after the natural oxidization. The opposite takes place for the Ni-layer treated for 10 minutes by UV-ozone. The surface becomes more hydrophilic and the contact angle is lowered to 54 °. Usually a low contact angle is preferred when spin-coating polymer on top for obtaining a smooth and uniform film [95].

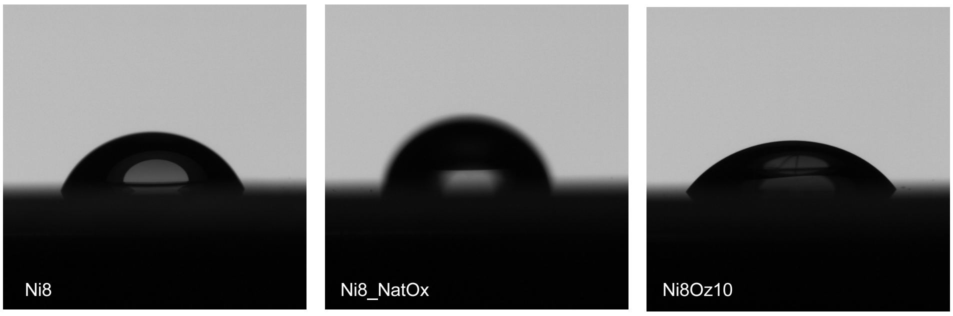

Figure 3.19: Contact angle of a thin Ni-film after natural oxidization

The pure Ni-film shows a sheet resistance of 29.7 Ω/sq and is slightly lowered to 27.6 Ω/sq by leaving the Ni-film for 2 months under ambient conditions. Again, the Ni-film exposed to ozone behaves differently and the sheet resistance is increased to around 32.4 Ω/sq which is an increase of more than 9 %. The effect of the ozone treatment on the transmittance is more or less negligible. An average Vis transmittance of around 36.5 % was measured before the treatment and was slightly increased to 36.8 % after the treatment (figure 3.20). A slight enhancement of the transmittance has been observed for the UV-ozone treated Ni-film for wavelength longer than 500 nm. ITO compared to Ni shows a constant sheet-resistance when treated with UV-ozone with around 16.7 Ω/sq. A similar behavior arose for the ITO transmittance; almost no change for the transmittance was evaluated (86.3 % before the treatment and 86.2 % after the treatment). The UV-ozone process shows a small effect in terms of transmittance for longer wavelengths on UTMF, but the effect on ITO is negligible.

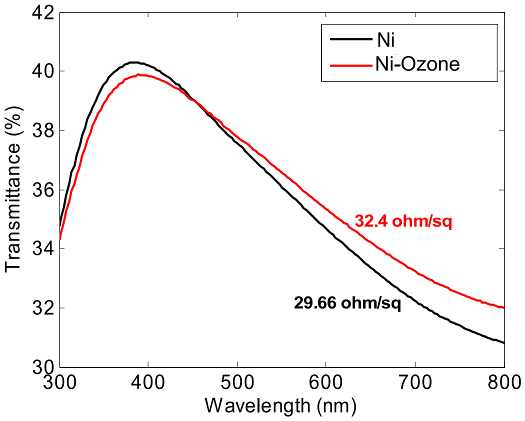

Figure 3.20: Transmittance and Rs before and after ozone treatment

The different pre-treated Ni-films have been then applied as semitransparent conductive anode material for OLEDs. The identical OLED configuration has been used as in the previous section with SY as emissive polymer and a CaAg cathode for an efficient electron injection. The OLED configuration and the proposed band diagram are shown in figure 3.21a and b.

(a) (b)

Figure 3.21: OLED configuration (a) and proposed band diagram (b)

The Ni films show very similar behavior and the results for the OLED measurements are presented in figure 3.22. An increase of the OLED efficiency has been observed for the Ni film which was treated under the UV-ozone. Lower current densities and higher luminance have been measured for the UV-ozone treated OLED resulting in an increase of the power efficiency. The maximum power efficiency has been increased from 1.2 lm/W for the untreated OLED up to 1.4 lm/W for the UV-ozone treated Ni-OLED.

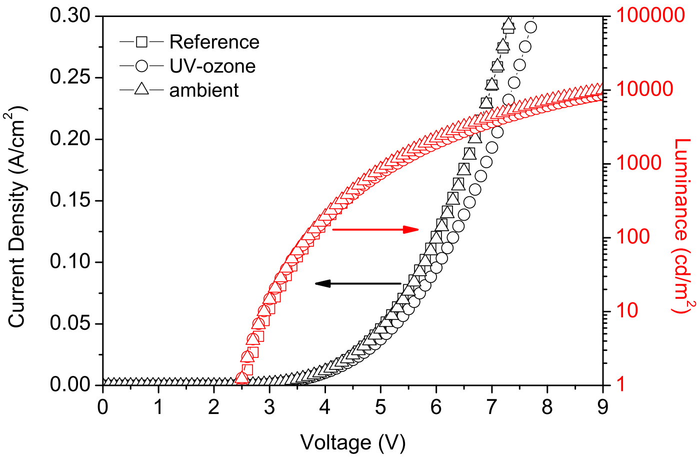

(a) I/V and L/V curve for Ni and treated Ni samples

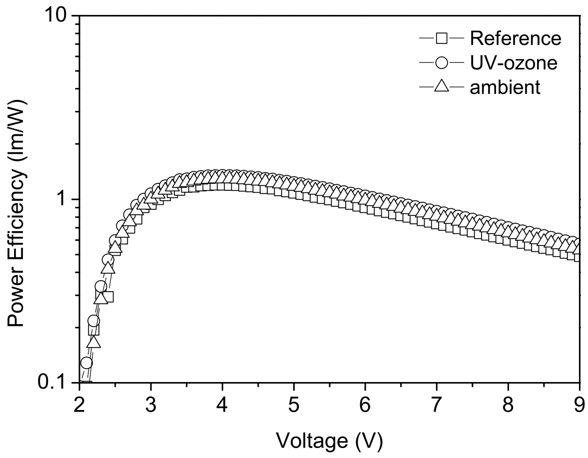

(b) Efficiency for Ni and treated Ni samples

Figure 3.22: measured OLED characteristics for devices with SY as active polymer and CaAg cathodes, I/V, L/V and measured efficiency for Ni and oxidized Ni samples

Such an increase of the current density has been explained by Kim *et. al.* [96] where a workfunction enhancement for ITO has been measured due to the reduction of carbon atoms and the formation of an oxygen-rich surface by the treatment. Furthermore, the UV-ozone treatment removes all organic residues which potentially decrease the contact resistance between the Ni and the PEDOT film leading to an increase of the brightness and therefore in efficiency. No change of the workfunction has been observed after the treatments.

A small increase of the current density has been observed for the Ni-film stored for two months under ambient conditions (natural oxidization). An oxidization of the Ni takes place leading to a similar effect as for the UV-ozone treated Ni-OLED [97]. However, it is well-known that Ni has a very slow oxidization rate at room temperature. The characteristics of the OLEDs are summarized in table 3.5:

	Ni	Ni UV-ozone	Ni ambient
max. Luminance$_{max.J}$ (cd/m^2)	10298	11468	11356
Current Density$_{max.L}$ (A/m^2)	0.8	0.79	0.8
V_{TH} / $V_{max.L}$ (V)	2.5/9.8	2.5/10.1	2.5/9.5
max. Efficiency (lm/W)	1.2	1.4	1.3

Table 3.5: Performance data of the PFO-OLEDs with ITO and Ni anode and CaAg as cathode

To conclude, the contact angle has been significantly decreased when treating the Ni-film with UV-ozone, which is an advantage when depositing uniform polymer films. The electrical and optical properties in terms of sheet resistance and transmittance of the Ni-film did not change very much when treated under UV-ozone. Applying the UV-ozone as a pretreatment process for OLED application leads to an efficiency enhancement of the OLED due to an improved charge carrier injection [96] compared to the untreated OLED. The thin Ni-metal film is therefore a good candidate as an alternative semitransparent conductive anode material due to its low oxidization rate and its potential improvement when treated by UV-ozone.

3.4 Further improvements of UTMF layer using double metal layer

In the previous section, Ni thin metal films were proposed as alternative anodes in OLEDs due to several key advantages over ITO [98][99]. However, other metals have better electrical and optical properties [99] than Ni. Another very good alternative for such applications is Cu, a very inexpensive material with excellent electrical and optical properties already widely used in microelectronics. Ultrathin Cu films are strongly subjected to oxidation and corrosion which alter significantly their electrical and optical properties [100]. A newly developed bilayered ultrathin-metal film (UTMF) structure consisting of an ultrathin and continuous Cu film covered by a protective Ni film has been applied as semitransparent front electrode for organic solar cell (OPV) applications [101]. It was found out the stability of the Cu-film was significantly increased by capping with Ni and such a CuNi-based OPV shows comparable efficiency to the ITO-based device. In the following section, a newly developed bilayered ultrathin-metal-film (UTMF) structure is presented consisting of an ultra-thin and continuous Cu film covered by a protective ultra-thin Ni film as bottom electrode in OLEDs. The multilayer has been applied as semitransparent conductive anode material in an OLED device.

3.4.1 Properties of Ni, Cu and CuNi as UTMF

The following UTMF layers were deposited by magnetron sputtering on double-side optically polished UV grade silica substrates. Cu, Ni, and Cu with a constant 1 nm Ni capping layer, of total thickness of 8 nm each, have been fabricated and the layer properties have been investigated in detail. Figure 3.23a shows the optical transmittance spectrum of as-grown Cu (8 nm), Ni (8 nm), bilayer CuNi (Cu = 7 nm, Ni = 1 nm) and ITO (100 nm) commercial film which has been always used as a reference.

The ITO shows the highest transmittance value at 86 %, while the Cu layer shows 65 % and the Ni layer shows 36 % (values given in table 3.6). The capping of Cu by 1 nm Ni slightly lowered the transmittance of the bi-layer, but it is still higher than for Ni. The reflectance of the transparent anode is very crucial for the efficiency of the OLEDs, the light will be either trapped inside the dielectric stack or outcoupled in an efficient way which obviously increases the overall OLED efficiency [103]. In figure 3.23b, the reflectance of the deposited layers is shown and it is visible that the highest reflectance was measured for the Ni layer due to its poor transmittance. The double layer shows lower reflectance than for the Ni but still higher than for ITO.

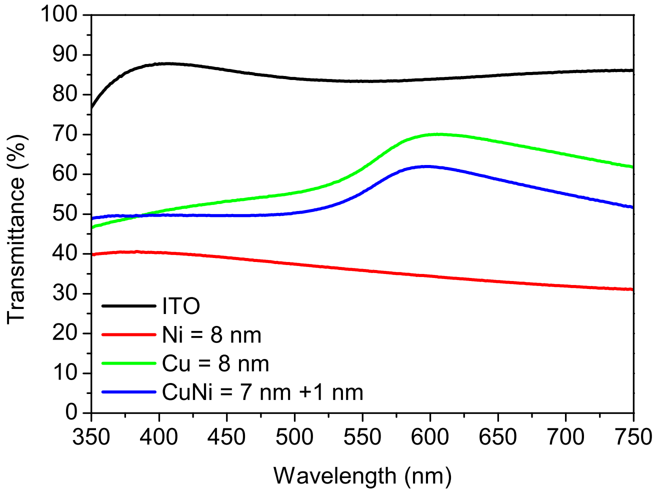

(a)

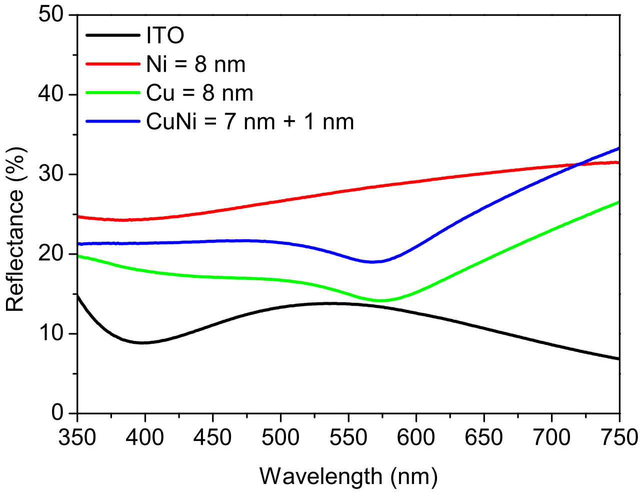

(b)

Figure 3.23: Transmittance (a) and reflectance (b) over the full visible wavelength range

For the sheet resistance, both ITO and Cu layers show a low value around 15 to 17 Ω/sq while Ni is slightly higher, around 30 Ω/sq. It is also observed that the conductivity behavior of the bilayer UTMF is mainly dominated by the underlying ultra-thin Cu layer [102]. Surface treatment is a crucial process for the activation of the anode layer, however, an important side effect is the change of the contact angle [104] for a better spreading of the polymer on the anode surface. A lower contact angle leads to an uniform layer with an improved anode-polymer contact due to the change of the surface energy [105], which can be easily proved using the simple but effective scotch tape test. Several surface treatments have been described and investigated in literature, but this investigation deals with UV-ozone treatment which seems to be the most efficient one for our device configuration. It is well known that the ozone treatment affects the hydrophobicity of the layer by varying the contact angle, and indeed, all the layers including ITO show a reduction of the contact angle, therefore becoming more hydrophilic, as shown in figure 3.24 as an example for the CuNi bi-layer.

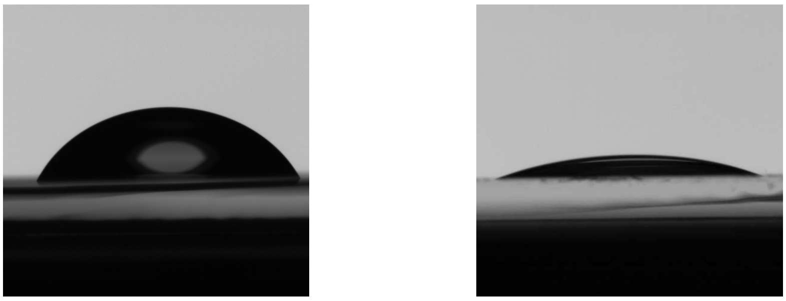
(a) (b)

Figure 3.24: Contact Angle for CuNi before (a) and after (b) Ozone treatment

A treatment with UV-ozone influences as well the optical and electrical properties. A 10 min ozone treatment results in an increase of the sheet resistivity of 9 % for Ni, 65 % for Cu, 8.5 % for Cu-Ni and has almost no influence at all on the ITO layer. Cu layer shows a better transmittance and lower resistivity than Ni. While its transmittance is only 2 % decreased, its sheet resistance is increased by about 65 % after a 10 min treatment in ozone. Capping the Cu layer with Ni offers a better stability of the resistivity with ozone exposure, with only an increase of 8 % this time. The effect of the ozone treatment on the transmittance is more or less negligible for all the layers studied.

Looking at the morphology of the various thin layers, the root-mean-square (rms) roughness measured over an area of 1 μm^2 of all the layers is quite low (less than 0.7 nm), the rougher layer being the Cu layer. Surface roughness has to be kept below the thickness of the layer, otherwise films could be discontinuous and thus non-conductive (figure 3.25). A high roughness might also lead to local short circuits in the device.

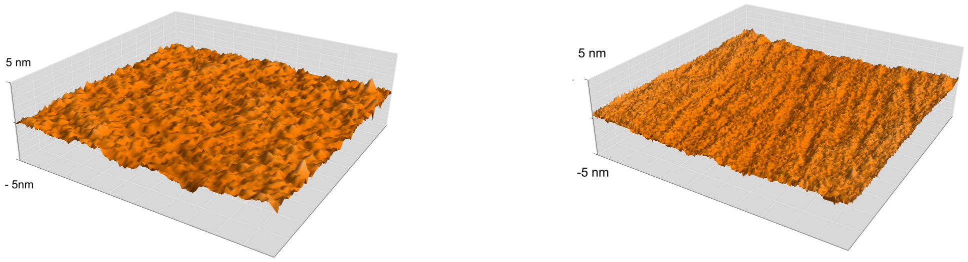

(a) (b)

Figure 3.25: AFM pictures from ITO (a) and CuNi (b)

Pre - or postannealing processes are very important for the fabrication of OLEDs. The materials used in solution processed devices are water-based or contain various solvents. It is well-known that the presence of solvents or water residues (after the fabrication of the OLEDs) is a limiting factor for the device lifetime and efficiency. Therefore, annealing processes are crucial for a functioning device and they might take in a quite broad temperature range with temperatures up to 200 °C or even more. The stability improvement of the Cu layer with a Ni capping is also observed upon thermal treatment of the layers, as shown in figure 3.26.

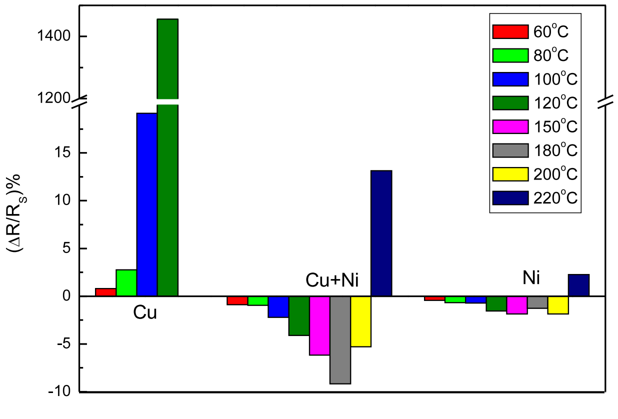

Figure 3.26: Stability of the metallic layers upon thermal treatment (Courtesy of D. S. Ghosh)

The variation of the sheet resistance with thermal treatment reaches high values for temperatures as low as 100 °C for the Cu layer, while for the CuNi bilayer, up to 220 °C the variation in the sheet resistance is small. Cu films are strongly subjected to oxidation and corrosion, which alter significantly their electrical and optical properties. The inevitably partial oxidation of the Cu layer leads consequently to an increase in the sheet resistance. Ni on the other hand is characterized by its very slow oxidization rate and protects therefore efficiently the underlying Cu layer. Aïda Varea *et.al.* (Int. J. Electrochem. Sci., 7, p.1288 (2012)) proved that a Ni-rich electro deposited CuNi film improves the corrosion resistance of the material which is very similar at surface of the CuNi UMTF bilayer. ITO is known to be stable up to very high temperatures. Thus, high temperatures of 300 °C or more improves the optical and electrical properties of the ITO. The Ni and the CuNi bilayer also provide a larger work-function, which is beneficial for the anodic injection. The Haacke figure of merit φ shows a significant improvement for the CuNi bi-layer compared to that of the pure Ni even if it still lower than the ITO. The results are summarized in table 3.6:

	ITO	Ni 8 nm	Cu 8 nm	CuNi 8 nm
mean. Transmittance (%) before Ozone	86	36.5	64.1	56.8
mean. Transmittance (%) after Ozone	86	36.8	61.5	58.6
RsΩ/sq before Ozone	16.7	29.6	15.5	15.3
RsΩ/sq after Ozone	16.8	32.4	25.7	16.6
$\varphi = \frac{T_{Av}^{10}}{R_S}$ (after ozone)	13.2 x 10^{-3}	1.4 x 10^{-6}	0.3 x 10^{-3}	0.29 x 10^{-3}
Contact angle before Ozone	78	63	/	61
Contact angle after Ozone	65	54	/	20
Workfunction (eV) (before Ozone)	5.0	5.1	4.7	5.1
Workfunction (eV) (after Ozone)	5.1	5.2	4.8	5.2
Roughness (nm) (before Ozone)	0.5	0.6	0.7	0.6

Table 3.6: Structural, Optical and Electrical Parameters of the ITO, Ni, Cu and the CuNi layers. The Haacke figure of merit φ was calculated from the average transmittance and the sheet resistance

To summarize, the main drawback of the Cu layer for device application, which is its low stability to oxidation and temperature, has been alleviated by simply using a 1 nm Ni capping layer. Therefore, the Ni capping makes Cu-Ni UTMF very interesting for the OLED applications as it overcomes the stability issue of the Cu layer and increases the work function, still maintaining good optical and electrical properties.

3.4.2 Double metal layer as anode for bottom light emitting diodes

In the previous section, UTMF anodes were analyzed and applied as semitransparent conductive anode for bottom light emitting diodes. The following OLED structure has been used in this investigation with the corresponding layer sequence in figure 3.27.

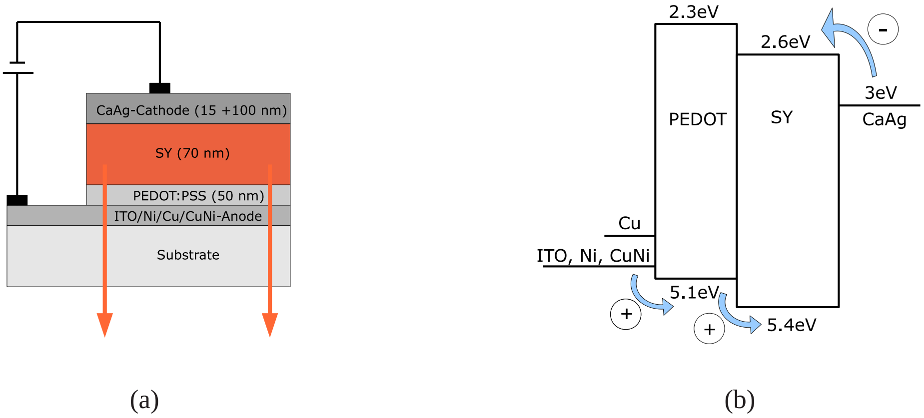

(a) (b)

Figure 3.27: Schematic of SY-based OLEDs (a) and corresponding band diagram (b) varying the anode material

Figures 3.28a and b compare the current-voltage (I/V) and luminance characteristics of OLEDs with a thin metal anode against those of a typical ITO anode. It can be seen that the lowest performance is obtained for the Ni-based device. Slightly higher voltage threshold, lower current density and lower luminance reflect the poor transmittance and high resistivity of the 8 nm Ni layer. The luminance of the Ni-based OLED is significant lower although the workfunction of Ni is similar to the one of ITO and guarantees therefore a similar charge carrier injection. A limiting factor for the charge carrier transport might be the higher sheet resistance of the Ni which would explain higher driving voltages but not the lower luminance level. Also the emissive dipole position is with a simulated value of 56 nm closer to the metallic cathode resulting in a less efficient radiative recombination due to possible losses at the metal cathode. As a result, the current efficiency 1.5 cd/A for the Ni-OLED is poor compared to the reference ITO OLED with 2.9 cd/A. Another limiting factor is the difference of the outcoupling efficiencies of the different device configuration. The optical interaction in the stack is explained more in detail for the presented device structures in the following part of the chapter and shows a very low outcoupling for the Ni-OLED.

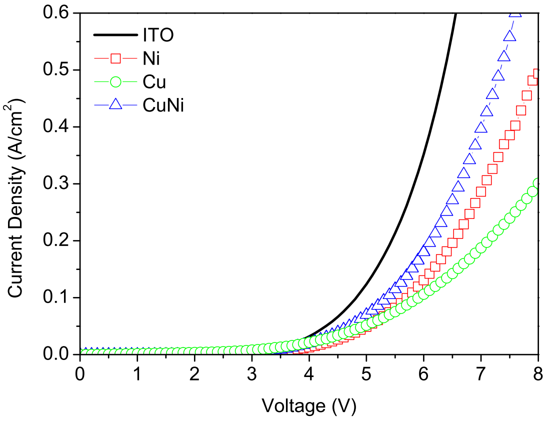

(a) Current density versus applied voltage

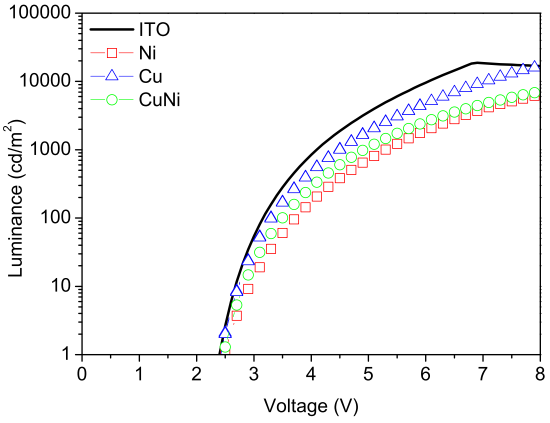

(b) Luminance versus applied voltage

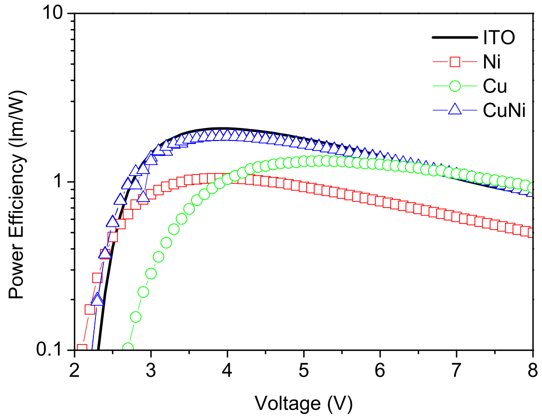

(c) Efficiency versus applied voltage

Figure 3.28: IV, LV and efficiency of SY-based OLEDs with the anode being ITO, Ni, Cu or CuNi

The Cu-based device behaves very similarly to the Ni-based device, as the driving voltage at a given current density is found to be higher than the one of ITO. This difference might be due to the sheet resistance values of Cu and Ni, which, after the ozone treatment, stand around 32 Ω/sq and 27 Ω/sq respectively, compared to 17 Ω/sq for ITO. The advantage of the Cu-based device lies in the higher transmittance of the Cu layer compared to the Ni layer and therefore it shows a higher luminance level than the Ni-based device. The higher luminance is possibly obtained due to a shift of the emitter dipole position, simulated to be at 49 nm. When looking at the device efficiency, the Ni-based and the Cu-based device show a lower efficiency compared to the ITO-based device.

The CuNi double layer anode has a similar sheet resistance (around 17 Ω/sq) to the one of the ITO resulting in a similar threshold voltage and maximum luminance level for the OLED. A further increase of the luminance compared to the Ni and Cu-OLEDs has been obtained due to the lower sheet resistance and the higher transmittance of the CuNi film. The CuNi-OLED shows a threshold voltage for light emission and a maximum luminance level close to the ITO reference device. Additionally the emitter dipole position is with a simulated value of 46 nm well centered leading to an efficient radiative recombination. Furthermore, the current efficiency has been significantly increased compared to the single layer metal films and is with 2.7 cd/A close to the value of the ITO-OLED, which again shows the potential of the double metal layer as anode for bottom light emitting diodes. The results of the OLED measurements including the calculated power efficiency in lm/W are summarized in table 3.7.

	ITO	Ni 8 nm	Cu 8 nm	CuNi 8 nm
V_{TH} / $V_{max.Lce}$ (V)	2.4/6.9	2.5/8.6	2.5/11.3	2.4/8.1
max. Luminance (cd/m^2)	18730	9265	15024	17165
max. Efficiency (lm/W)	2.1	1.1	1.3	1.9

Table 3.7: Threshold voltage V_{TH}, voltage at maximum brightness $V_{max.Lce}$, efficiency at maximum brightness efficiency$_{max.L}$ and maximum efficiency for SY-based OLEDs when using ITO, Ni, Cu or CuNi as anode and CaAg as cathode.

The difference in terms of OLED efficiency is very likely not only caused by the different electrical properties of the anode metals, but also by the difference in the optical properties within the OLED structure. An important aspect of metal based OLEDs is the possible presence of cavity effects, which leads to an angular dependence that is different from that of ITO-based devices. Hence, the fact that luminous efficiency is comparable in the normal direction does not necessarily guarantee that it is also in an off-normal direction. Indeed, microcavity OLED can exhibit significantly enhanced emission in the forward direction as well as a much narrower emission spectrum [106][107], making evident that possible microcavity effects of the proposed metal-based devices have to be considered. To this end, the theoretical description of the microcavity effect in OLEDs, as cited in Ref. [107], explains that a weak microcavity effect occurs associated to the low reflectance of the Cu, Cu-Ni and ITO layers, which is about 15 - 18 % at the wavelength of the emission peak (for Ni, it is about 30 %). The electrically stimulated emission is slightly shifted for the different material with around 542 nm for the Ni-OLED and around 549 nm for the rest. The highest transmittance and therefore lowest reflectance takes place between 500 and 600 nm for the Cu and CuNi resulting in a low microcavity effect. Furthermore, the electroluminescence (EL) spectrum for all devices has been measured and the results are shown in figure 3.29.

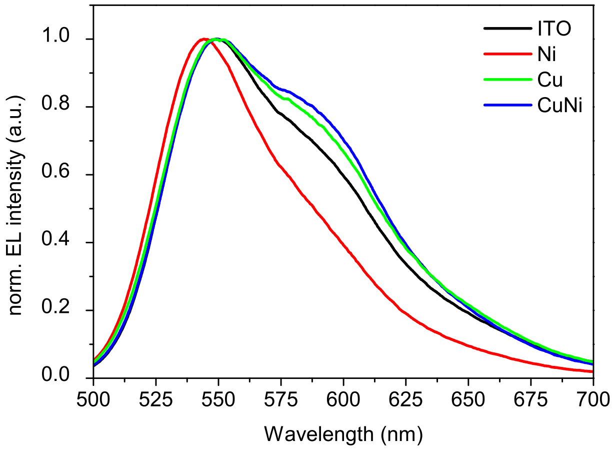

Figure 3.29: Electroluminescence spectrum of SY-based OLEDs with the anode being ITO, Ni, Cu or CuNi

The full width half maximum (FWHM) of the spectrum is similar for the Cu, CuNi and for the ITO-based OLED (around 90 nm). Only the Ni-based device shows a thinner FWHM (around 72 nm), which agrees with the value of its reflectivity – the highest among the three metal electrodes. The calculated full width at half maximum (FWHM) and the wavelength at the maximum EL emission have been summarized for the OLEDs in table 3.8.

	ITO	Ni 8 nm	Cu 8 nm	CuNi 8 nm
FWHM (nm)	87.3	72.1	91.4	92.2
max. EL (nm)	548.8	542.8	549.2	548.2

Table 3.8: FWHM and the wavelength at the maximum EL emission peak for OLEDs with ITO, Ni, Cu or CuNi as anode and CaAg as cathode

The electroluminescence and the outcoupling efficiency have been calculated for OLEDs based on the UTMFs anode and using the measured PL and EL spectrum. The refractive index n and the extinction coefficient k for the different anode materials (ITO, Ni, Cu, CuNi) and from the polymer materials used (PEDOT:PSS, SY) have been measured and the results for each material can be found in the figure section of the appendix. The data have been used in commercially available optical simulation software.

A shoulder in the EL-spectrum appears for all the measured devices (ITO, Cu, CuNi) at around 600 nm. This shoulder is suppressed for the Ni-OLED and is the main reason for the reduction of the FWHM. The difference in the EL-spectrum might result from the different refractive index of the Ni and the CuNi as shown in figure A.11 and A13. The change of the spectrum can be explained in detail when simulating the outcoupled spectrum using the PL spectrum of the SY (figure 3.30). As an example, the Ni and CuNi OLEDs have been compared since their FWHM shows a significant difference of 20 nm. The simulated EL spectrum shows a similar difference at around 600 nm (figure 3.30a). It can be assumed that this effect is only related to the different optical properties of the stack. The shape of the outcoupled power over the wavelength is very similar for the Ni and the CuNi (figure 3.30b). But the outcoupled fraction of the total emitted power is around 1.5 % lower for the Ni device over the calculated wavelength regime. Additionally the curve of the CuNi-bilayer does not follow exactly the Ni curve showing an enhanced outcoupling between 550 nm and 650 nm which finally results in a difference of the EL-shape. This effect is more visible when normalizing the outcoupled power between 550 nm and 650 nm (see inset figure 3.30b). This difference of the outcoupling is attributed to the absorption coefficient, as shown in figure A.11 and A13, which drops significantly for the CuNi-bilayer for wavelengths longer than 550 nm.

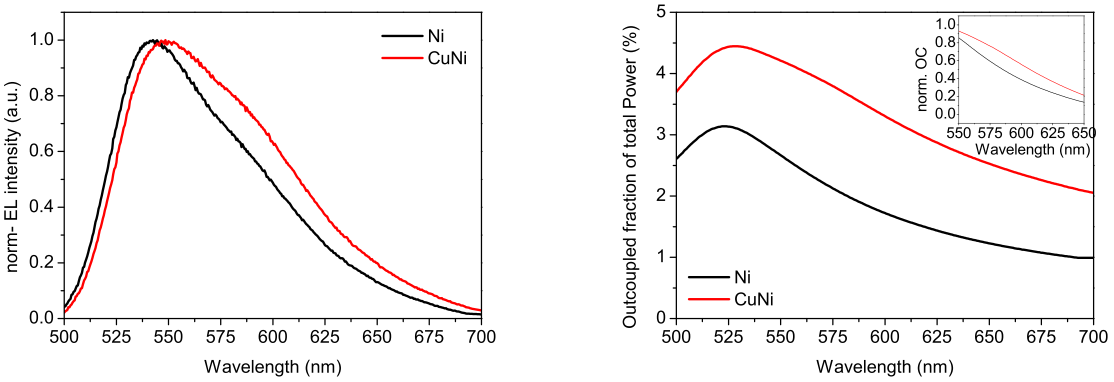

(a) simulated EL-spectrum

(b) calculated out-coupling fraction of total power

Figure 3.30: simulated EL (a), calculated outcoupled fraction of total emitted power (b) for Ni and CuNi OLED

The average outcoupled fraction of the total emitted power by the emitter dipole over the wavelength range between 500 nm and 700 nm has been calculated for all the device structures. The highest outcoupled fraction has been calculated for the ITO-OLED in this particular device configuration, resulting in the highest efficiency among the OLEDs. However, the average outcoupled fraction is not significantly higher for the ITO (4 %) compared to the metal layers, in particular to the CuNi OLED (3.6 %). Cu, for instance, shows good optical properties (outcoupled fraction of 3.8 %) with even a slightly higher outcoupled fraction than CuNi which makes Cu favorable as anode material if it would be thermally stable and not showing such a fast oxidization. Such values are quite typical for OLEDs with such a configuration indicating that almost 80 % of the emitted dipole power is therefore lost for all the presented devices (due to intrinsic non-radiative losses as explained in the theoretical chapter), but this investigation also shows the potential of OLEDs when improving the outcoupling. The results show that the outcoupling intensity as well as the good electrical properties of the CuNi lead to the highest device efficiency among the UTMF-OLED, even though the efficiency of the ITO-OLED has not been completely reached. However, the brightness, threshold voltage, as well as the emission spectrum is very similar which makes CuNi a potential candidate for replacing ITO.

Further improvements in terms of the electron - hole balance would lead to a further shift of the emissive dipole position towards the PEDOT:PSS - polymer interface resulting in a further enhancement of the efficiency for the CuNi OLED. An optimum outcoupling efficiency of around 4.75 (%) can be found for this particular emission spectrum when shifting the emissive dipole at a position of 21 nm from the PEDOT:PSS - polymer interface. The optimized outcoupled power as a function of the emission wavelength of the emitting polymer SY and the emitter dipole position has been simulated in figure 3.31.

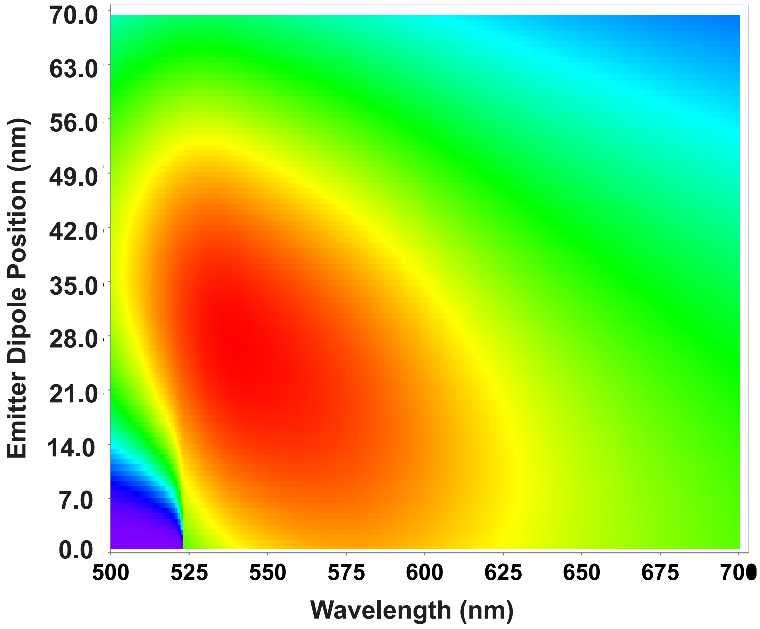

Figure 3.31: Outcoupled fraction of the total emitted power as a function of the emitter dipole position with the distance from the PEDOT:PSS - polymer interface

It is important to point out the role of the capping Ni layer, which has enabled the Cu-Ni layer to retain good electrical and optical properties after the ozone treatment. This is even more visible when studying the luminance as a function of the operating time of the devices (shown in figure 3.32). The graph shows the inital investigation for the lifetime measurement and a deeper analysis is required to understand the metal anode influence on the device stability. The lifetime experiments were performed under inert atmosphere and darkness without encapsulation. The OLEDs have been stressed for 360 min and the luminance has been measured for every 10 min.

For glass/ ITO device, the luminance decay of the devices is slow, losing around 30 % of its initial brightness after 360 min. Although the luminance of the Cu-Ni anode/ glass substrate device dropped initially, its decay is very smooth and reaches 35 % after 360 min, at higher current when compared to the driving current for ITO anode/ glass substrate. Cu anode/glass substrate devices loses about 77 % of the initial luminance after applying a voltage for around 360 min due to the expected reaction of the waterbased and acidic PEDOT:PSS with the Cu. Actually, the ITO and Cu-Ni based devices show a similar slope of the luminance, showing again similar behaviors of the Cu-Ni bilayer and ITO as anodes for OLEDs.

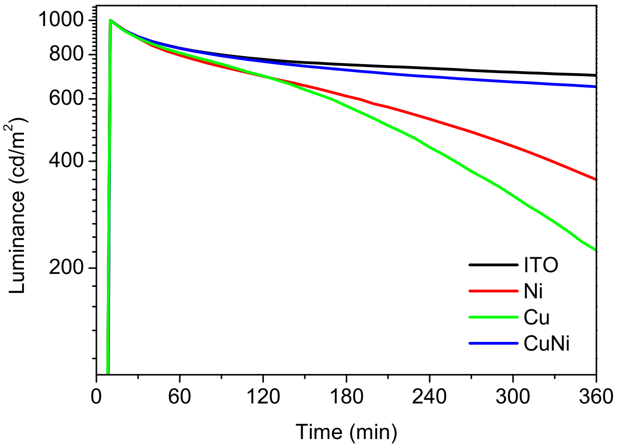

Figure 3.32: Lifetime of SY-based OLEDs with the anode being ITO, Ni, Cu or CuNi

In sum up, the use of Cu–Ni UTMF as anode in high-performance OLEDs has been demonstrated. Previous studies have shown the potential of Ni UTMF to replace ITO for organic device applications, due to easy fabrication, good optical and electrical qualities [76]. Cu UTMF was also studied due to better optical and electrical properties than Ni, although it shows poor stability when treating the metallic layer with higher temperatures. A good trade-off between the Ni stability and the Cu excellent optical and electrical properties for UTMF is an ultrathin Cu layer stabilized using a capping Ni layer. Its average visible transparency is as high as 64 % and its sheet resistance as low as 15 Ω/sq. The bilayer Cu–Ni UTMFs show excellent stability against temperature and oxidation. It is demonstrated that double layer UTMFs are an effective alternative electrode with easy fabrication and low cost [77].

3.5 Conclusions

Initially, Ni as ultrathin single layer metal film was investigated for its potential as anode electrode for bottom light emitting diodes. Ultrathin metal layers with thicknesses between 6.5 and

9.5 nm have been investigated and compared with ITO. A 9.5 nm thin Ni film shows a reasonable sheet resistance and workfunction which is suitable for OLED applications. However, the transmittance is around 33% and therefore much lower than for ITO with 86%. The transmittance of thinner Ni films would be obviously higher, but the drawback is the significantly increased sheet resistance. Furthermore, the metal film would be discontinuous for thicknesses below the percolation thickness, which is usually between 3 and 6 nm. The Ni film has been applied as semitransparent conductive anode for bottom emitting OLEDs and it has been shown that a similar or even higher luminance can be reached even though the transmittance of the Ni is much lower than for ITO. The improvement is not the result of an improved electrical contact and charge carrier injection, since the power efficiency of the Ni OLEDs is lower due to its higher driving voltages. The high driving voltage is the result of the missing electron injection layer leading to an unbalance in electrons and holes. An explanation for the increased luminance intensity has been found looking at the different optical modes in the device structure. The luminance enhancement is the contribution of an increased outcoupling for the investigated device specification and the characteristic emission for the used blue-emitting polymer. A simulation based on the matrix-transfer formalism confirmed this assumption of an increased outcoupling efficiency. Ni shows therefore its potential as anode electrode with several advantages including simple deposition, no need for post deposition treatments, and lower cost.

However, the efficiency of the presented OLEDs was still quite poor due to the inefficient electron injection, which results from the use of only Al on the cathode side. Increasing the overall efficiency using an electron injection layer (Ca) and PFO and SY as emissive polymer was the issue in section 3.2.3. The significant enhancement of the luminance as well as the efficiency is clearly the result of the increased electron injection leading to a more balanced ratio between electrons and holes. A difference in the electrons - holes ratio influences obviously the position of the recombination zone. The position of the recombination zone can be simulated and was shifted from before x = 0.85 (relative distance from the PEDOT - Polymer interface) to 0.26 for the OLEDs with electron injector and PFO as emissive polymer. The measured efficiencies for the OLEDs with PFO and Ni were even higher than for the ITO reference OLED with almost a three-time higher efficiency for the best Ni OLED with a 10 nm thin layer.

To overcome the issues of Ni-metal films such as low transmittance and relatively high sheet resistance, a double layer based on Cu and Ni has been extensively investigated. Cu shows better optical and electrical properties than Ni, but poor stability upon heating. Cu as single material is well-known for oxidizing very fast with a strong negative impact on the electrical and optical properties. It was found that Cu is very stable when capped with a Ni layer, maintaining the excellent electrical and optical properties of pure Cu and very good stability against temperature and oxidation of pure Ni. The average transparency in the visible part of the spectrum is around 64 %, which is more than a twofold increase compared to pure Ni. When applied to OLEDs, the device with CuNi as anode shows the highest efficiencies among the metal film based OLEDs. The efficiency of the CuNi-based OLED is still lower than for ITO in this device configuration; however, a strong increase has been obtained compared to the Ni OLED. A strong enhancement of the luminance was observed for the double layer with a similar threshold voltage as it was measured for the ITO. The simulation confirms the significantly increased outcoupling efficiency for the CuNi-OLED configuration in comparison with the ITO-OLED. The observed temperature stability, processability at room temperature together with the optical transmittance and electrical resistivity performances confirm that multilayer Ultrathin Metal Films are serious competitors to transparent conductive oxides such as ITO.

Chapter 4

Atomic Layer Deposition (ALD) Technique applied to multilayer organic LEDs

An established method to enhance the efficiency of OLEDs is the use of multilayered device structures, consisting of layers of organic semiconductor materials with different energy levels and functionalities (e.g. charge transport, emission, blocking layers). In small-molecule-based OLEDs, which are commonly fabricated via vacuum deposition techniques, the fabrication of heterostructures is relatively straightforward [108][109]. In contrast, in solution-processed OLEDs, the situation is more complex. When a layer stack is made by solution processing, it is imperative that a layer is not attacked and dissolved by subsequent coating steps [110][111]. In the past few years many strategies were developed to overcome the dissolution problem and to prepare multilayer OLEDs by spin coating [112]-[114]. This can be achieved, for example, by using orthogonal solvents for each layer or by making the deposited film insoluble by, for instance, a subsequent cross-linking step [114]. Since cross-linking steps require high temperatures and may lead to unwanted diffusion of material, a fully solution processed OLED with good performance is very difficult to obtain. Recently, a liquid buffer method which completely prevents the dissolution between solution-processed polymer layers was reported to achieve high-efficiency and stable OLEDs [115].

A possible approach for obtaining multilayer OLEDs is the use of a thin film of a metal-oxide deposited directly on top of the solution processed organic layer. C.-Y. Chang et. al. [116] have shown that OLEDs can withstand an aggressive photolithographic patterning process without *any degradation of the organic layer by using a thin (1 nm) atomic-layer-deposited* Al_2O_3 *film as a protecting layer for the electroluminescent (EL) organic material. A possible routine for the alignment of the charge carrier transport has been shown in [117] where a 1 nm thin natural grown aluminum oxide has been used as buffer layer in organic photovoltaic cells. Such* Al_2O_3 *can be deposited well controlled via atomic layer deposition as referenced before.*

In this chapter, atomic layer deposition (ALD) was used to form Al_2O_3 *films as buffer layers, taking advantage of ALD's low defect density, high conformity, and low deposition temperatures to maximize the surface coverage of such thin films and to avoid thermally degrading the EL layer. Multilayer OLED structures are realized using sequential solution processing and a thin* Al_2O_3 *film as an intermediate protection layer. Even though ALD is originally a vacuum based process, there are recent approaches for ALD at atmospheric pressure and R2R manufacturing. Very recently, BENEQ sold a R2R ALD equipment to the CPI's NETPark facilities in Sedgefield in North East England for the development of flexible thin moisture barriers films.*

4.1 Experimental details

The same ITO substrate, surface treatments and PEDOT:PSS deposition recipe as described in chapter 3 have been used for the OLED fabrication. The samples spin-coated with poly(para-phenylene vinylene) (PPV) copolymer SY were additionally heated for 10 min at 120 °C due to the higher boiling point of Toluene (111 °C) while the samples with 2-methoxy-5-(2-ethylhexyloxy)-p-phenylene vinylene, namely MEH-PPV were heated for 10 min at 70 °C due to the lower boiling point of chloroform (62 °C) and low glass transition temperature of the MEH-PPV. The process recipes are summarized in table 4.1.

Polymer	Concentration (mg/ml)	Solvent	Spincoating Recipe	Thickness (nm)
MEH-PPV	10	$CHCl_3$	1500 RPM for 20s	120
SY	5	Toluene	2500 RPM for 20s	80
Alq_3--1	1	$CHCl_3$	2500 RPM for 20s	5 *
Alq_3--3	3	$CHCl_3$	2500 RPM for 20s	8 *
Alq_3--6	6	$CHCl_3$	2500 RPM for 20s	10 *

Table 4.1: Polymer solution concentration, spin-coating recipe and resulting thickness; (*) indicates that the layers were measured on glass

Alq_3 (Sigma Aldrich) has been dissolved in chloroform $CHCl_3$ in different concentrations and spin coated either directly onto the SY film or onto the SY layer protected by the oxide. Al_2O_3 layers with different thicknesses and deposited at different temperatures have been used in this chapter. The final multilayer device structure is shown in figure 4.1b.

Figure 4.1: reference OLED (left) and investigated multilayer device with a solution processed Alq_3 layer, SY has been protected by a thin aluminum oxide Al_2O_3 layer deposited by ALD (right)

4.2 Effect of the deposition process on the intrinsic properties of organics

High quality Al_2O_3 can be deposited by the ALD technique when the temperature and the cycling time (referring to the chemical reaction) are calibrated well [118][119]. In that term, a densely packed oxide promotes a better protection against environmental impacts (e.g. oxygen, water and solvents) when used as encapsulation. Usually, the ALD process requires temperatures higher than the glass transition temperature (Tg) of the polymer, fulfilling the requirements for processing densely packed oxides. It is therefore important to study the effect of the ALD process on the polymer for two reasons: first, the temperature effect during the deposition process and, second, the effect of a chemical reaction of the polymer with the precursors. The well-known soluble SY with a high Tg of around 180 °C has been used and compared with MEH-PPV with a low glass transition temperature of around 75 °C in the following demonstration (figure 4.2a,b). The ALD layer was deposited with different thicknesses ranging from 0.2 nm up to 5 nm. The process time was varied depending on the process temperature and the wanted thickness (number of cycles).

Samples without an ALD deposited oxide have been chosen as reference.

(a) sample with SY as emissive material

(b) sample with MEH-PPV as emissive material

Figure 4.2: Al_2O_3 deposited on SY (a) and MEH-PPV (b)

It should be mentioned that such ALD process has been shown to have adverse effects on the organic layer. C.-Y. Chang *et. al.* [116] have shown that the Al_2O_3 layer deposition disrupt the conjugation length of the polymer (MEH-PPV in that case). The affected MEH-PPV became insulating due to the disrupted conjugation, and therefore the device characteristics deteriorated drastically. This polymer chain conjugation disruption has been attributed to the exposure to trimethylaluminum (TMA) and the use of elevated temperature in the ALD process, which accelerated the permeation of TMA vapors into the organic layer [120]. They determined that the mechanism of the conjugation disruption happens through electrophilic addition of TMA to the vinylene C=C groups of MEH-PPV. The significant change in the UV-Vis spectrum (spectrum shift and weakening of the signal) caused by the ALD Al_2O_3 layer indicated that the TMA exposure affected not only the top surface but also the bulk of the MEH-PPV layer. In order to reduce the effect of the ALD deposition on the organic layer, the deposition of the Al_2O_3 layer should be performed at low temperatures, even though such a low temperature ALD process takes longer time. The deposition process in this work was very similar to the ALD process described by C.-Y. Chang *et. al.* using a pulse of TMA followed by a pulse of H_2O [119].

To check the possible deterioration of the organic layer by the ALD process, the optical properties of MEH-PPV (low Tg) and SY (high Tg) were studied before and after the Al_2O_3 layer deposition at different temperatures (80 °C, 150 °C and 235 °C). Figure 4.3 demonstrates the importance of a low temperature Al_2O_3 deposition (80 °C) on 2-methoxy-5-(2-ethylhexyloxy)-p-phenylene vinylene (MEH-PPV) with a glass transition temperature as low as $Tg = 75\,^{\circ}C$. The intensity of the PL spectrum is significantly decreased, even though a low temperature deposition process (figure 4.3 left) for the deposition of only a 2 nm thin Al_2O_3 layer has been used. The normalized PL spectrum (figure 4.3 right) shows clearly the influence of the deposition process on the PL spectrum. The spectrum is slightly red shifted and the emission peaks are different. The polymer properties might be influenced by two process effects, the required elevated process temperature for the deposition of aluminum oxide layer and the possible degradation of the polymer due to the ALD precursors. A systematic study of the temperature effect and on the chemical reaction is addressed in the following investigation. The applicability of the ALD process might depend therefore on the Tg of the polymer and the chemical stability against the reactants.

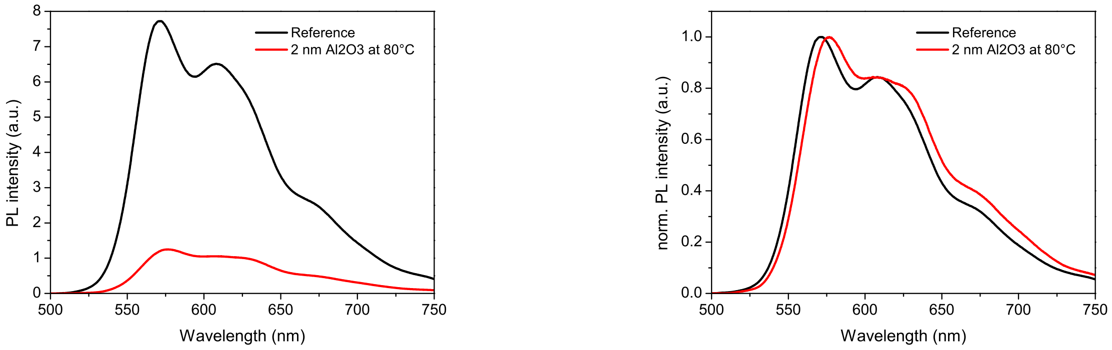

Figure 4.3: PL spectra (left) and normalized PL spectra (right) for MEH-PPV film capped with a 2 nm Al_2O_3 layer, deposited at 80 °C

The phenylsubstituted poly(para-phenylene vinylene) (PPV) copolymer ("‘superyellow"’ (SY) from Merck) shows excellent properties with a given Tg of around 175 °C which should lower the influence of the process temperature on the polymer properties. No shift of the emission wavelength has been observed in the PL spectrum when depositing at 80 °C (figure 4.4a). Often a temperature treatment below Tg is used in order to remove the residual solvent after film deposition. Such a low temperature treatment often increases the PL efficiency due to the change of the polymer morphology and its influence on the orientation of dipole moments and the degree of interchain interactions, resulting in an enhanced intensity which is clearly visible for all the processes [122]. A maximum PL intensity has been measured for the deposition of a 0.8 nm thin ALD film. An ALD process for the deposition of an Al_2O_3 thicker than 0.8 nm leads again to a slight decrease of the PL intensity. However, no damage of the underlying polymer due to the heating or the migration and reaction with TMA and/or H_2O is expected. A change of the polymer itself due to the process temperature has not been expected since the process temperature is far below the glass transition temperature of the SY.

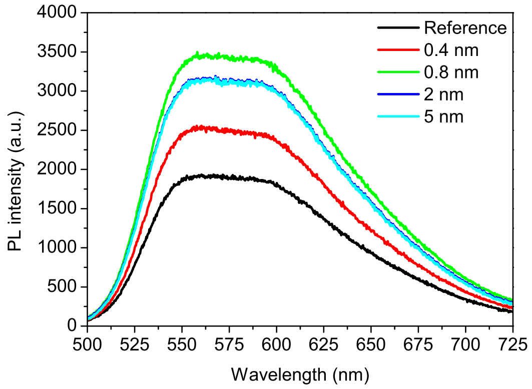

(a) PL spectra of SY after the ALD process at 80°C

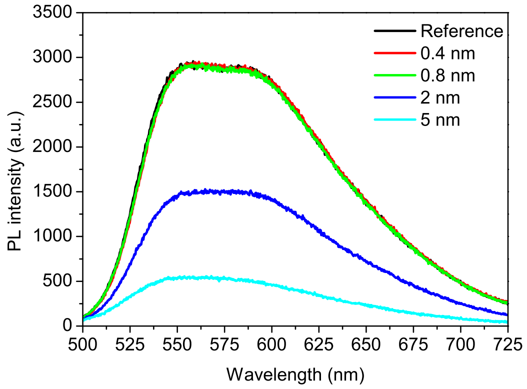

(b) PL spectra of SY after the ALD process at 150 °C

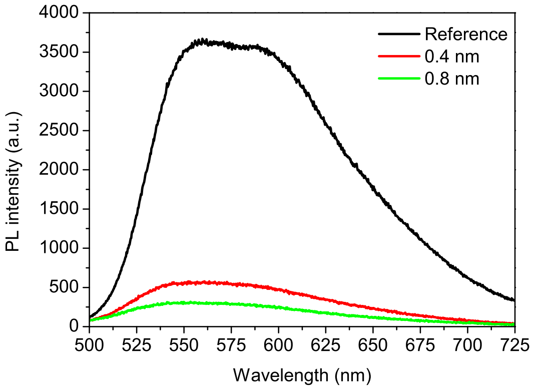

(c) PL spectra of SY after the ALD process at 235 °C

Figure 4.4: PL spectrum of Al_2O_3 covered SY, the temperature of the ALD deposition was varied between 80 °C (a), 150 °C (b) and 235 °C (c) and the thickness of the ALD layer was varied between 0.4 nm and 5 nm

It is different for a process temperature of 150 °C in figure 4.4b, which is close to the glass transition temperature of the SY polymer. The spectrum for the reference sample and the samples with a 0.4 nm and 0.8 nm ALD films are identical without any spectral shift or influence on the PL intensity. For ALD processes with thickness of 2 nm and more, the PL intensity decreases drastically and the PL emission looks slightly different regarding the shoulder at 600 nm. The peak at 560 nm and the shoulder at 600 nm are not clearly visible anymore and the PL spectrum becomes broad and unstructured. It is unlikely that the elevated process temperature decreases significantly the PL efficiency. Therefore the decrease can be very likely attributed to a chemical reaction of the ALD precursors with the polymer, which on the other hand, is a thermally activated process [120].

The maximum deposition temperature was considered to be 235 °C for obtaining a high quality Al_2O_3 layer (figure 4.4c). An expected drastic change of the PL spectrum has been observed for a high deposition temperature of 235 °C due to the ALD reactants and a process temperature which is significantly higher than Tg of the polymer. The PL intensity decreases significantly even when depositing very thin ALD film of only 0.4 nm. No spectrum could be recorded for an oxide layer thicker than 0.8 nm which corroborates again the degradation of the polymer itself due to the thermally activated stronger chemical reaction.

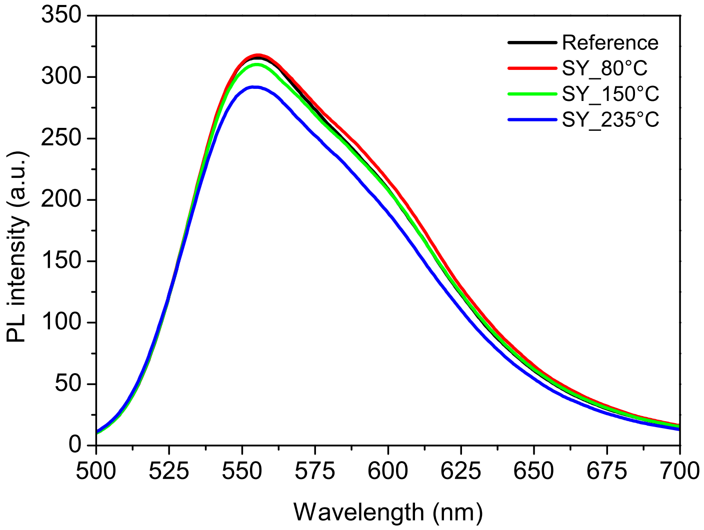

Figure 4.5: PL spectrum of temperature treated SY, the temperature of the ALD deposition was varied between 80 °C , 150 °C and 235 °C and with an identical annealing time as for the 2 nm ALD deposition process

In order to verify if the change of the PL emission spectrum comes purely from the heating effect or from the chemical reaction of the TMA with the polymer, SY has been spin-coated on a glass again and treated at 80 °C, 150 °C and 235 °C without the deposition of Al_2O_3. The annealing time at different temperatures is equal to the ALD process time, so that the effect of the temperature could be evaluated (figure 4.5). The PL spectrum of the SY does not show a wavelength shift after the temperature treatment. Only a small decrease of the PL intensity has been measured for temperature as high as 235 °C .

Both measurements (figure 4.4 and 4.5) together show that the diffusion of TMA into the polymer layer is stronger for higher temperatures and causes a strong degradation of the polymer properties. An additional decrease can be expected for a process temperature higher than Tg due to the morphological change of the polymer. Therefore, a process temperature lower than Tg should be chosen for the deposition of the Al_2O_3 in order not to damage the polymer due to the temperature and moreover the chemical reaction. The ALD-processed SY films show identical PL spectra at low deposition temperatures due to a low permeation of TMA vapors into the organic layer. M. D. Groner *et. al.* [121] have studied the effect of the low temperature on the quality of the ALD layer grown and have shown that many of the properties of the low temperature Al_2O_3 ALD films were comparable with the properties of the Al_2O_3 ALD films grown at higher temperatures of 177 °C . Good thin film properties were observed despite decreasing densities and increasing hydrogen concentrations and impurities. As a result, the ALD process of Al_2O_3 deposition should not be detrimental to the SY layer used in this work, and therefore the protection mechanism of low temperature processed Al_2O_3 ALD films is investigated in the next section.

Atomic Force Microscopy was also used to study the heating effect on the morphology of the polymer film (figure 4.6). The untreated SY film shows the highest roughness (area RMS around 2.5 nm) which decreases with higher temperatures, with 1.7 nm after a temperature treatment of 80 °C, 1.1 nm at 150 °C and with the lowest RMS roughness of 1.0 nm at 235 °C. It is clearly visible that a temperature treatment above Tg changes the morphology of the polymer film.

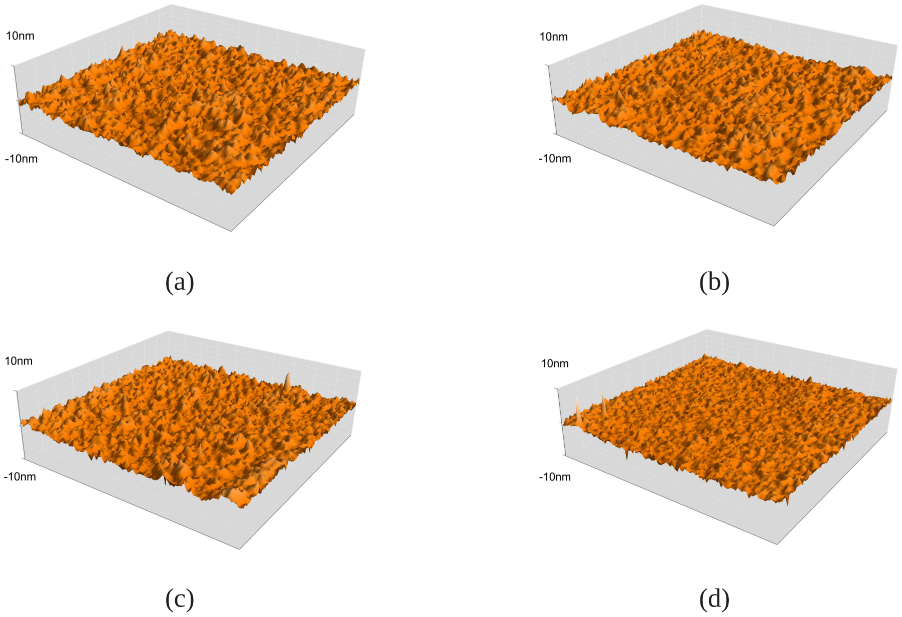

Figure 4.6: AFM images from spin-coated SY-films without annealing (a), annealed at 80 °C (b), 150 °C (c) and 235 °C (d)

The AFM images shown in figure 4.7 illustrate a good uniformity of the ALD film with a thickness of 2 nm and 5 nm all over the organic layer. Furthermore, the organic layer has a root-mean square (RMS) roughness of around 2.5 nm (figure 4.6a) without any temperature treatment, which decreases to 0.6 nm (figure 4.7b) when a thin ALD layer (2 and 5 nm) is deposited on top of it. Such parameters should be beneficial for device application in terms of the protection but, on the contrary, a 5 nm Al_2O_3 is not suitable, as Al_2O_3 is an electrical insulator [123].

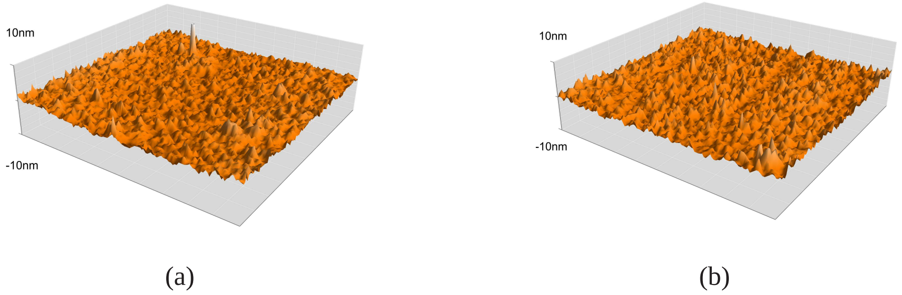

Figure 4.7: 2 nm (a) and 5 nm (b) Al_2O_3 on SY film

An Al_2O_3 film deposited at 80 °C with a thickness of 2 nm has been chosen. In the first application, the charge blocking characteristic of the Al_2O_3 layer is demonstrated with an example in the next figures before applying the film into the multilayer OLEDs. The insulation Al_2O_3 has to be thin enough to guarantee a charge carrier transport. It has been demonstrated that the breakdown electric field for the bulk aluminum oxide is around 10 MV/cm [124]. The charge carrier transport is dominated by direct charge carrier tunneling for a film thickness of up to 3 nm. Choosing a 2 nm layer thin aluminum oxide guarantees therefore a sufficient charge carrier transport and protection mechanism. Moreover, this experiment proves if the ALD deposition process at low temperature has an influence on the emission spectrum due to the migration of the TMA into the polymer layer. The device structure and the proposed band diagram are shown in figure 4.8.

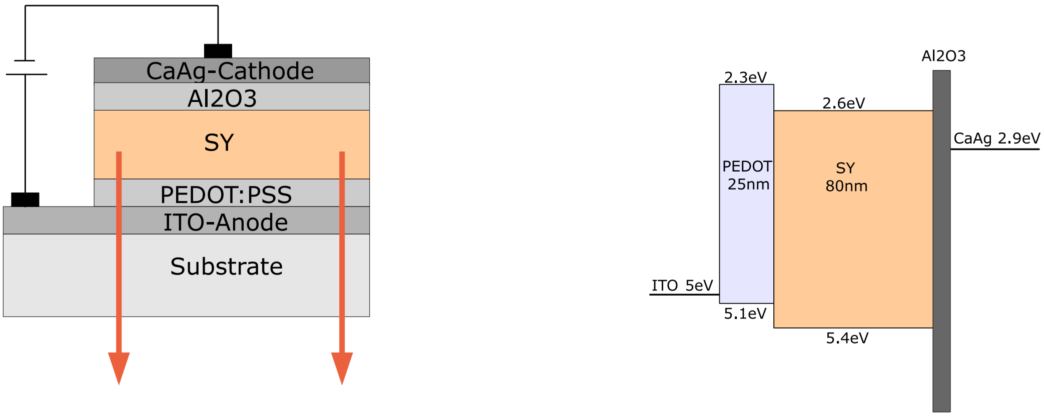

(a) (b)

Figure 4.8: OLED device structure (a) with Al_2O_3 and proposed band diagram (b)

The current density-voltage and luminance-voltage characteristic are presented in figure 4.9a. As already indicated, the current density is lowered due to the presence of the oxide layer which acts as charge blocker. As a result, the brightness of the OLED decreases significantly and its maximum is shifted towards higher voltages. The lowered brightness and the voltage shift have a significant influence on the OLED efficiency, shown in figure 4.9b. The voltage drop of around 0.5 V in the current - voltage behavior is due to the presence of the 2 nm aluminum oxide film. An applied electric field of around 25 MV/cm can be calculated which is even higher than the breakdown electrical field given in literature and therefore sufficient high for charge carrier transport.

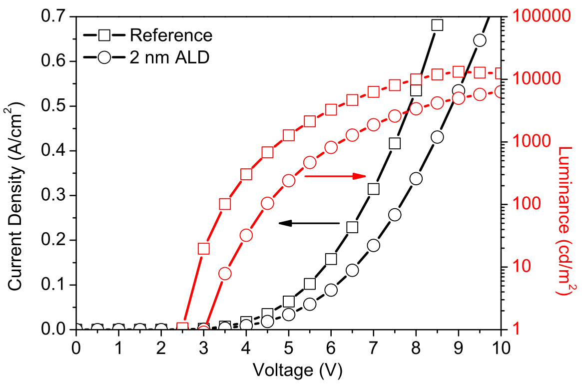

(a) Current Density-Voltage and Luminance-Voltage behavior

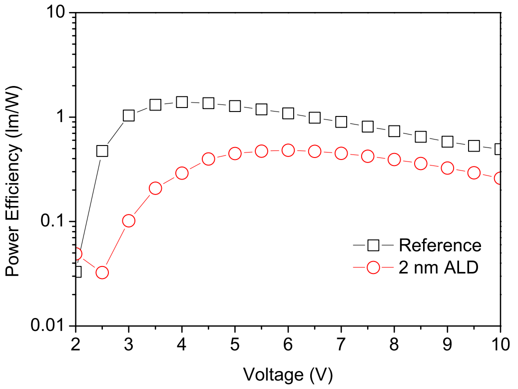

(b) Power efficiency versus applied voltage

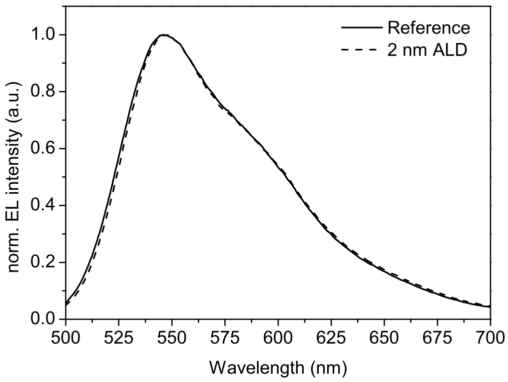

(c) normalized EL spectra taken at 8 V

Figure 4.9: OLED characteristic for OLEDs with and without a thin 2 nm Al_2O_3 layer between SY as emissive polymer and the CaAg cathode

More important is the record of the emission spectrum of the OLEDs since it shows if the ALD process changes the intrinsic properties of the polymer film or if there is a degradation of the emissive polymer while depositing Al_2O_3. When normalizing the EL spectrum of both OLEDs, shown in figure 4.9c, it can be seen that the presence of the oxide and, moreover, the ALD process itself have no influence on the emission spectrum in this simple device configuration. The effect on the OLED is therefore truly related to the blocked charge carrier transfer.The characteristics of these OLEDs are summarized in table 4.2.

	Reference without ALD	2 nm Al_2O_3
Current Density$_{max.L}$ (A/m^2)	0.8	0.76
V$_{TH}$ / V$_{max.L}$ (V)	2.5/9	3/10
max. Luminance (cd/m^2)	13220	6360
max. Efficiency (lm/W)	1.4	0.5

Table 4.2: Performance of SY-based OLEDs with and without a thin 2 nm Al_2O_3 layer between the emissive polymer and the CaAg cathode

This section shows the importance of a well-chosen process condition for the ALD process when depositing Al_2O_3 on film polymer. A degradation of the polymer takes place due to the migration and possible reaction of the TMA into the polymer. The pure use of Al_2O_3 as interfacial layer would result in a lower OLED efficiency because Al_2O_3 is an electrical insulator. However, the solution processed injection layer might compensate such an effect. This will be demonstrated in the next sections.

4.3 The ALD layer used to avoid intermixing of successive spin coated organic layers

In this section, an ALD deposited layer of 2 nm of Al_2O_3 is used as a protective layer for a polymeric film of poly(phenylenevinylene) co-polymer (SY), which was successively covered by spin coating of a second organic layer [125]. The result is the deposition by spin coating of successive organic layers, separated by an ultra-thin Al_2O_3 layer, without intermixing of the successive organic layers due to solvent dissolution.

4.3.1 Study of the solvent influence on the underlying layer.

To study the surface coverage of the ALD layer on top of SY and to show that no penetration of the solvent from the top organic layer to the bottom organic layer occurs, the following experiment was done. Various SY layer samples were prepared with a 2 nm Al_2O_3 layer deposited at 80 °C on top (figure 4.10).

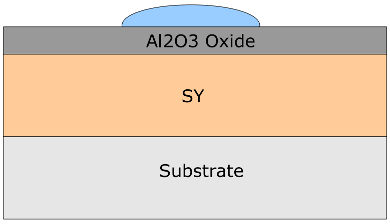

Figure 4.10: Solvent drop on SY protected by a thin Al_2O_3 layer

Figure 4.11a shows the photos of the samples prepared, which present a strong yellow coloration uniform throughout the samples.

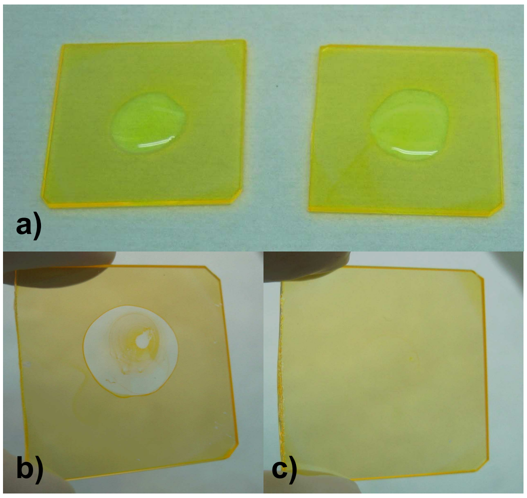

Figure 4.11: (a.) SY samples with (left) and without (right) a 2 nm thick Al_2O_3 layer, showing a strong yellow coloration. A drop of chloroform was deposited on top of both SY samples. The dissolution of the SY layer below is clearly seen, with a transparent area appearing where the toluene was deposited (b) while for the SY covered by the 2 nm thick ALD layer, no dissolution area nor defect can be seen to the SY layer (c).

A small drop of solvent was deposited on the Al_2O_3 coated SY layer, the solvent used being chloroform. Chloroform has been used as solvent for the Alq_3 electron transport/injection layer. After drying out, the solvent did not damage the bottom SY layer, which still shows the same yellow coloration uniformly all over the layer (figure 4.11c). If the SY is not protected by the Al_2O_3 layer, the small drop of solvent dissolves immediately the SY layer beneath and results in a white mark on the sample, where the polymer has been dissolved again, as can be seen in figure 4.11b [125]. Such visual proof shows very well the protective role of the Al_2O_3 layer to the organic layer beneath, with no selectivity regarding the solvent used.

Figure 4.12 shows the effect of the solvents on the PL spectrum for samples with or without a protection layer. A strong deterioration of the PL spectrum has been observed for the unprotected SY layer due to the partial dissolution of the SY-film by the solvent. A very strong decrease has been observed when depositing $CHCl_3$. Looking at the normalized PL spectrum (figure 4.12b), a strong shift of around 14 nm has been measured.

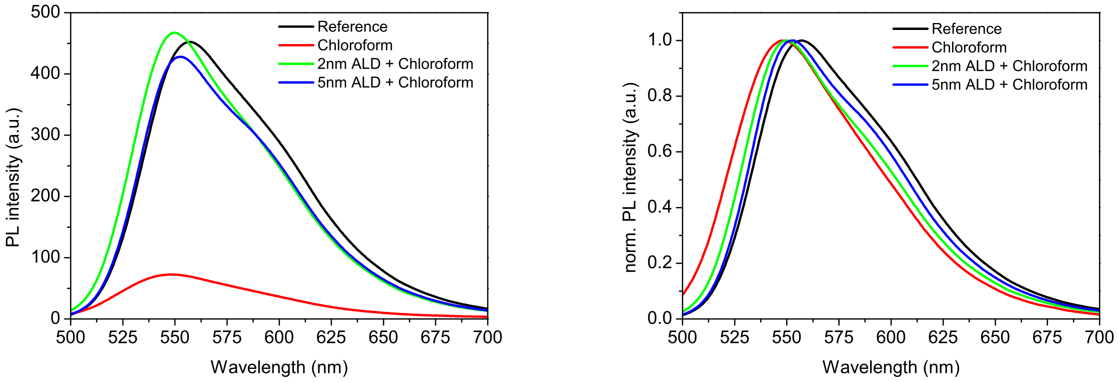

(a) (b)

Figure 4.12: PL spectrum of SY samples after depositing chloroform and using a 2 nm/ 5nm thin ALD layer as protection, PL spectrum (a) and normalized PL spectrum (b)

	SY	SY + $CHCl_3$	SY + 2 nm Al_2O_3 + $CHCl_3$	SY + 5 nm Al_2O_3 + $CHCl_3$
FWHM (nm)	80	77.5	76	77.5
max. PL (nm)	557	549	550	552.5

Table 4.3: FWHM and the wavelength at the maximum PL emission for the reference SY film, SY treated with $CHCl_3$ and protected with a 2 nm and 5 nm Al_2O_3

A thin 2 nm Al_2O_3 layer provides already a protection against solvents. However, the protection is only lowering the impact of the solvents, since a partial penetration of the solvents into the polymer cannot be avoided [119][126]. The PL enhancement when depositing a 5 nm film is the result of the temperature effect at 80 °C, which has been already observed in the previous section. The shape of the emission spectrum is similar for all samples, however, a small shift of the emission spectrum of 7 nm has been still observed due to a partial dissolution of the polymer surface (figure 4.12b). A 5 nm thick oxide layer provides obviously a stronger protection resulting in a decreased spectral shift of only 4.5 nm.

In both cases, the emission intensity was higher using a thicker Al_2O_3 *layer resulting in a more efficient protection. No shift of the emission spectrum was observed and the emission maximum stays at the same wavelength [127]. Even though it is evident, that a more efficient protection of the organic layer against solvents is provided by thicker* Al_2O_3 *layers, it has to be noted that* Al_2O_3 *is an electrical insulator. Thus, for the multilayer OLEDs, a 2 nm thin* Al_2O_3 *is deposited as protection layer in the following subchapter providing sufficient protection, but still not blocking all the charges.*

4.3.2 Application to multilayer OLEDs; avoidance of intermixing of the layers

Most of the standard OLED polymers favor hole-transport leading to a charge carrier unbalance in the device, which results in poor efficiencies. The standard approach to improve the efficiency of OLEDs is to insert an electron transport and/or injection layer (ETL) at the cathode interface in order to improve the electron transport and/or injection. Such EIL/ETL may consist of an organic molecule, which is thermally evaporated, or barium or calcium, which are highly reactive materials. In this chapter, the possibility to use a spin coated thin film of tris(8-hydroxyquinoline) aluminum (Alq_3) as ETL is investigated by using a thin 2 nm Al_2O_3 deposited between the two spin coated layers. Alq_3 blocks efficiently the holes due to its deep HOMO level and it is also a good electron transport layer, commonly used in small molecule OLEDs [128]. Using Alq_3 as interfacial layer should therefore provide an improved balance between electron and holes, leading to a shift of the recombination zone towards the polymer center instead of being close to the cathode [129]. Alq_3 has been spin-coated without any protection onto the polymer film (figure 4.13b). Furthermore, a Al_2O_3 layer within the OLED has been prepared (figure 4.13c) and, as the final device, an OLED with the complete stack of SY, Al_2O_3 and Alq_3 has been investigated (figure 4.13d).

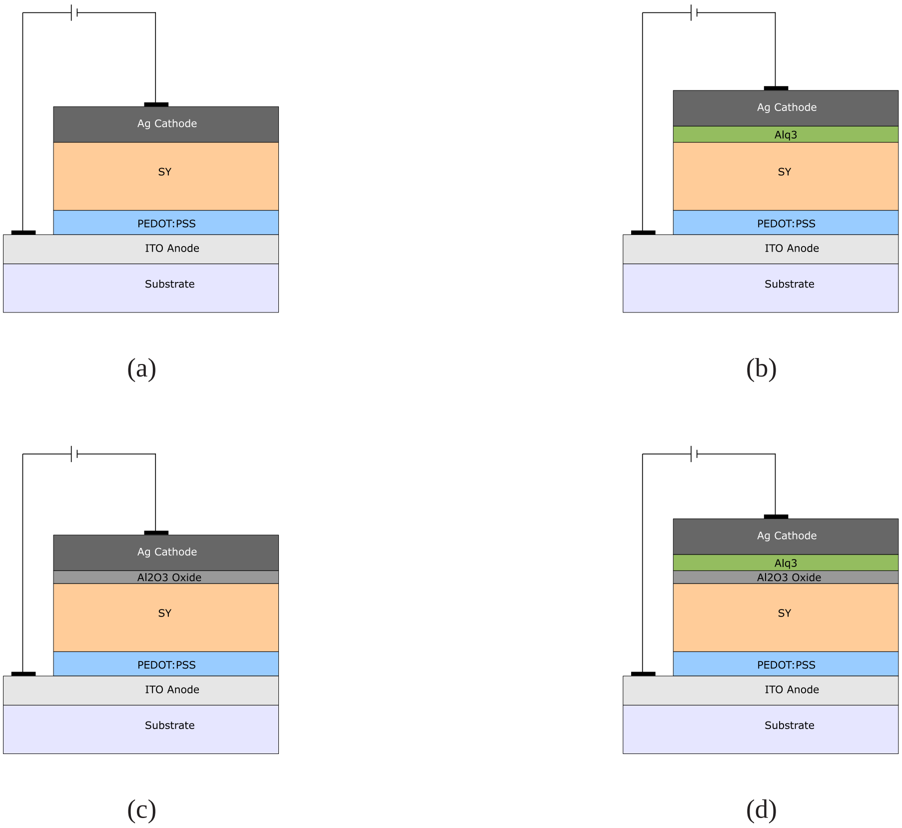

Figure 4.13: (a) OLED structure without ALD and without electron injection layer as reference, (b) with Alq_3 injection layer and without ALD protection layer, (c) with Al_2O_3 as protection layer and without an electron injection layer, (d) solution processed Alq_3 electron injection layer on a Al_2O_3 protected SY polymer film

The band diagram is schematically shown in figure 4.14. Figure 4.14a shows the simple OLED structure without having any interfacial layer for an increased electron injection and transport. The energy bandgap between the LUMO level of the polymer and the workfunction of the Ag cathode is big, resulting in a poor electron injection. A different behavior can be expected when looking at the band diagram in figure 4.14b after inserting Alq_3 as electron injection material. The energetic step between the fermi-level of Ag and the LUMO of Alq_3 is slightly smaller than that to the LUMO of SY. The Alq_3 does not only improve the electron transport towards the emissive polymer, additional it will also improve the poor electron injection. Furthermore, the holes are blocked at the polymer/ALD/Alq_3 interface due to the Alq_3's deep HOMO level.

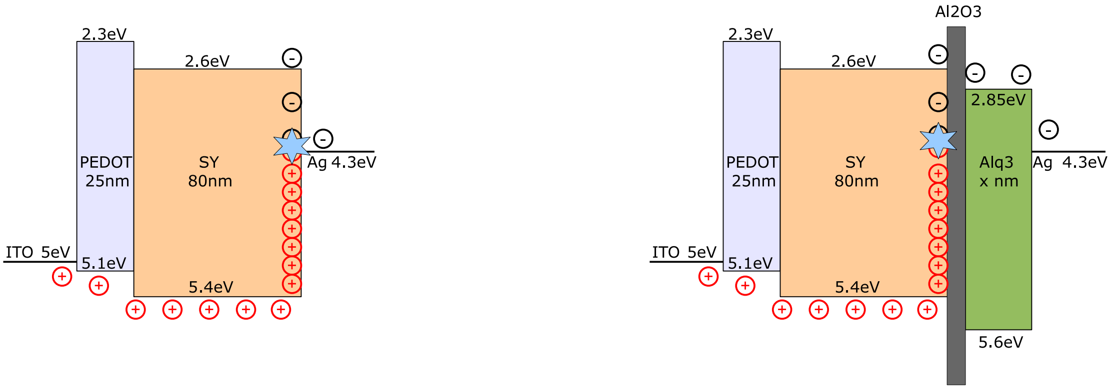

(a) (b)

Figure 4.14: proposed band diagram for the reference OLED (a) and the improved OLED with Al_2O_3 as protection layer and Alq_3 as electron transport layer (b))

The measured current and luminance behavior is shown in the figures 4.15a and b. Additionally, the power efficiency of these OLEDs has been calculated in figure 4.15c. The OLED efficiency for the device structure (a) and (c) is poor due to the large energy gap between the cathode and LUMO level of the polymer. The poor injection of electrons in (a) is even more hindered by adding an ALD deposited oxide between the polymer and the cathode in (c). Al_2O_3 blocks efficiently the charge transport even for very thin layers. Therefore, the efficiency in (c) is even lower than in (a) due to the higher required voltages and the lower luminance. However, introducing an electron injection layer (for instance, Alq_3) does not necessarily mean that the OLED efficiency will increase; this can be seen for the OLED (b). The solution processed Alq_3 layer was spin-coated onto the polymer film. The SY film was therefore partially dissolved by the Alq_3 film, as already demonstrated in figure 4.11b. The efficiency of this OLED is very low, with additionally a strong increase of the threshold voltage for the light emission. It can be seen that the device performance is significantly improved when inserting a 2 nm thin Al_2O_3 layer between the SY and the Alq_3 layer (d). Not only does the current density decrease, but additionally the luminance level is significantly increased leading to an efficiency enhancement of one order of magnitude (figure 4.15c) from 0.016 lm/W for the reference device up to 0.17 lm/W for the multilayer OLED. When electrically excited, the maximal luminance of 243 cd/m^2 measured at 9.7 V for the reference (a) increases up 1445 cd/m^2 at the same voltage and with a maximum possible luminance of 4734 cd/m^2 at 12.1 V for the multilayer OLED (d).

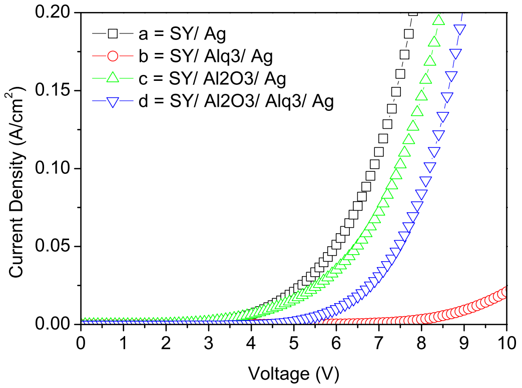

(a) Current density versus applied voltage

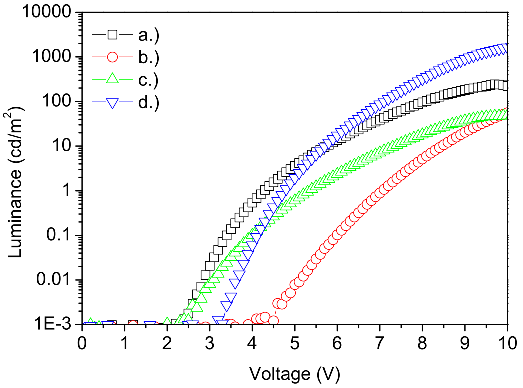

(b) Luminance versus applied voltage

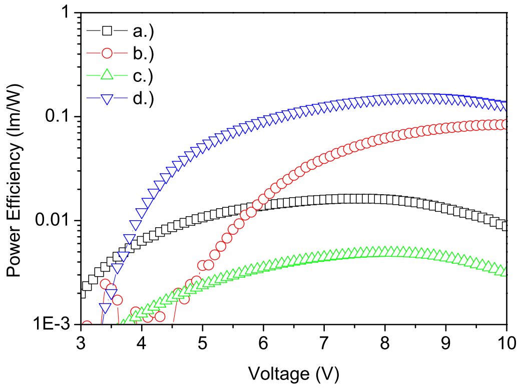

(c) Power efficiency versus applied voltage

Figure 4.15: OLED characteristic for OLEDs with and without a thin 2 nm Al_2O_3 layer between SY as emissive polymer and Alq_3 as electron injection layer, a.), b.), c.) and d.) referring to the OLED architecture shown in figure 4.13.

The underlying SY-polymer film has been therefore successfully protected by a 2 nm thin Al_2O_3 film so that a solution processed Alq_3 could be deposited on top leading to a significant efficiency increase of the OLED. A decrease of the luminance after reaching its maximum has been observed and it has been explained literature by the interfacial charge accumulation [130]. This is more likely the case when the thickness of the layers is not optimized or when the energy levels are not optimally aligned.

Additionally, the EL spectra have been measured in order to test if the additional layers (ALD + Alq_3) have an impact on the emission spectrum (figure 4.16). There is no shift of the emission wavelength and no additional emission comes from the Alq_3 in the lower wavelength range. The slight increase at around 600 nm might be a contribution of the additional layers on the optical properties of the stack.

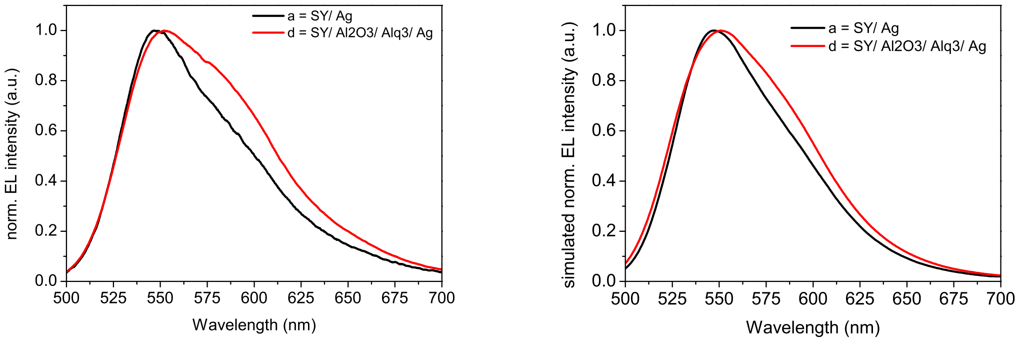

(a) (b)

Figure 4.16: measured (a) and simulated (b) electroluminescence spectrum for the reference OLED and the OLED structure using Al_2O_3 as interfacial layer, a.)and d.) referring to the OLED architecture shown in figure 4.13.

The optical simulation corroborates the above assumption. A measured photoluminescence quantum yield for the spin-coated superyellow polymer film of 22.5 % has been considered for the simulation. The optical constants for each material can be found in the appendix. The out-coupled EL spectrum has been simulated using the device parameters (thickness of each layer) as well as the measured photoluminescence spectrum of the SY-film. The developing of the shoulder between 550 nm and 650 nm on the spectrum of the multilayer film is therefore purely related to the introduced Alq_3 layer with its specific optical constants (figure A.5) as the simulation proved. Additionally, conclusions on the electronic properties of the device stack when introducing Alq_3 can be drawn using the simulated EL spectrum. The relative dipole position (relative distance from the PEDOT:PSS - polymer interface) can be calculated using the simulation software. For the device structure shown in figure 4.13a, a relative dipole position of around 0.95 (corresponds to 76 nm distance from the PEDOT:PSS - polymer interface) has been calculated, while the relative dipole position was clearly shifted towards the PEDOT-Polymer interface with a value of 0.28 (corresponds to 22 nm distance from the PEDOT:PSS - polymer interface) for the multilayer device in figure 4.13d. Therefore the inefficient recombination mechanism close the metallic cathode (in terms of radiation) has been lowered due to the presence of the Alq_3. A dipole position close to the metallic electrode leads to a coupling to surface plasmon polaritons (SPP).

Additionally, these values have been taken for the calculation of the outcoupling fraction of the emitted power over the wavelength and as a function of the dipole position (figure 4.17).

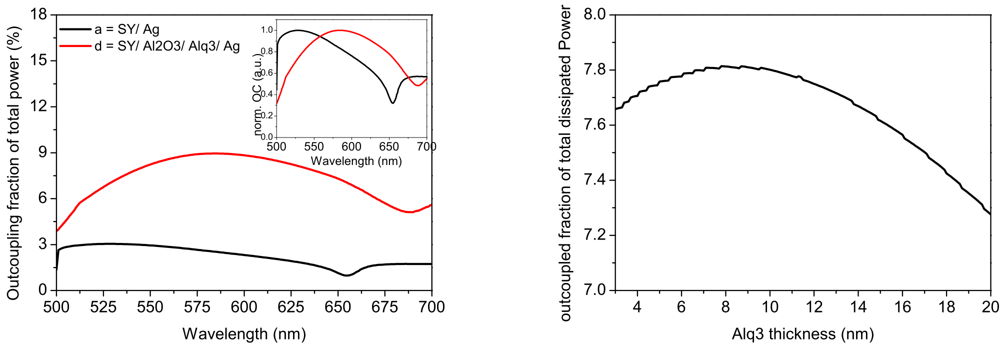

(a) (b)

Figure 4.17: Simulated outcoupled power fraction as a function of the wavelength for the reference OLED and the multilayer OLED (a). Simulated outcoupled power fraction as a function of the Alq_3 thickness (b)

The intensity of the optical outcoupling shows a significant difference between the devices. The OLED shown in 4.13a has a calculated average outcoupled power fraction of only 2.2 %, which is significantly lower than 7.7 % for the multilayer OLED. It is therefore very likely that the multilayer OLED structure not only increases the charge carrier balance, resulting in a recombination zone shift towards the center, but also it improves the intensity of the outcoupled power. The outcoupled power is shown as a function of the wavelength for both OLEDs. It can be seen that for the multilayer OLED, the highest outcoupled power fraction of almost 9 % has been reached at around 590 nm, which is actually exactly the wavelength where a shoulder appears for this device configuration (see inset 4.17a). The behavior of the outcoupled power for the multilayer OLED is shifted towards longer wavelength resulting in a shoulder at around 600 nm for the electroluminescence spectrum.

Again, the presence of the interfacial layer Al_2O_3 and the EIL/ETL Alq_3 leads to a shift in the emissive dipole position resulting in an enhancement of the outcoupled power. The average outcoupled power varies depending on the thickness of the Alq_3 with a maximum of around 7.8 % for an Alq_3 thickness of around 8 nm. The intensity of the outcoupled emission varying the Alq_3 thickness and emitter dipole position has been additionally simulated (figure 4.18). The highest emission intensity (dark red) has been simulated for a dipole position between 16 - 32 nm distance from the PEDOT:PSS - polymer interface and an Alq_3 layer thickness lower than 10 nm, which is in an good agreement with the previously presented device structure.

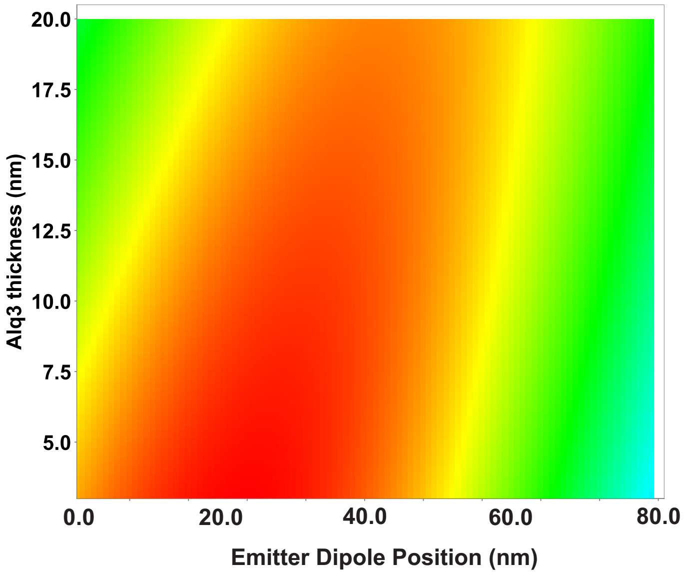

Figure 4.18: outcoupled power intensity as a function of the Alq_3 thickness and dipole position with the distance from the PEDOT:PSS - polymer interface

The dipole position has been shifted away from the electrode as calculated before resulting in a significant increase of the outcoupling power. The measured device characteristics are summarized in table 4.4.

OLED	$J(L_{max})$ (A/m^2)	V_{TH} / $V_{max.Lce}$ (V)	L_{max} (cd/m^2)	max. Eff (lm/W)
a.) Reference	0.76	4.3/ 9.7	243	0.016
b.) Alq_3 1 mg	0.9	7.1/ 13.8	198	0.08
Alq_3 3 mg	0.3	10.6/ 19.4	113	0.07
c.) ALD	0.8	5.3/ 13.6	134	0.005
d.) ALD + Alq_3 (5 nm)	0.73	4.8/ 12.1	4734	0.17
ALD + Alq_3 (8 nm)	0.49	5.3/ 13.2	3886	0.19
ALD + Alq_3 (10 nm)	0.12	8.2/ 15.2	701	0.15

Table 4.4: experimental results of SY-based OLEDs with and without a 2 nm Al_2O_3 layer as protection, varying the concentration of the spin-coated Alq_3 film

The subsequent spin-coating Alq_3 layer onto a Al_2O_3 protected SY polymer film has been successfully implemented into the OLED structure. Such a configuration has shown the expected enhancement in the device efficiency due to the presence of the ETL/EIL. The relative dipole position was clearly shifted from being very close to the SY - Al_2O_3 interface towards the SY - PEDOT:PSS interface as simulated before. Such a shift of the emissive dipole position indicates an improved charge carrier balance. The result shows the potential of the ALD as protection and/or interfacial layer. A significant increase of the OLED efficiency has been measured; however, the effect has to be investigated for different polymers due to their different required process conditions (for instance, temperature and used solvents).

As another example, MEH-PPV shows very poor electron conduction. OLEDs with MEH-PPV as emissive material and without an electron injector hardly emit light. The band diagram as well as the device structure is shown in figure 4.19. The band diagram shows a big energy gap between the LUMO level of the MEH-PPV and the workfunction of the Al-cathode without an electron injection layer. The same idea has been applied, as demonstrated previously. Alq_3 was spin-coated onto the Al_2O_3 protected MEH-PPV layer and the OLED performance has been compared with the reference OLED (figure 4.20). Taking into account the low Tg from MEH-PPV, the impact of the ALD process will be more significant as demonstrated in figure 4.3.

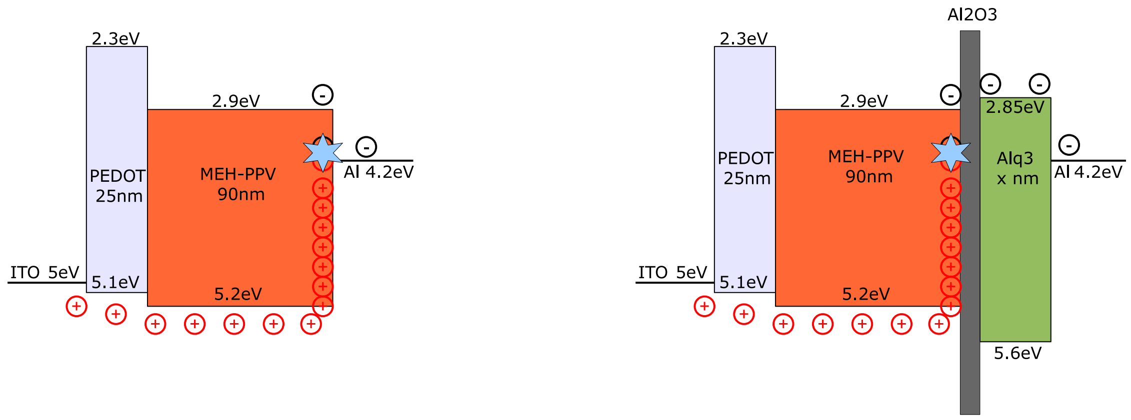

(a) (b)

Figure 4.19: proposed band diagram for the reference OLED (a) and the improved OLED with Al_2O_3 as protection layer and Alq_3 as electron injection (b)

The reference OLED shows very poor behavior with a very low efficiency of around 0.002 lm/W. The maximum luminance of the multilayer OLED is significantly higher with around 900 cd/m^2, resulting in an increase of the power efficiency of around one order of magnitude. The efficiency is still quite low taking into account that the layer thicknesses and process conditions have not been optimized so far. However, the improvement is quite significant and is related to the shift of the dipole position away from the Al-cathode due to the introduction of the interfacial Al_2O_3. The decrease of the luminance for the MEH-PPV reference OLED is due to the degradation of the OLED after reaching its maximum. The results, including the current density at the maximum brightness, are summarized in table 4.5.

Material	MEH-PPV	MEH-PPV + ALD + Alq_3
Current Density$_{max.Lce}$ (A/m^2)	0.3	0.68
V_{TH} / $V_{max.Lce}$ (V)	4.5/ 7.5	3.5/ 12
max. Luminance (cd/m^2)	9	880
max. Efficiency (lm/W)	0.002	0.035

Table 4.5: Performance of MEH-PPV-based OLEDs with and without a thin 2 nm Al_2O_3 layer between the emissive polymer and the cathode

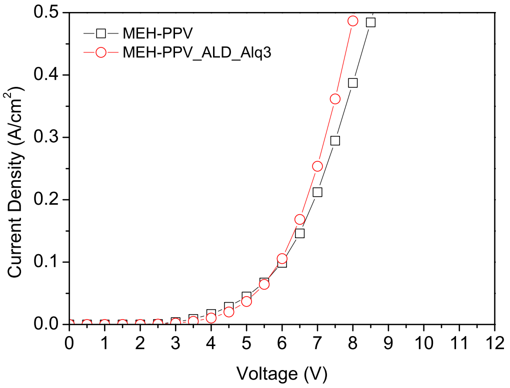

(a) Current density versus applied voltage

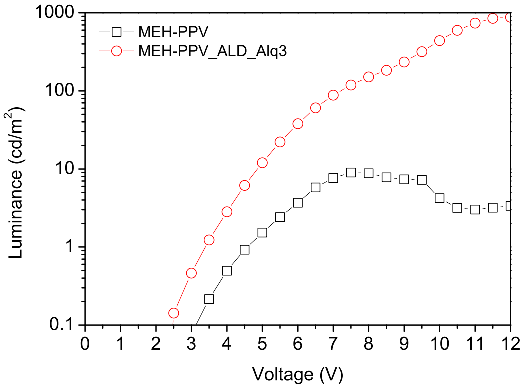

(b) Luminance versus applied voltage

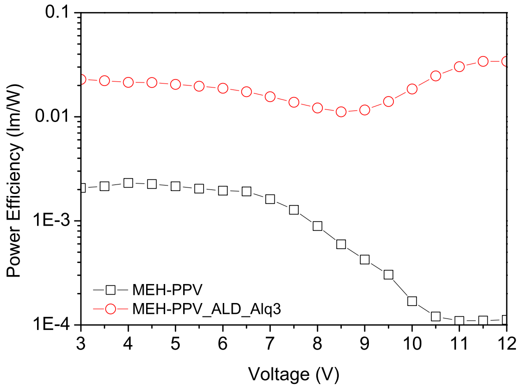

(c) Power efficiency versus applied voltage

Figure 4.20: OLED characteristic for OLEDs with and without a thin 2 nm Al_2O_3 layer between MEH-PPV as emissive polymer and Alq_3 as electron injection layer

Both OLED structures show an increase of the efficiency when using Al_2O_3 *as protection layer and a solution processed* Alq_3 *as electron injection layer. It has been demonstrated that an ALD deposited* Al_2O_3 *film prevents efficiently the degradation of the underlying polymer when spin-coating a layer on top. Additionally, the charge blocking mechanism of the* Al_2O_3 *layer has to be considered due to its insulation character. Solution processed* Alq_3 *compensates therefore the charge carrier blocking effect of the ALD film leading to a significant enhancement of the luminance and results in a strong increase of the efficiency. Therefore, a good trade-off has to be found between the protection mechanism and the charge blocking mechanism of the oxide layer.*

4.4 Conclusion

In this chapter multi-layered, solution processed OLEDs are developed. Thin intermediate metal-oxide layer prepared by ALD are used to avoid solvent induced degradation of the organic layers. This chapter deals with mainly two issues: 1.) finding the right process condition of the ALD process for the deposition of oxides onto a polymer layer, and 2.) defining an oxide layer thickness with sufficient protection properties and the charge carrier blocking behavior of the oxide within the OLED structure. Those ultra-thin ALD films were deposited at low temperatures at 80 °C in order to avoid degradation of the bottom organic layer. The degradation of the polymer results in a change of the PL-spectrum and has been measured for two polymers with different Tg. It was shown that a 2 nm ALD film on a polymer is very uniform with low roughness. The deposition process of the Al_2O_3 at low temperatures onto SY does not degrade the polymer. A strong degradation of the SY-polymer was found when using higher temperature for the thermally activated chemical reaction during the ALD process. A very low permeation to various solvents through the oxide onto the underlying SY-polymer has been demonstrated. Furthermore, this technique has been applied to the OLED fabrication process, attempting to fabricate both the emissive layer and the electron transport layer by successive spin coating. No intermixing was observed between the two organic layers due to the thin ALD film deposited between them. The device showed an improved luminance and efficiency, which has been expected due to the presence of the ETL. An enhancement has not been observed when the ETL is applied directly on top of the emissive organic layer. The simulation shows that the recombination zone is shifted away from the metallic cathode towards the PEDOT:PSS - polymer interface by the presence of the ALD and Alq_3 layer. The additional Al_2O_3 and Alq_3 layers lead to a shift of the emissive dipole position away from the polymer-metal cathode resulting in an significant decrease of the non-radiative losses due to the surface plasmon coupling on the metal cathode surface. Additionally, the outcoupling intensity is significantly increased leading to a twentyfold increase of the luminance and a higher efficiency of the OLED of around one order of magnitude. The same concept has been proven using a less efficient polymer, named MEH-PPV. An increase of the efficiency and brightness in the same order of magnitude has been measured and corroborates the previously made assumption. Thus, the method reported here improves the applicability of atomic layer deposition in OLED fabrication and the possibility of using solution processed multilayer for an enhancement of the OLED efficiency.

Chapter 5

Blend of a polymer and an organic small molecule as emissive layer for OLEDs

A simple approach for the fabrication of efficient OLEDs is the use of blended organic material in order to avoid multi-layer structures and decrease the complexity of the device architecture. Many conjugated light emitting polymers are hole conductive showing a low electron mobility. Low electron mobility leads to an unbalance of electrons and holes in an OLED device structure, resulting usually in a shift of the position of the recombination zone towards the cathode. The recombination close to the electrode is known to be inefficient [131]. An increase of the OLED efficiency can be achieved by doping the polymer with an electron transport material. Both, the carrier injection and transport can be improved by carefully selecting the materials and their concentration in the blended polymer [132][133]. Among conjugated polymers, 2-methoxy-5-(2-ethylhexyloxy)-p-phenylene vinylene (MEH-PPV) has been extensively investigated [134][135] as host material for polymer blend based devices due to its efficient EL emission and for its hole transport properties. MEH-PPV as host material was blended with an electron-transport or hole-blocking material (usually a non-emissive material).It shows a significant enhancement of the device efficiency when used as emissive layer [132][136]. For instance, the device efficiency was increased by blending MEH-PPV with a newly synthesized electron-transport material (DFD) or with a hole-blocking material [137][138], but the voltage for the maximum light emission was shifted towards higher voltages.

In this chapter, MEH-PPV doped with the small molecule electron conductor tris(8-hydroxyquinoline) *aluminum Alq_3 was used as active material for the OLED [139]. Both materials are often used as emissive layer either for solution processed OLEDs in the case of MEH-PPV or for vacuum processed small molecule OLEDs for Alq_3. An efficient energy transfer from the Alq_3 to the MEH-PPV is expected due to the overlap of the emission spectrum of the Alq_3 and the absorption spectrum of the MEH-PPV [140]. The blend has been investigated by means of electroluminescence and fluorescence spectroscopy upon variation of the Alq_3 content in the blend. Used in OLEDs, such a blend shows a significant enhancement for the luminance and power efficiency.*

5.1 Experimental details

The OLED fabrication procedure is identical to that described in the previous chapters. The conjugated polymer 2-methoxy-5-(2-ethylhexyloxy)-p-phenylene vinylene, namely MEH-PPV, was blended in different weight concentration with Alq_3 (both from Sigma Aldrich) and dissolved in chloroform $CHCl_3$. The formulations have been stirred overnight and then spincoated on the PEDOT:PSS layer with no ramp time and 2500 rpm for 30 s. Aluminum (Al) was used as cathode and was thermally evaporated through a shadow mask. The device structure and the finished device are shown in figure 5.1a,b.

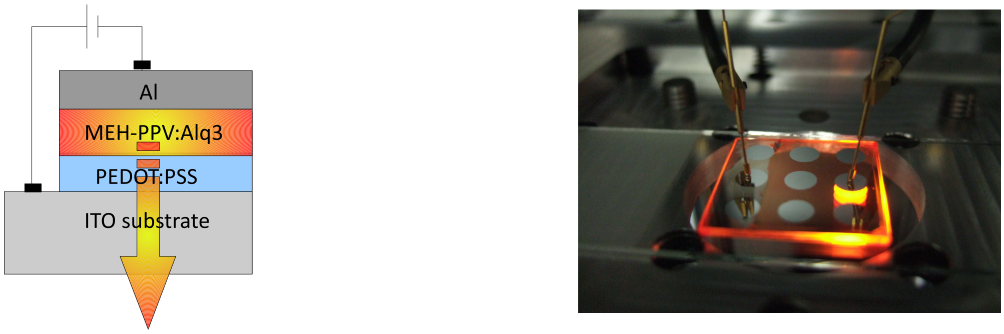

(a)

(b)

Figure 5.1: device structure for blend-based OLED (a), working device after fabrication (b)

5.2 Spectroscopy Study of the Energy transfer mechanism between the polymer and the organic small molecule

The absorption and emission spectrum for Alq_3 and MEH-PPV measured for a thin spin-coated film are shown in figure 5.2. A strong overlap of the emission spectrum of the Alq_3 with absorption spectrum of the MEH-PPV is indicated with the red hatch. The absorption maximum of the MEH-PPV was measured to be at 500 nm while the maximum emission wavelength of the Alq_3 is at 540 nm.

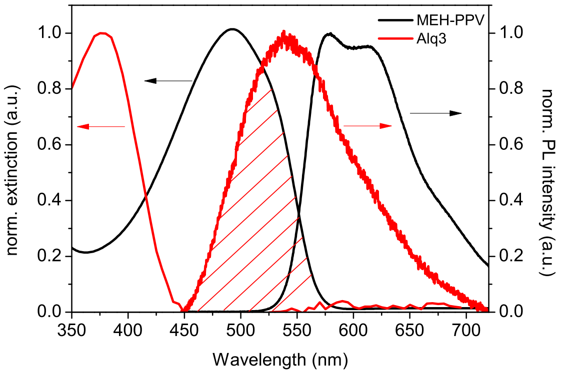

Figure 5.2: optical absorption and photoluminescence for MEH-PPV and Alq_3

A broad emission peak can be seen in the photoluminescence spectrum of the MEH-PPV film with a maximum at 580 nm and a weaker peak at around 620 nm. The features at 580 and 620 nm are assigned to the transition from the lowest vibrational level of the first excited electronic state to the lowest vibrational level of the ground electronic state $(0 \rightarrow 0)$ and a combination of its vibronic replica $(0 \rightarrow 1)$ and an increasing interchain interaction due to the polymer aggregation when spin-coated as a film, respectively. This fluorescence signal with its characteristics is the result of the convolution of the emission of intrachain excitons and interchain species due to the possible exciton transport along and between the polymer chains. As a result, the usually measured sharp spectrum with a clear resolution of the vibronic features, as measured for instance in very low concentrated polymer solution (M. Yan, *et.al.* Phys. Rev. Lett. 75, p.1992 (1995)) or single MEH-PPV polymer chain, is broadened due to a strong interchain interaction in the polymer film [154]. Since interchain interactions lead to the formation of lower-energy excited (resulting in a redshift) states coupled only weakly to the ground state, they are generally considered to lower the luminescence efficiency. An increasing doping concentration might influence therefore the interchain contribution due to the separation of the polymer chains. This effect and, as a consequence, resulting influence on the emission spectrum and device performance is investigated during this chapter.

The optical properties have been measured for MEH-PPV as host material. MEH-PPV was then blended with Alq_3 as electron conductive material in different concentrations (9 %, 17 %, 33 %, 50 % and 60 % weight ratio), spin-coated on glass. The normalized absorption spectrum does not show any change for the maximum absorption peak, even for a very high blend concentration (figure 5.3a). The maximum absorption remains located at 500 nm for the blended MEH-PPV. A second absorption peak at 380 nm appears for the blend with an increasing Alq_3 amount.

The interaction between two different molecules of the same species (MEH-PPV) doped by the electron transporter Alq_3 was investigated by studying the fluorescence measurements. The presented blended system meets the necessary conditions of Förster-type energy transfer due to the strong overlap of the donor emission and the absorption spectrum of the acceptor molecule. For Alq_3 concentrations in the range up to 60 %, the blend fluorescence shows similar spectral features as the pure MEH-PPV as it has been demonstrated already in figure 5.2. No substantial contribution from Alq_3 is found when looking at the photoluminescence spectrum of the blend layer (figure 5.3b). The normalized spectra reveal that the long-wavelength contribution at 620 nm becomes weaker with increasing Alq_3 concentration. This may be the result of an increased separation of individual polymer chains due to the increasing presence of Alq_3 molecules and a resulting reduced chain-chain interaction (figure 5.3c) [141]. A strong aggregation (low separation of the polymer chains) might, additionally to vibrational feature, lead to an increased number of weakly emissive species [152]. As the polymer chains become separated by the electron transporting small molecules, the emission appears to be dominated by single chain MEH-PPV exciton. No emission coming from the Alq_3 is visible for all concentrations.

The FWHM has not been significantly changed when doping the MEH-PPV with Alq_3, as shown in table 5.1. The reference MEH-PPV layer shows a maximum first PL peak at 580 nm with a calculated FWHM of around 104 nm. These values vary slightly in a range of around 3 nm for all blend concentrations. It can be therefore concluded that adding Alq_3 as electron transport material in low concentrations does not change significantly the PL spectrum of the host MEH-PPV material.

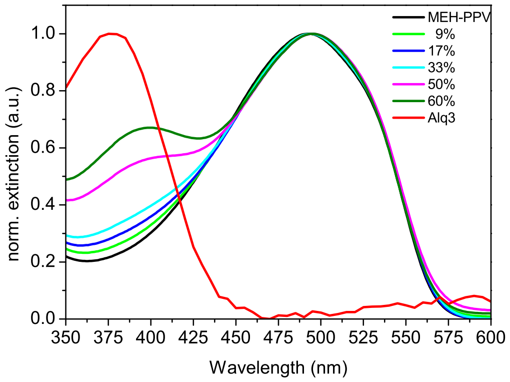

(a) normalized absorption spectrum MEH-PPV:Alq$_3$ blended films for Alq$_3$ contents from 5% up to 60%.

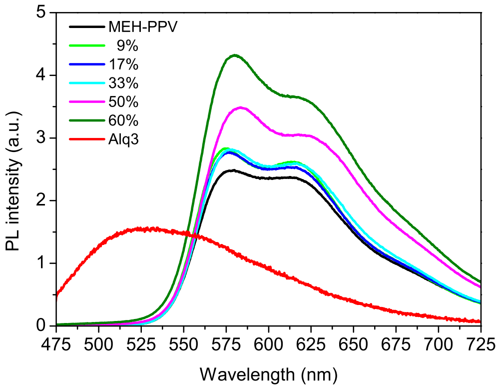

(b) CW PL of Alq$_3$ (solid red curve) MEH-PPV (solid black curve) and the blend for Alq$_3$ contents from 5% up to 60%.

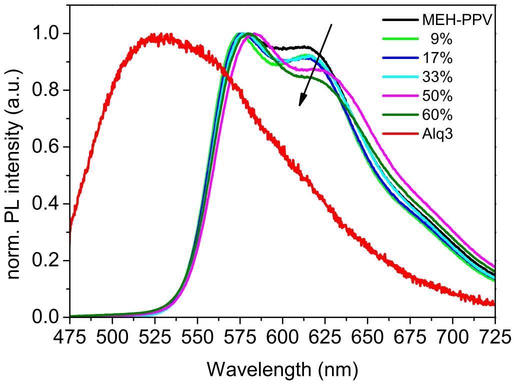

(c) normalized PL spectrum of blended MEH-PPV

Figure 5.3: (a) extinction spectrum, (b) PL spectrum and (c) normalized PL spectrum for MEH-PPV:Alq$_3$ blended films for Alq$_3$ contents from 5 % up to 60 %.

	MEH-PPV	9 %	17 %	33 %	50 %	60 %
FWHM (nm)	104	101	100	103	110	107
max. PL (nm)	580	574	577	578	583	580

Table 5.1: FWHM and the wavelength at the maximum PL emission intensity for the blended MEH-PPV

A more detailed analysis on the emission contribution is provided by looking at the time-resolved PL (TRPL). The emission has been detected at the emission maximum of the MEH-PPV at 570 nm. The excitation has been varied between the absorption maxima of the Alq_3 (400 nm) or MEH-PPV (500 nm), respectively. The TRPL shows the influence of the small molecule Alq_3 on the luminescence kinetics of the MEH-PPV as emission layer. The blended layer shows an exponential behavior and the decay function could be fitted by three main components with their specific percentile contribution. The calculated values for different blend concentrations are listed in tables B.1 - B.4 in the appendix.

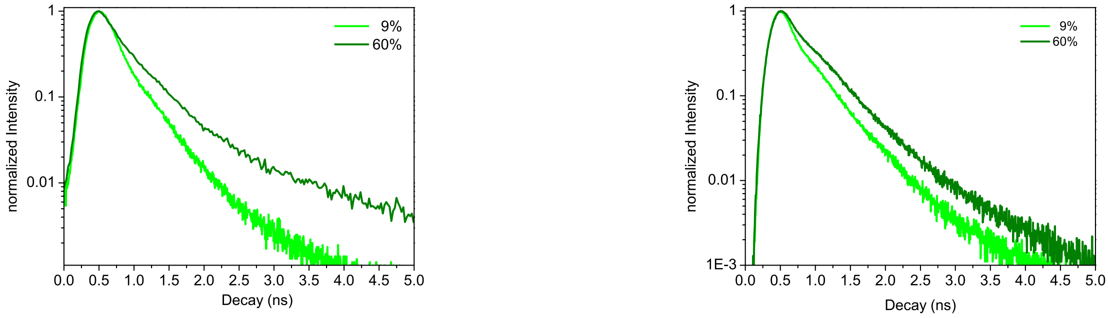

(a) Excitation wavelength 400 nm, detection wavelength 570 nm

(b) Excitation wavelength 500 nm, detection wavelength 570 nm

Figure 5.4: PL decay for the MEH-PPV emission detected at 570 nm and with a blend concentration of 9 % and 60 %, excitation at the absorption maximum of the Alq_3 (a), excitation at the absorption maximum of the MEH-PPV (b)

The PL decay is additionally divided in three different proportions after the exponential fitting analysis. The tables in the appendix give an overview of the percentage of the PL decay component with a certain delay t_n. For instance, 63.6 % of the generated photons required 0.15 ns for the decay, 30.9 % of the generated photon required an average time of 0.42 ns while only 5.5 % of the generated photons required an average decay time of 1.1 ns, for pure MEH-PPV and an excitation wavelength of 400 nm. Figure 5.4a shows the time-resolved PL decay profiles of the MEH-PPV fluorescence (probed at 400 nm) of the MEH-PPV:Alq$_3$ blend with a concentration of 9 % and 60 %. It is clearly visible that the decay time of the blend films are significantly increased for a concentration of 60 % of Alq$_3$. The time constants of the decay components increase to maxima of 0.16, 0.47 and 1.98 ns (at 60 % of MEH-PPV:Alq$_3$) compared to 0.14, 0.4 and 1.5 ns for the lower concentration (table B.1). The fluorescence decay kinetics of the blend is also monitored when exciting MEH-PPV (excitation wavelength 500 nm), as shown in figure 5.4b. The PL decay time is not as significant longer due to the decreased emission contribution of the Alq$_3$ (excitation wavelength is not at the maximum for exciting the Alq$_3$). The increase in the photoluminescence lifetime of the MEH-PPV:Alq$_3$ provides further evidence of Förster energy transfer from the Alq$_3$ to MEH-PPV in the blend films due to the indirect excitation of the Alq$_3$ in the blend which is an evidence of Förster energy transfer.

Time-resolved spectroscopy evidences the dynamics of excitation transfer from intrachain to interchain species in MEH-PPV and from Alq$_3$ to MEH-PPV for varying Alq$_3$ content (figure 5.5). The influence of the intrachain and interchain contribution to the blend emission varying Alq$_3$ (percentages 0 %, 9 %, and 60 %) is investigated by carrying out luminescence measurements with various time windows (i.e. delay intervals) after the excitation.

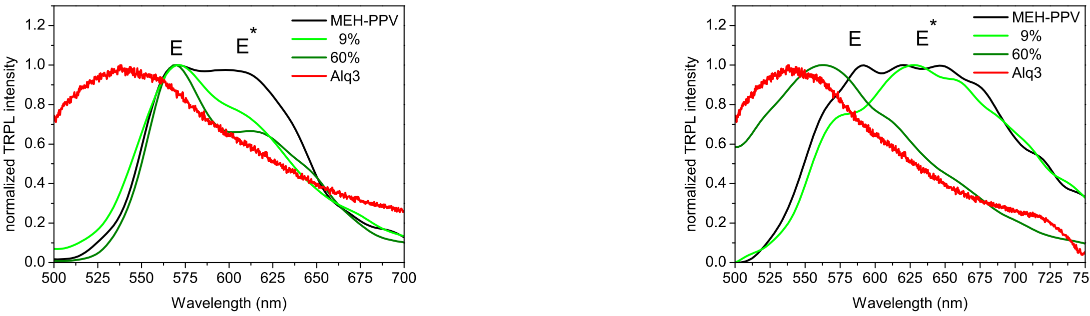

(a) excitation pulse with a delay interval between 0 ps to 960 ps

(b) excitation pulse with a delay interval between 2.5 ns delay to 17 ns

Figure 5.5: Time resolved PL of MEH-PPV alone (green), MEH-PPV:Alq$_3$ = 9% (blue) and MEH-PPV:Alq$_3$ = 60% (light blue). The red curve refers to the Alq$_3$ steady state PL emission as a reference. (E) and (E*) indicate the double peak signal with the vibrational transitions at 580 and 620 nm.

The delay intervals run from the excitation pulse (0 ps delay) to 960 ps ("‘FAST"’ range) and from 2.5 ns delay to 17 ns ("‘MEDIUM"’ range). In the FAST range (figure 5.5a), the fluorescence from the three samples with MEH-PPV exhibit similar characteristics (red curves refer to the CW PL spectrum of Alq_3). The signal is dominated by MEH-PPV emission, with the characteristic double peak signal fluorescence transitions visible at 580 nm and 620 nm. The emission at 620 nm (E^*) loses its intensity with increasing Alq_3 content and is therefore related to the reduced interchain contribution, as pointed out in figure 5.5. As results, a sharper fluorescence signal has been detected for the highest doping concentration of 60 % with a clear indication of the vibrational transitions at 580 and 620 nm. The emission from pure MEH-PPV is less structured and exhibits overlapped interchain and intrachain emission components. The decrease of the interchain emission component has its origin in the polymer chain separation due to the presence of the Alq_3 molecules. The nature of the emitting species in the blend becomes apparent when collecting the signal for longer delay times (more appropriate for the Alq_3 PL kinetics): in the case of pure MEH-PPV (figure 5.5b), the intrachain fluorescence rapidly changes into an unstructured fluorescence centered between 620 nm - 660 nm assigned to MEH-PPV excimers [142]. In the case of the 9 % and 60 % blend, the emission at longer wavelengths (E^*) is reduced and tends to dissappear due to the reduced interchain compontribution. Then, the MEH-PPV excimer formation is nearly completely hindered by the presence of a large amount of Alq_3 (60 %). In this latter case, Alq_3 emits almost independently from MEH-PPV and its fluorescence contribution is seen as overlapped by that of MEH-PPV. The observed Alq_3 fluorescence component lifetime amounts to $\sim$ 6 ns (at 530 nm), i.e., shorter than what is usually measured ($\tau \sim 10$ ns - 12 ns) at room temperature [143].

It has been shown previously that the intrachain component is not influenced by doping MEH-PPV with Alq_3. The chain – chain interaction is reduced when doping MEH-PPV with Alq_3 resulting in a structured fluorescence signal with the characteristic vibrational transitions at 580 and 620 nm and with a lowered emission intensity at 620 nm. The difference in the interchain and intrachain contribution should result also in a difference of the quantum yield which is important for the use of the blend as emissive layer and this information is additionally required for the optical simulation (figure 5.6). For the quantum yield measurements in figure 5.6, the blend layers were excited using either the wavelength at the maximum absorption of the Alq_3 (395 nm) or the wavelength at the maximum absorption of the MEH-PPV (480 nm). A decrease of the PLQY has been observed for an increasing blend concentration in both cases. This effect has been observed in various publications. R. Pizzoferrato *et.al.* (Chemical Physics Letters 414, p.234, 2005) observed a decrease of the PLQY when blending a PAE co-polymers with polystyrene or polymethyl-methacrylate since not all the polymer chains within the host polymer matrix might be effectively dispersed [145] [146]. One explanation has been described as luminescence quenching mechanism due to low miscibility of the blend components and a possible dopant aggregation [144]. A possible aggregation at very high Alq_3 concentration might result in locally stronger MEH-PPV interchain interaction due to the local compression of the MEH-PPV polymer chains as a result of the Alq_3 aggregates, as described by R. Pizzoferrato. The observed effect is even stronger for higher doping concentration of the investigated blend where the PLQY drops from the initial 22 - 24 % (depending on concentration and excitation wavelength) to 18 % for a blend concentration of 60 %. A lowered PLQY will consequently decrease the outcoupled power (increasing non-radiative losses) when applying the blend as emissive layer in OLEDs.

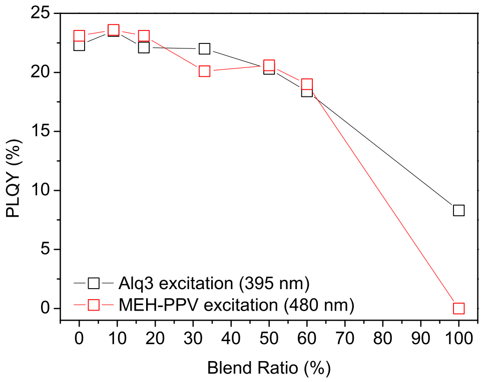

Figure 5.6: Quantum Yield for MEH-PPV:Alq_3 blended films for Alq_3 contents from 5% up to 60%.

AFM measurements show the morphology difference of the blended polymer reflecting also the miscibility of the polymer blend (figure 5.7).

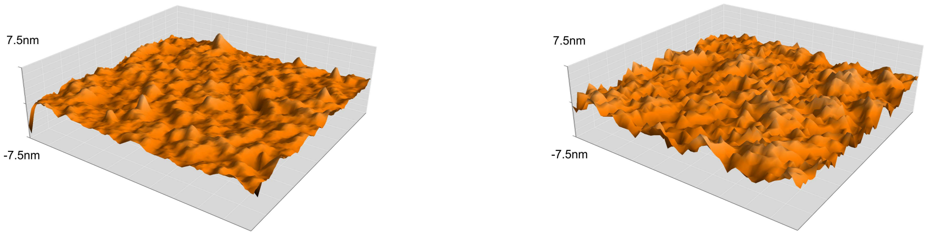

(a) (b)

Figure 5.7: AFM images of MEH-PPV:Alq_3 blended films with 9 % (a) and 60 % (b) concentration

The surface roughness is slightly lower for low concentrations (figure 5.7a) and increases for a high doping concentration of around 60 % (figure 5.7b), which could be an indication of a possible dopant aggregation due to a lower miscibility at high doping concentrations. A low surface roughness should be beneficial for device application due to a better interface between the layers.

To conclude, the modulation observed in the steady state emission spectra of the blends mainly originates from the different contributions to the fluorescence deriving from excited intrachain species of MEH-PPV, i.e., excimers states. Progressively passing from low concentrations to more than 50 % Alq_3 in the blend, it is possible to tune the formation of MEH-PPV excimers (by Alq_3 molecules interposition between polymer segments) and, in the limit of Alq_3 high concentration, to hinder it totally. Whereas the steady state spectrum does not show any evident contribution of Alq_3 fluorescence, by using detection techniques with time resolution and by properly choosing the delay ranges, it is possible to evidence the contribution of the guest polymer. As a result, as the Alq_3 content in the blend increases, the interchain contribution is reduced with respect to the intrachain one, since the presence of Alq_3 molecules augments the distance between the MEH-PPV chains, progressively hindering the excimer formation. TRPL evidences the dynamics of excitation transfer from intrachain to interchain species in MEH-PPV and from Alq_3 to MEH-PPV when the Alq_3 concentration is increased.

5.3 Performance of the blend as emissive layer for OLEDs

The architecture of the blend-based device was ITO/PEDOT:PSS/Polymer Blend/Al, as seen in figure 5.8a. The effect on the charge carrier transport was studied by the investigation of the blended MEH-PPV doped with the electron transport small molecule Alq_3 with different concentrations as emissive layer in OLEDs. MEH-PPV is a hole conductive material with a reported mobility between 1 x 10^{-5} cm^2/Vs and 3 x 10^{-3} cm^2/Vs [144]. The electron mobility is around 1 - 2 order of magnitude lower for MEH-PPV. On the contrary, Alq_3 is a typical electron conductor with good hole-blocking properties due to the low HOMO energy level of around 5.6 eV and with a maximum electron mobility of around 4 x 10^{-5} cm^2 [145]. The energy band-diagram shows the energy level for each layer (figure 5.8b). MEH-PPV is blended with Alq_3 in different concentrations which might influence the electronic nature of the blended MEH-PPV within the OLED structure. Alq_3 blocks also efficiently the holes due to its deep HOMO level. Therefore, the holes are supposedly trapped at the MEH-PPV:Alq$_3$ interface [146]. The majority charges are holes traveling form the anode (ITO) towards the Al cathode. The injection of electrons is very limited due to the energy gap between the workfunction of the Al and the LUMO level of the MEH-PPV. On the other hand, the presence of Alq$_3$ might lead to an improved transport of electrons due to its higher electron mobility. Both effects might lead to a shift of the emitter dipole position and an increased radiative recombination rate.

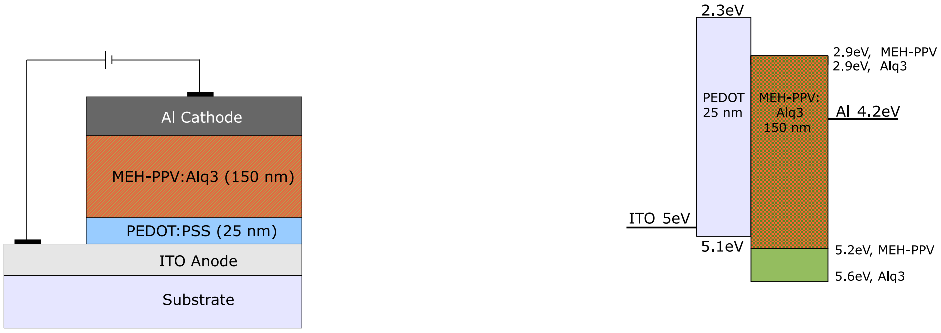

(a) (b)

Figure 5.8: OLED architecture for blended OLEDs (a) and proposed band diagram (b)

The electrical characterization of the fabricated OLEDs shows that the current density decreases when increasing the Alq$_3$ amount (figure 5.9a). On the other hand, an increasing luminance was measured when doping MEH-PPV with the highest luminance reached for a concentration of only 9 % of the Alq$_3$ (figure 5.9b). The Alq$_3$ favors the transport of electrons throughout the blend layer and the blocking of the holes due to the deep HOMO energy level [144][145]. Since small amounts of Alq$_3$ in the blend do not provide efficient hole blocking, the current flow is still high. For higher Alq$_3$ concentrations, the overall current density decreases continuously as the confinement of the holes becomes more efficient due to a denser Alq$_3$ network. As the separation of the polymer chains by Alq$_3$ insertion becomes larger for very high concentration (resulting very likely in a dopand aggregation for very high concentrations), the interchain charge transport is hindered, thus reducing the carrier mobility. Such a behavior is more visible for very high concentrations of Alq$_3$ due to the rapid decrease of the current density. The threshold voltage increases significantly for Alq$_3$ content above 33 % weight concentration from originally 5 V up to 21 V for the highest concentration.

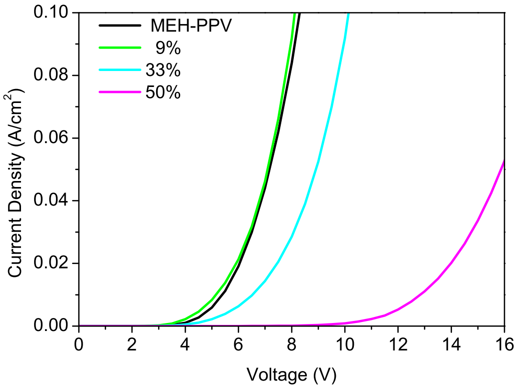

(a) Current density versus applied voltage for MEH-PPV:Alq$_3$ OLEDs

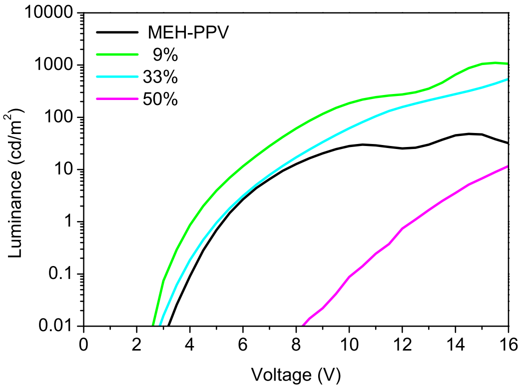

(b) Luminance versus applied voltage characteristic for MEH-PPV:Alq$_3$ OLEDs

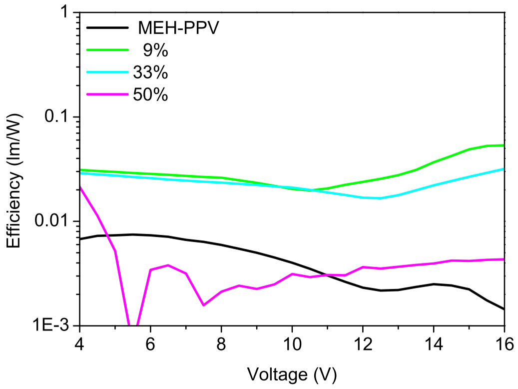

(c) Power efficiency versus applied voltage characteristic for MEH-PPV:Alq$_3$ OLEDs

Figure 5.9: characteristic for OLEDs with MEH-PPV:Alq$_3$ as active emissive layer at different concentrations

The increased presence of electrons and the hole blocking mechanism due to Alq_3 might result in a shift of the emissive dipole towards the center of the polymer and away from the inefficient recombination close to the metal cathode. The power efficiency in lm/W shows a significant improvement compared to the reference MEH-PPV device (figure 5.9c), due to the increase of the luminance by almost keeping the same voltage and current density. The results of the measurements are summarized in table 5.2.

Weight concentration (%)	0	9	17	33	50	60
Current Density$_{max.Lce}$ (A/m^2)	0.43	0.42	0.37	0.38	0.22	0.24
V$_{TH}$ / V$_{max.Lce}$ (V)	5.5/14.5	5/15.5	4,5/16	5/19	12,5/27	21/40
Luminance (cd/m^2)	48	1106	919	709	268	153
max. Efficiency (lm/W)	0.003	0.055	0.05	0.03	0.01	0.005

Table 5.2: Current Density (A/m^2) and efficiency (lm/W) at the maximum brightness (cd/m^2) for MEH-PPV:Alq_3 varying the doping concentration. Best overall performance for the blend OLEDs with a concentration of 9 %

The reference device exhibits a broad EL band centered at around 600 nm, which is assigned to the convolution of the emission of intrachain excitons and interchain species [142][139] (figure 5.10).

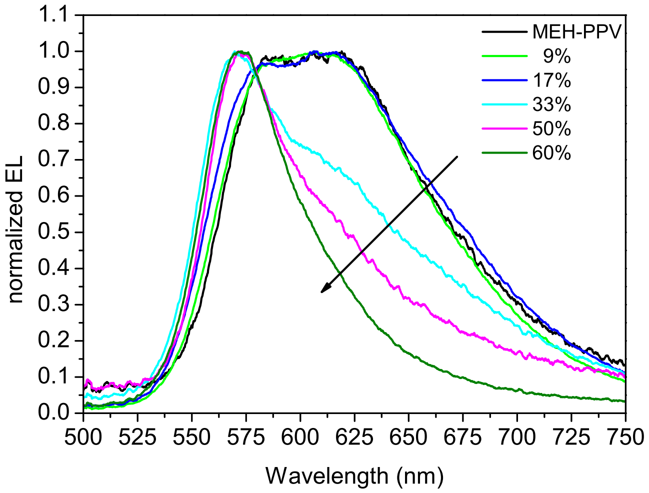

Figure 5.10: Normalized EL spectra for various Alq_3 concentrations in the blend as active layer. The arrow shows the decay of the emission intensity at around 620 nm

Such a broad structure is especially a characteristic for doping concentrations lower than 33 % Alq_3. Above 33 %, as the Alq_3 amount increases, the lower - energy component at around 620 nm of the emission loses intensity and almost disappears, leaving a broadband emission peaked at 580 nm with a shoulder at 620 nm. The FWHM is reduced from 110 nm for the pure MEH-PPV OLED up to 55 nm for the highest doping concentration of 60 % (table 5.3). The EL spectra show no Alq_3 emission contribution for all blend concentrations [147]. A small blueshift of around 10 nm at the FWHM has been observed for the EL spectrum of the blended layers. Several publications reported such an effect for blended polymers [148][149]. To clarify, the blend layers have been processed under the same conditions and using the same solvents. It is therefore unlikely that the EL shift is related to the process conditions. The changes in the EL and PL spectrum upon Alq_3 doping are often understood in terms of higher sensitivity of the EL to the chain separation due to the transport of the electrical excited charge carriers, which happens mainly across the polymer chains [150][151]. However, the lowered emission intensity at 620 nm as result of the increased Alq_3 concentration is not as significant when recording the CWPL (figure 5.3b) leading to the assumption that the position of the emissive dipole in the device accounts for the substantial change of the EL spectrum.

	MEH-PPV	9 %	17 %	33 %	50 %	60 %
FWHM (nm)	110	110	122	90	67	55
max. EL (nm)	619	606	607	570	571	573

Table 5.3: FWHM and the wavelength at the maximum EL emission peak for blended MEH-PPV OLEDs

The device structure, the CWPL spectrum, the measured EL spectrum, the PLQY and the optical constants for each layer are required for the simulation of the EL spectrum and the calculation of the emissive dipole position. The PL and EL spectrum are examined experimental previously in figure 5.3b and 5.10. The measured transmittance and reflectance required for the calculation of the optical constants are shown in figure A.14 and A.15. The calculated refractive index n and the extinction coefficient k for each blend concentration are measured and shown in figure A.4 - A.10. A good agreement between the experimental results (figure 5.10) and simulated outcoupled emission spectrum for the pure MEH-PPV and the blend with a concentration of 9 % and 60 % has been found, as shown in figure 5.11a. The shape of the spectra for the given blend concentrations seems to be similar when comparing the experiment and simulation. The dipole position has been calculated for the previously simulated blend concentrations (MEH-PPV, 9 %

and 60 %) (figure 5.11b). The passive optics simulation clearly shows the shift of the emissive dipole position without consideration of the electronic properties such as charge carrier injection or charge carrier mobilities. For the undoped MEH-PPV, an emitter dipole position with a distance of only 5 nm from the metallic cathode - polymer blend interface has been calculated taking into account an emissive layer thickness of 150 nm. The calculated position of the emitter dipole was found to be around 26 nm away from the metallic cathode - polymer blend interface for a concentration of 9 %. More significant is the shift of the emitter dipole for the highest concentration. The emitter dipole position is 125 nm away from the metallic cathode - polymer blend interface. Again, the simulation is based on passive optics calculation without consideration of charge transport and recombination mechanism. As a result, the simulation clearly shows that the polymer chain separation and its influence on the PL spectrum and PLQY does not influence significantly the EL spectrum. In fact, the significant decrease at 620 nm is mainly the result of the shifted emitter dipole position towards the anode side of the active layer.

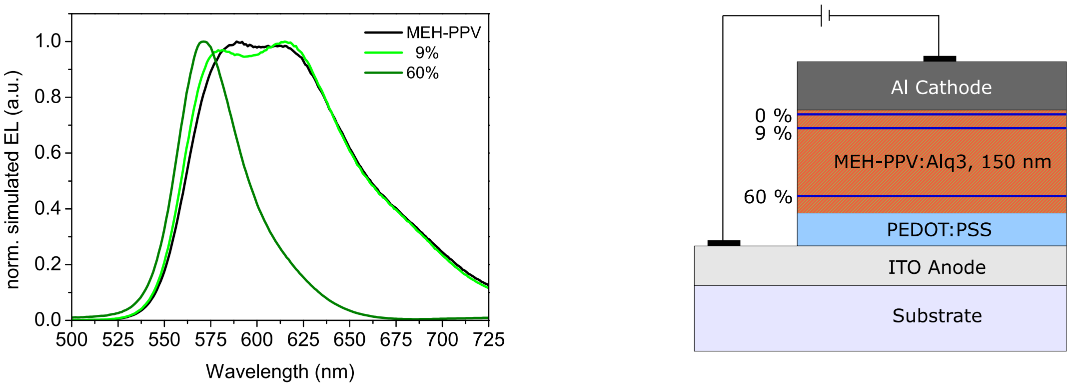

(a)

(b)

Figure 5.11: simulated EL spectrum for various blend concentration (a), calculated emitter dipole position (b)

Figure 5.12 shows a deeper analysis of the influence of the emitter dipole position and the changed intrinsic properties on the emission spectrum and their relationship to each other. The electroluminescence spectrum has been simulated in figure 5.12a using the reference blend OLED (concentration 9%, black) with n, k, PL and PLQY when doping MEH-PPV with 60 % of Alq$_3$ and keeping the emitter dipole position as calculated for the 9 % blend concentration (red) and vice - versa (green). A change of the intrinsic properties of the polymer due to a high doping concentration (intrinsic properties) lowers the second peak of the emission spectrum (red). The second peak at 620 nm is completely suppressed when shifting the emitter dipole very close to the PEDOT:PSS - polymer interface (as for a doping concentration of 60 %) and keeping the intrinsic properties (blend concentration 9 %). This simulation proves again that the difference of the PL and EL spectrum is rather related to the strong shift of the emitter dipole than to the change of the intrinsic properties.

The emitter dipole position and the intrinsic properties will consequently influence the characteristic of the outcoupled power fraction. Figure 5.12b illustrates the simulation results. The outcoupling characteristic for the reference blend device (9 %) and the device with the influenced intrinsic properties are very similar, however, the average outcoupled fraction is lowered from 3.3 % to 2.61 %. A different characteristic of the outcoupled fraction over the wavelength has been simulated when shifting the emitter dipole towards the PEDOT:PSS - polymer interface (green curve). The average outcoupled power is also lowered to 2.7 % in this particular case. This drastic change of the outcoupling characteristic when shifting the emitter dipole is therefore mainly responsible for the change of the EL spectrum since the outcoupling around 570 nm is enhanced while the outcoupling at 620 nm is almost completely suppressed.

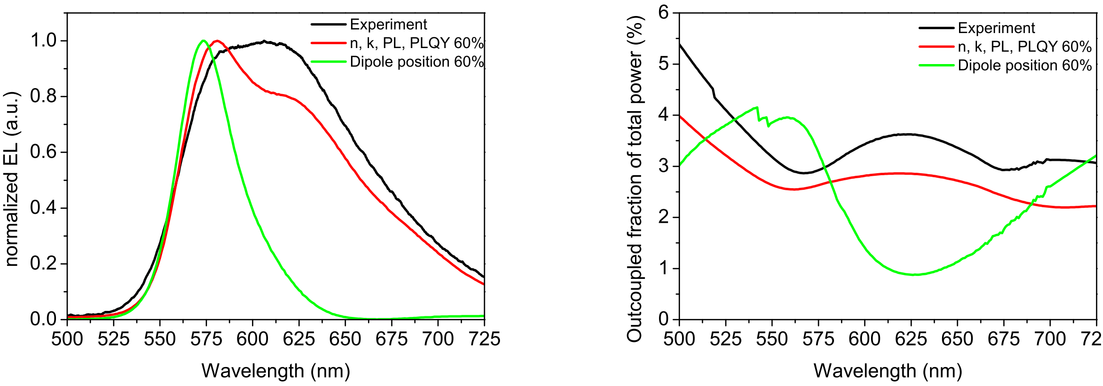

(a) (b)

Figure 5.12: simulated EL spectrum (a) and outcoupled fraction of total power (b) for a doping concentration of 9 & varying either the dipole position or the intrinsic properties

An optimization of the optical characteristics of such a device configuration should consider a low doping concentration since the intrinsic material properties are maintained and the shift of the emitter dipole does not influence the EL spectrum and might lower therefore the outcoupling efficiency. The simulation results are in good agreement with the experimental results when using a low doped MEH-PPV blend as emissive layer in OLEDs (table 5.2). The outcoupled fraction of the total emitted power has been simulated for the pure MEH-PPV device, the best blend device (9 %) and the blend with the highest doping concentration (60 %) (figure 5.13a). The simulation shows a significant increase of the outcoupled power fraction for the low blend concentration (up to 3.3 %), while the outcoupled fraction is around 2 % lower for the reference MEH-PPV and the high concentration blended OLED (figure 5.13a). The outcoupled fraction of the total power depends on the intrinsic optical properties of the blend influenced by the doping concentration (n, k, PL, PLQY) and moreover the dipole position as previously proved. The average outcoupled power fraction has been also evaluated for the OLEDs as a function of the emitter dipole position (figure 5.13b), assuming that the electrical properties will be maintained.

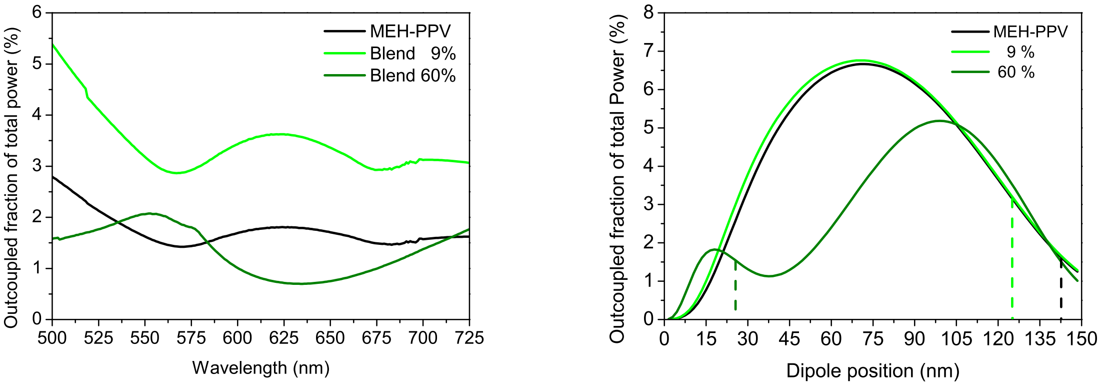

(a) (b)

Figure 5.13: outcoupled fraction of total emitted power over the emission wavelength of the blend devices (a), average outcoupled fraction for blended OLEDs as a function of the relative dipole position (b) with an indication of the calculated emitter dipole position for these particular device configurations

The dependence of the outcoupled power on the emitter dipole position is clearly visible. The MEH-PPV and blend 9 % OLED exhibit a very similar characteristic for the outcoupled power fraction since the low concentration of Alq_3 does not influence significantly the intrinsic optical properties of the MEH-PPV, as seen when evaluating the PLQY (figure 5.6), the PL (figure 5.3) and EL (figure 5.10) spectrum and the optical constants (figure A.6). The enhancement of the outcoupled power fraction is therefore mostly related to the shift of the emitter dipole position, as shown in figure 5.13b for a low doping concentrations. When doping MEH-PPV with a high amount of Alq_3, the intrinsic material properties, such as n, k, PLQY and the photoluminescence spectrum are strongly influenced. As a result, the characteristic of the outcoupled power fraction as a function of the emitter dipole position has been changed (figure 5.13b).

An optical optimization would lead to a significant increase of the outcoupled power when shifting the emitter dipole towards the center of the blend layer, as illustrated in figure 5.13b (assuming that the electrical performance of the OLED is not affected). An optimum distance of the emitter dipole of 79.5 nm from the metallic cathode has been calculated reaching a maximum outcoupling power fraction of 6.76 % (polymer thickness 150 nm). Changing the thickness of the emissive layer also influences the distance of the emitter dipole to the electrodes keeping the relative position within the polymer. An optimized layer thickness leads to higher outcoupling power intensities, as shown in figure 5.14., since the distance of the emitter dipole to the metallic cathode is larger. An optimum for the blend thickness has been found at 380 nm reaching an outcoupled power fraction of 6.66 %. Again, the optimization method considers only the optical parameters and does not take into account the electronic properties of this device structure.

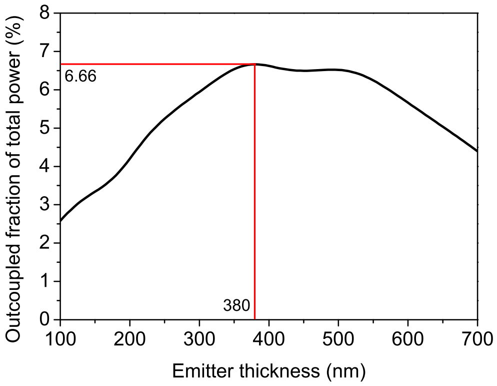

Figure 5.14: Simulated outcoupled power fraction and its maximum at 380 nm as a function of the thickness of the blend layer with a concentration of 9 % Alq_3.

The best blend OLED device can be compared with the multilayer structure, which has been investigated in chapter 4.3.2 (figure 4.19). Both concepts presented in this thesis show a strong improvement compared to the reference OLED. It has been proved that the blending of the host polymer can even lead to higher efficiencies than multilayer OLEDs when optimizing the doping concentration. The best blend device shows higher luminance values at much lower current densities compared to the multilayer OLEDs. The charge carrier transport in such a blend structure is not hindered due to the presence of an interfacial protection layer. As an advantage, the multilayer device shows a lower threshold voltage which might be beneficial for some applications. These both concepts have to be understood as model due to the use of commercially available but less efficient materials. The choice of solution processed multilayer or blend device concept depends on the required specifications. The measured characteristic of the devices are summarized for comparison again in table 5.4.

Material	MEH-PPV:Alq_3 (9 %)	MEH-PPV + ALD + Alq_3
Current Density$_{max.Lce}$ (A/m^2)	0.42	0.67
V_{TH} / $V_{max.Lce}$ (V)	5/15.5	3.5/ 12
max. Luminance (cd/m^2)	1106	880
max. Efficiency (lm/W)	0.055	0.035

Table 5.4: Comparison of MEH-PPV based OLEDs, 1.) MEH-PPV was blended with 9 % Alq_3 and 2.) multilayer device with Al_2O_3 and Alq_3

The significant increase of the MEH-PPV OLED efficiency via doping with Alq_3 *is the result of an improved charge carrier transport. An increase of the electron transport can be expected due to the presence of the electron transport and hole blocking material* Alq_3*. The increased doping concentration leads to a shift of the emissive dipole position towards the center which prevents the inefficient and non-radiative recombination close to the metallic electrode. Additionally, the outcoupled fraction of total power has been increased due to the shift of the emitter dipole. As a result, a significant enhancement of the OLED luminance for a low doping concentration at similar voltages and similar current densities has been measured. A significant decrease of the emission intensity at around 620 nm for increasing* Alq_3 *concentration has been recorded when examining the EL spectrum. It has been reported that the electroluminescence signal responds more sensitively to the interchain contribution due to the charge carrier transport across the polymer chain. However, the difference between the PL and EL signal is very significant and the passive optics simulation disproved this conclusion. The decreased emission intensity at around 620 nm can be related to the difference in the optical path due to the shift of the emitter dipole resulting in an increased outcoupling efficiency. The multilayer concept from chapter 4 has been compared with the blend OLED, showing slightly lower performances when using multilayer structures.*

5.4 Conclusion

Blending of polymers is an efficient solution for increasing the efficiency of solution processed OLED devices. Conjugated polymers are usually hole-conductive and the electron mobility is very low. The energy transfer from the guest small molecule Alq_3 to the host polymer MEH-PPV has been elaborated in this chapter. Alq_3 has been added in different concentrations to MEH-PPV and the optical and electrical properties have been evaluated. It has been shown that no contribution of the Alq_3 has been measured for the steady state photoluminescence measurement. TRPL evidences the dynamics of excitation transfer from the intrachain to interchain species in MEH-PPV and from Alq_3 to MEH-PPV when the Alq_3 concentration is increased. As the content of the Alq_3 in the blend increases, the interchain contribution to PL is reduced with respect to the intrachain contribution, since the presence of the Alq_3 molecules augments the distance between the MEH-PPV chains, progressively hindering the excimer formation. The OLED efficiency has been increased significantly taken into account that no electron-injection has been inserted between the blend and the Al-cathode. The increase of the luminance when blending MEH-PPV at similar voltages and current densities can be therefore attributed to the improved electron transport and the resulting shift emissive dipole away from the inefficient recombination position close to the metallic cathode. However, not only the electronic properties have to be considered in such a blend device. Blending the host polymer also changes the optical characteristic in terms of transmittance and reflection. The calculated absorption coefficient k and refractive index n show strong wavelength dependence and it has been proved that the doping concentration influences also the outcoupled emission spectrum. A drastic decrease of the emission intensity at 620 nm has been measured for the electroluminescence spectrum. A higher response sensitivity of the EL signal on the interchain contribution has been considered but this explanation is not sufficient for such a decrease. The simulation proves that the difference of the EL and PL spectrum can explained by the difference of optical path length due to the shift of the emissive dipole away from the metallic electrode.Additionally, the outcoupled fraction of the emitted total power by the emitter dipole is around 2-times as high as for the only MEH-PPV device when doping with 9 %. It is therefore mandatory to consider two effects when blending a polymer: optimizing the concentration in respect to the desired electronic properties and controlling the influence of the guest small-molecule on the optical characteristic within the OLED stack.

Chapter 6

Summary and Outlook

The introduction of OLEDs for applications such as advertisement or signages is limited due to the high price of the OLEDs resulting from the use of ITO and the complex and cost intense processing for achieving high efficient devices. A significant motivation for the applicability of OLEDs in different niche markets would be a low cost device using commercially available materials and without ITO and not necessarily achieving high efficiencies and long lifetimes. The present thesis analyzes different methods for the efficient use and improvement of commercially available materials for their application in organic light emitting diodes. Furthermore, these materials have been used also in solution processed multilayer OLEDs using an ALD deposited aluminum oxide film within the stack. The focus of the thesis is to find alternative processes and material combinations without being focused, in this initial state, on record efficiencies of OLEDs. Nevertheless, similar or even higher efficiencies have been reached for the proposed techniques which already show the promising potential of the ideas herein presented even though further work is required for a deeper analysis.

Three main topics have been covered throughout the thesis. The chapter 3 deals with the replacement of ITO using ultra-thin metal films. ITO is one of the cost drivers of OLEDs and it has also a few fundamental disadvantages due to its coupling ability, processing and brittleness when using flexible substrates. The field of applications of the ALD has been further exploited in chapter 4. Only a few nanometers thin aluminumoxide layer has been deposited onto the active emissive polymer to prevent intermixing when spin-coating an electron transport material on top. However, intermixing is a desired process when using blends where a host material (MEH-PPV) is controlled doped with an electron transport material (Alq_3). The energy transfer and its effect on the OLED efficiency have been investigated in chapter 5.

It is well know that OLEDs have a poor outcoupling efficiency, which is mostly limited by the relatively thick conductive and transparent ITO anode. The refractive index of this oxide is different from the polymer refractive index and influences therefore the intensity of the outcoupling power. (see equation $\eta_{out} = (1 / 2n^2)$). Replacing the commonly used ITO as anode material is one of the main issues in research nowadays. Promising candidates for the replacement of ITO as electrode materials are ultra-thin metal films (UTMF), such as Ni and a double layer CuNi layer as presented in chapter 3. Ultra-thin Ni layers can be easily and controlled deposited and do not require any further treatments. The sheet resistance and a surface roughness is a bit higher for the Ni film compare to the ITO. The workfunction matches the HOMO level of the on top spin-coated PEDOT layer, so that an efficient injection of holes can be guaranteed. The optical characterization shows that the transmittance is around three times lower. However, an improved OLED efficiency and a higher brightness can be obtained when applying such an ultrathin Ni film as anode in OLEDs. The intensity of the outcoupled power is not only dependent on the transmittance of the layer but also on the thickness due to the possible waveguiding modes. It has been proved, using a commercial simulation software, that the waveguiding is lowered for the Ni-film due to its low thickness, which results in an improved outcoupling. Ni has been implemented in OLEDs with different emissive active polymers (SY and PFO). The OLED with Ni and PFO show even a higher brightness than the ITO based OLED but the efficiency in lm/W is lower due to the poorer electronic properties of the Ni film and due to the poor electron injection.

Therefore, a further increase of the performance of Ni-based OLEDs requires a further improvement of the material properties itself and an improved electron injection using an interfacial layer between the polymer and the metal cathode. For instance, pure Cu shows better optical and electrical properties than Ni, but it is not very compatible as pure anode material due to its unstable behavior within the OLED structure. It was found, however, that these excellent properties can be maintained capping the Cu layer with Ni forming a CuNi interface which is additionally resistant against oxidization. The transparency is higher than the pure Ni and reaches 64 % for the visible light. Even the roughness (0.55 nm) and the sheet-resistance (15.3 Ω/sq) is very similar to ITO. When applied into OLEDs with SY as emissive polymer and with an efficient cathode, the devices show high efficiency, almost as good as ITO-based devices with good operation stability over time. A maximum brightness of more than 17000 cd/m^2 with an efficiency of 1.9 lm/W at 8 V was measured. This shows the excellent performance of such a CuNi double layer. The observed temperature stability together with the optical transmittance and electrical resistivity performances confirm that multilayer ultra-thin metal films are serious competitors to transparent conductive oxides, such as ITO, for those applications where transparent electrodes are required.

Avoiding complex processes for the electrode deposition as well as replacing ITO using cheap materials is very crucial for the successful commercialization of OLED devices. On the other hand, complex multilayer structures are widely used for obtaining high performance OLED devices based on vacuum deposited small molecules. In that case different layers can be exactly deposited on top of each other for a perfect alignment of the energy-level and optimal balance between electron and holes. Such a technology requires expensive and complex vacuum processes. However, multilayer structures are hard to achieve for polymer-based devices due to the intermixing of solution based organic layers. A novel approach for solution processed multilayer OLED structure has been demonstrated in chapter 4, where an ultra-thin ALD deposited aluminum oxide Al_2O_3 has been used for the protection of the underlying layer. An atomic layer deposition process has been chosen because it is a well controllable technique which is already widely used for the deposition of the encapsulation layer for organic devices due to the high density of the oxide. Additionally, companies like BENEQ and 3D-Micromac have been working on the implementation of the ALD technology into a R2R production facility. The combination of the possible implementation of a high quality dense oxide films for controlling the charge carrier balance in solution processed multilayer OLEDs is one of the main motivations for this research.

The oxide thickness and the deposition condition have been optimized for the used OLED configuration and, finally, the Al_2O_3 layer was applied into the multilayer OLED structure. A 2 nm thin aluminum oxide film show sufficient protection and allows still charge carrier transport as proved when applied in an OLED. Then, the electron transport small molecule tris-(8-hydroxyquinoline) aluminum (Alq_3) was spin-coated on top, between the protected emissive polymer and the cathode. It has been demonstrated that the PL and the EL spectrum of the OLED did not change or shift significant even though an additional emissive material has been introduced. The appearing small shoulder in the EL spectrum is the result of the additional layer with its optical properties as demonstrated in the simulation. Furthermore, the presence of the Alq_3 leads to the desired strong enhancement of the OLED efficiency. The brightness of the low efficient reference OLED was increased from around 200 cd/m^2 up to 4700 cd/m^2. Not only has the electrical characteristic of the OLED been improved by an improved balance of electron and holes, but also the optical characteristic. The introduced Alq_3 and Al_2O_3 leads to an improved electron transport and furthermore, the holes are blocked due to the deep energy level of the oxide so that the emitter dipole is shifted from being close at the metallic cathode towards the center of the emissive polymer. The simulation proves that the outcoupling fraction of the emitted power is poor for an emitting dipole located close to the metallic cathode. As soon as electron transport layer is present, the dipole position is moved away from the cathode resulting in a strong increase of the outcoupling fraction of the total emitted power; from 2 % for the standard device to 9 % for the multilayer OLED. The concept has been proved for a second polymer and an OLED efficiency enhancement in the same order has been calculated for the multilayer OLED. It has been therefore successfully demonstrated that multilayer structures for solution processed OLEDs can be achieved using an ultra-thin aluminum oxide as protection layer. Finally, it can be concluded that the ALD technique shows more potential than just the encapsulation of the polymer based devices. It offers a broad pool of possible applications, each of which requires further in-depth investigation.

An attractive alternative to multilayer structure is the use of a blended polymer as single layer. The active emissive polymers are usually hole-conductive with poor electron conductivity. However, the electron conduction of this material can be increased by doping with an electron-conductive material. A potential candidate is Alq_3, which is widely used for the electron transport and as emissive layer for vacuum deposited small molecule OLEDs. Alq_3 can be dissolved in commonly used solvents and can be, therefore, blended with the MEH-PPV solution. Doping the host material has been widely investigated; but in most of the cases, the used guest material is non-emissive in order to keep the emission purity. This approach limits the number of materials which can be used.

In the presented case in chapter 5, both materials used in the presented host-guest matrix are commercially available emissive materials. No further complex synthesis or additional chemical modification was used to change the electrical properties of the host and guest material. It has been shown that the photoluminescence spectrum of the host material (e.g. MEH-PPV) was maintained even for high Alq_3 doping content. When applying the blend as emissive layer into the OLED structure, a more than 20-fold increase of the brightness with a maximum of around 1100 cd/m^2 for a doping concentration of 9 % has been measured. The improvement is due to the improved electron transport leading to a more efficient radiative recombination since the emissive dipole is shift more to the center of the polymer. Not only the intrinsic electronic properties have been changed via doping, but also the intrinsic optical characteristics of the doped material are different depending on the doping concentration. The measurements of the optical constants show the influence of the doping concentration on the refractive index n and the absorption coefficient k. By applying this knowledge into the simulation a change of the dipole position can be calculated which influences also the optical path of the emitted light. The emitter dipole is clearly shifted towards the center of the emissive layer when doping MEH-PPV with Alq_3. The inefficient recombination close to the metallic electrode is therefore lowered. The OLED enhancement was therefore the result of the increased electron conduction leading to an improved balance of electrons and holes and, furthermore, to the increase of the improved outcoupling due to the shift of the dipole position and the change of the intrinsic optical properties of the blend. This technology extends, therefore, the range of material combinations as emissive layer for achieving efficient devices which are easy to fabricate. The measured efficiency is even higher than for the multilayer device with identical materials presented in chapter 4. It shows also that both concepts are improving the device efficiency, with lower threshold voltage for the multilayer OLED but higher efficiency for the blend device. Therefore both concepts have been proved to be attractive depending on the required specification.

Alternative anode materials have been successfully applied into the OLED structure. The proposed Cu-Ni bilayer offers a temperature stable, transparent and highly conductive anode material for optoelectronic applications. Well-known polymers have been used in order to successfully demonstrate the concept. Further, optimization of the layer thicknesses and the use high efficient polymers will increase significant the performance of such OLEDs. Ultrathin metal films increase the intensity outcoupled power due to its thickness resulting in a lower light coupling. Large area device have not been investigated in the presented thesis but future work should be to exploit the potential of double layer metal films for various big area applications such as OPV. Furthermore, the potential of the ALD technique has been explored for the fabrication of multilayer solution-processed OLEDs. Exploiting the technological possibilities of the ALD as process tool for the deposition of an interfacial oxide protection layer results in a multilayer OLED with a solution processed active layer and electron transport layer. The emissive layer has been protected successfully the underlying emissive layer leading additionally to a shift of the emitter dipole. The simulation corroborates the significant increase of the outcoupled power. Therefore, multilayer solution processed OLEDs can be fabricated without crosslinking or a complex chemical modification. The additional layer and variation of layer thickness can additionally enhance the OLED performance due to a recombination close to the emissive polymer center. However, sometimes an efficient OLED device with fewer layers is required. Fewer layers might play a role for low cost devices with reasonable performances. This can be usually done by doping the emissive layer by a hole- or electron transport material. The energy transfer in blended polymers has been investigated and a successful integration into an OLED device was demonstrated. Again, the doping of a hole conductive polymer leads usually to a shift of the emitter dipole position and improves the overall device efficiency. To conclude, the performance of an OLED device is strongly related to the intrinsic properties of the polymer material, the energy alignment between the interfaces of the layers and moreover the electrical and optical properties of the electrode materials. Thus, solution processed OLEDs with a reasonable efficiency and brightness can be achieved using commercially available low cost materials.

List of Figures

List of Tables

Appendix A

Figures

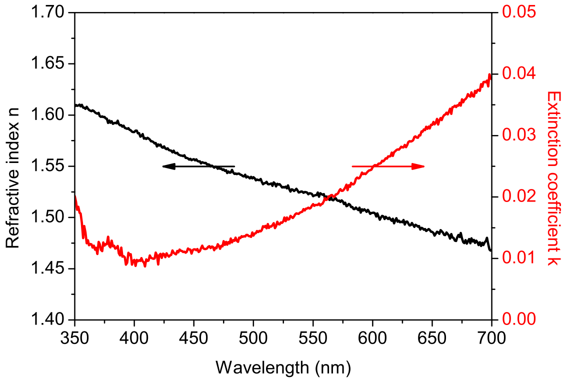

Figure A.1: refractive index n and extinction coefficient k for PEDOT:PSS

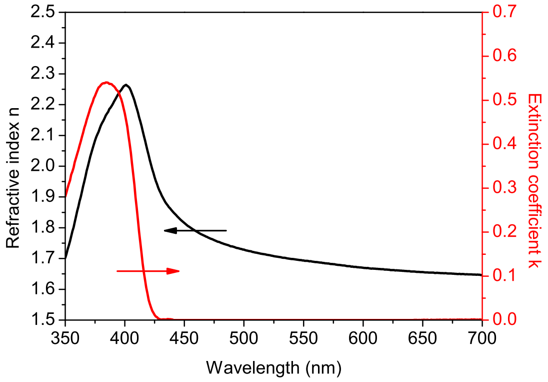

Figure A.2: PFO, refractive index n and extinction coefficient k for PFO

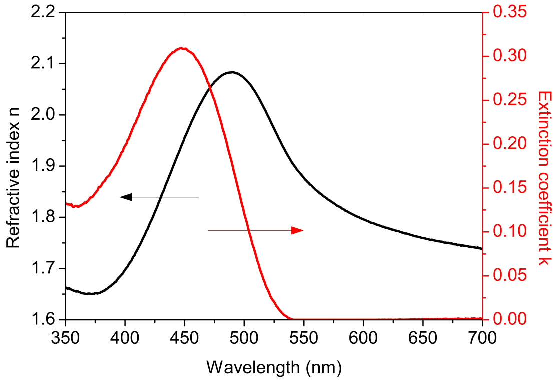

Figure A.3: refractive index n and extinction coefficient k for Superyellow

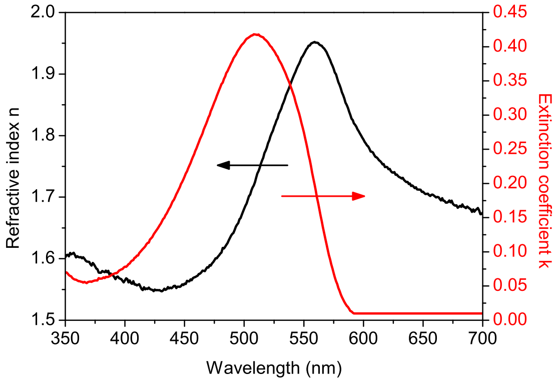

Figure A.4: refractive index n and extinction coefficient k for MEH-PPV

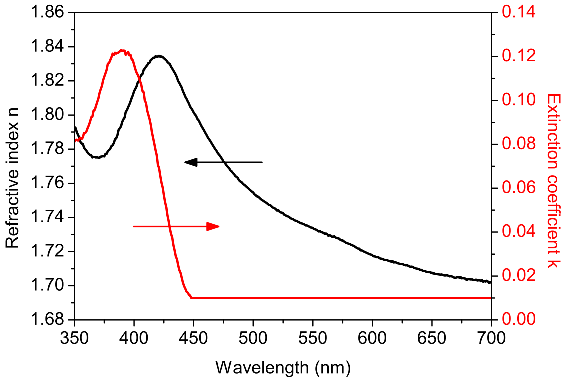

Figure A.5: refractive index n and extinction coefficient k for Alq3

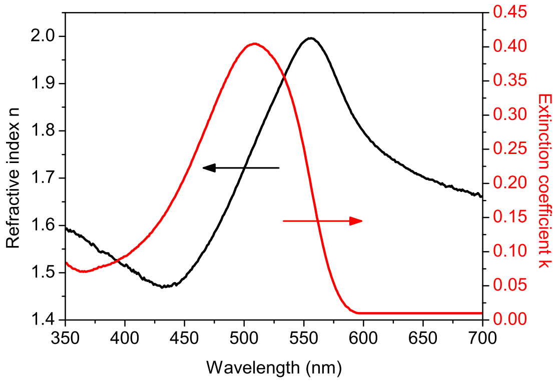

Figure A.6: refractive index n and extinction coefficient k for MEH-PPV:Alq3 with 9% doping concentration

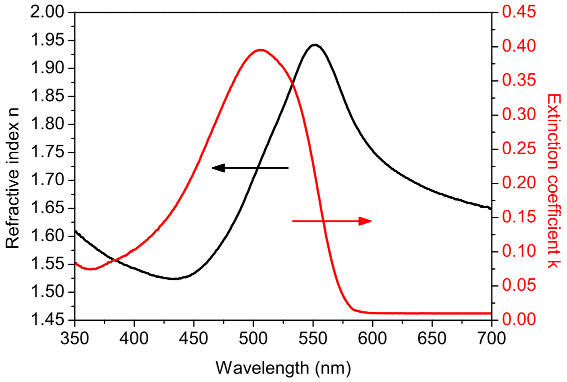

Figure A.7: refractive index n and extinction coefficient k for MEH-PPV:Alq3 with 17% doping concentration

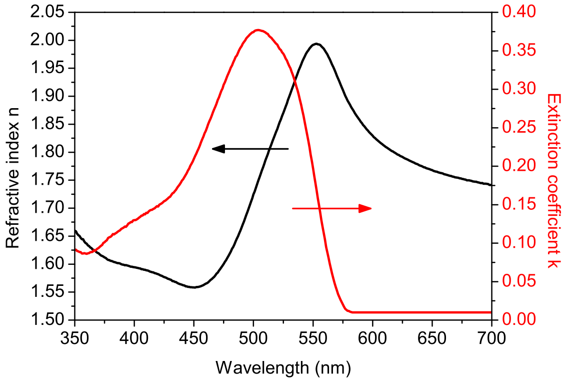

Figure A.8: refractive index n and extinction coefficient k for MEH-PPV:Alq3 with 33% doping concentration

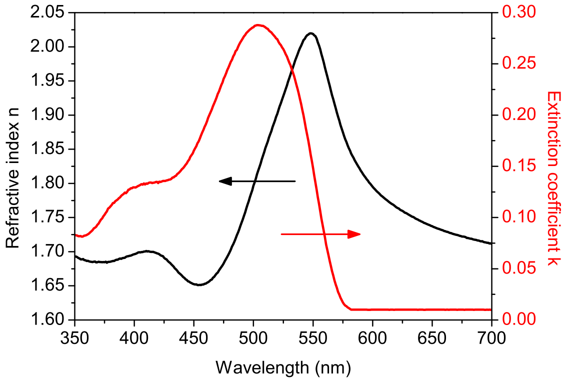

Figure A.9: refractive index n and extinction coefficient k for MEH-PPV:Alq3 with 50% doping concentration

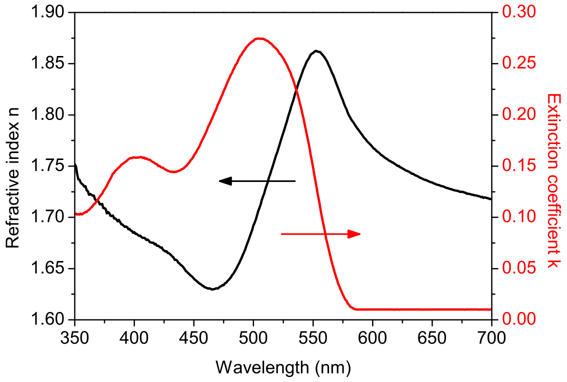

Figure A.10: refractive index n and extinction coefficient k for MEH-PPV:Alq3 with 60% doping concentration

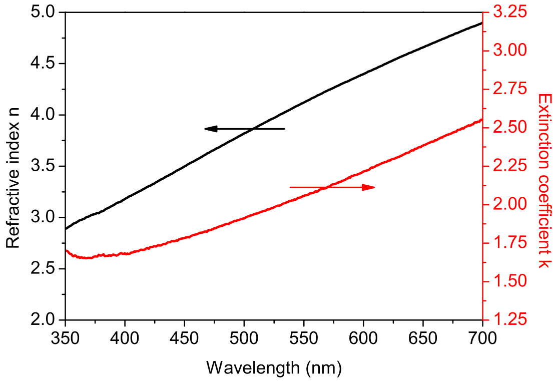

Figure A.11: refractive index n and extinction coefficient k for Ni

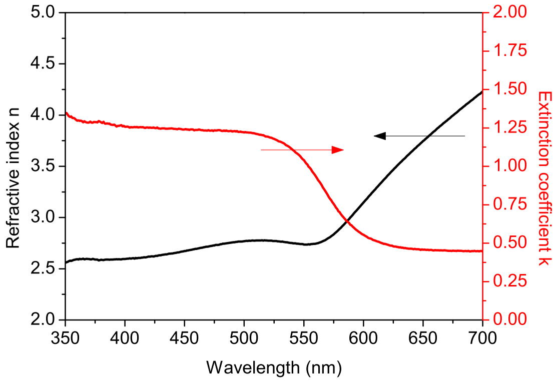

Figure A.12: refractive index n and extinction coefficient k for Cu

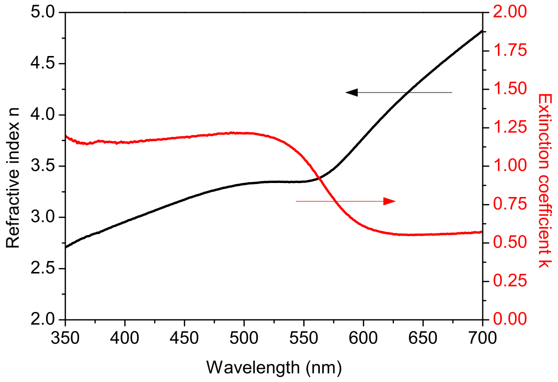

Figure A.13: refractive index n and extinction coefficient k for CuNi (7 nm + 1 nm)

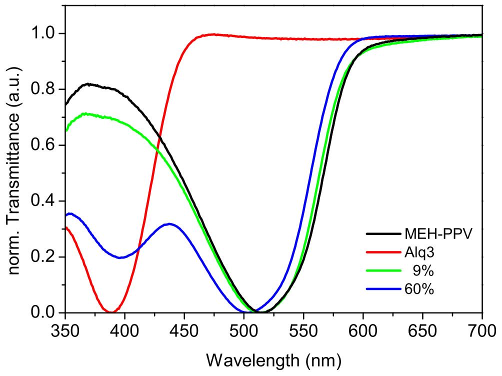

Figure A.14: Transmission spectrum for polymer blends

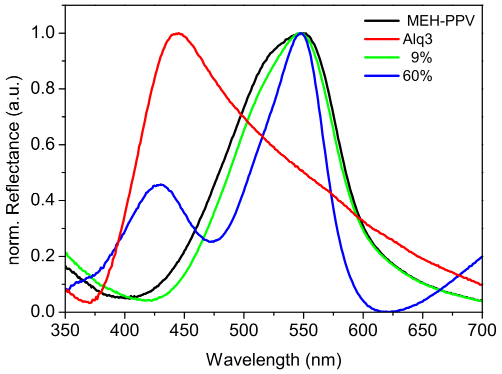

Figure A.15: Reflection spectrum for polymer blends

Appendix B

Tables

	f_1 (%)	t_1 (ns)	f_2 (%)	t_2 (ns)	f_3 (%)	t_3 (ns)
9 %	4.6	0.09	73	0.14	22	0.45
60 %	40	0.25	23	1.3	37	6.3

Table B.1: PL decay for blended MEH-PPV at different concentrations: excitation wavelength 400 nm, recorded emission wavelength 530 nm

	f_1 (%)	t_1 (ns)	f_2 (%)	t_2 (ns)	f_3 (%)	t_3 (ns)
0 %	63.6	0.15	30.9	0.42	5.5	1.1
9 %	71.8	0.14	25.9	0.4	2.3	1.5
60 %	37.0	0.16	50.1	0.47	2.9	1.98

Table B.2: PL decay for blended MEH-PPV at different concentrations: excitation wavelength 400 nm, recorded emission wavelength 570 nm

	f_1 (%)	t_1 (ns)	f_2 (%)	t_2 (ns)	f_3 (%)	t_3 (ns)
9 %	38.2	0.03	41.3	0.20	20.5	0.53
60 %	30.5	0.04	51.6	0.31	17.9	0.74

Table B.3: PL decay for blended MEH-PPV at different concentrations: excitation wavelength 500 nm, recorded emission wavelength 530 nm

	f_1 (%)	t_1 (ns)	f_2 (%)	t_2 (ns)	f_3 (%)	t_3 (ns)
0 %	42.1	0.07	53.0	0.38	4.9	1.2
9 %	52.4	0.11	44.6	0.38	3.0	1.3
60 %	23.8	0.09	67.9	0.39	8.3	1.13

Table B.4: PL decay for blended MEH-PPV at different concentrations: excitation wavelength 500 nm, recorded emission wavelength 570 nm

Appendix C

Transfer Matrix Formalism

The transfer matrix formalism has been used in the simulation software Setfos 3.3 (Fluxim) for the calculation of the passive optics properties of thin multilayer structures [155]. The reflectivity R, the absorption A and the transmission T of a multilayer structure can been calculated by considering the complex refractive index and the thickness of each layer. Assuming a multilayer system with N layers, each of those with a thickness d$_i$ and complex refractive index n$_i$.

A transfer matrix for each interface and layers can be calculated and as a result, the complete transfer matrix can be obtained by simply multiplying each single transfer matrix [156]. The optical stack can be described as follow:

$$\begin{aligned} n(x) = {} & n_0, x < x_0, \\ & n_1, x_0 < x < x_1, \\ & . \\ & . \\ & . \\ & n_N, x_{N-1} < x_i, \end{aligned} \tag{C.1}$$

First, we consider an individual transfer matrix through one interface between the layer i and the layer j. The amplitudes of the forward (indicated as F) and of the backward (indicated as B) propagating wave in a given direction can be expressed in the following way [157][158]:

$$\begin{bmatrix} E_F(x_i^+) \\ E_B(x_i^-) \end{bmatrix} = \mathbf{T}_{0N} \begin{bmatrix} E_F(x_N - 1^+) \\ E_B(x_N - 1^+) \end{bmatrix} = \begin{bmatrix} t_i j & r_{ji} \\ r_i j & t_{ji} \end{bmatrix} \begin{bmatrix} E_F(x_i^-) \\ E_B(x_i^+) \end{bmatrix} \tag{C.2}$$

The Fresnel coefficients for the TE-polarization would be [156][157]:

$$r_{ij} = \frac{n_i cos\theta_i - n_j cos\theta_j}{n_i cos\theta_i + n_j cos\theta_j} \tag{C.3}$$

$$t_{ij} = 1 + r_{ij} \tag{C.4}$$

and for the TM-polarization [156][157]:

$$r_{ij} = \frac{n_j cos\theta_i - n_i cos\theta_j}{n_j cos\theta_i + n_i cos\theta_j} \tag{C.5}$$

$$t_{ij} = \frac{n_i}{n_j} + r_{ij} \tag{C.6}$$

the symmetry relation of the Fresnel coefficients simplifies the equation C2:

$$r_{ij} = -r_{ji} \tag{C.7}$$

$$t_{ij} t_{ji} - r_{ij} r_{ji} = 1 \tag{C.8}$$

so that we obtain:

$$\begin{bmatrix} E_F(x_i^-) \\ E_B(x_i^-) \end{bmatrix} = \frac{1}{t_{ij}} \begin{bmatrix} 1 & r_{ij} \\ r_{ij} & 1 \end{bmatrix} \begin{bmatrix} E_F(x_i^+) \\ E_B(x_i^+) \end{bmatrix} \tag{C.9}$$

with the transfer matrix T$_{ij}$ for the wave propagation through the interface between the layer i and j:

$$T_{ij} = \frac{1}{t_{ij}} \begin{bmatrix} 1 & r_{ij} \\ r_{ij} & 1 \end{bmatrix} \tag{C.10}$$

the same can be applied for the propagation of the wave through the layer i, with the result [156][157]:

$$T_i = \begin{bmatrix} e^{j\,k_{x,i}\,d_i} & 0 \\ 0 & e^{j\,k_{x,i}\,d_i} \end{bmatrix} \tag{C.11}$$

multiplying all transfer matrices, for each interface and for each layer, results in the Transfer-Matrix $\mathbf{T}_{0N}$ from equation C2:

$$\mathbf{T}_{0N} = T_{01}\,T_1\,T_{12}\,...\,T_{(N-1)N} \tag{C.12}$$

The exact evaluation of the thickness, the transmittance, the reflection and the complex refractive index of each layer used in the OLED stack is crucial for the calculation of the amplitude of the reflected and transmitted wave through the stack. The software Setfos uses the prior measured parameters for the calculation of the influence of the passive optics on the propagating light beam through the media.

Bibliography

[1] C. W. Tang, S.A. VanSlyke. Appl. Phys. Lett. 51 913, (1987).

[2] J. H. Burroughes, D. D. C. Bradley, A. R. Brown, R. H. Marks, K. Mackay, R. H. Friend, P. L. Burns and A. B. Holmes, Nature 347, p.539 (1990).

[3] C. Zhong, C. Duan, F. Huang, H. Wu, Y. Cao, Chem. Mater. 23, p.326 (2011).

[4] J. Shinar, R. Shinar, J. Phys. D: Appl. Phys. 41, p133001 (2008).

[5] M. Riede, B. Lüssem, K. Leo, Comprehensive Semiconductor Science and Technology 4, p.448 (2011).

[6] R. H. Friend, R. W. Gymer, A. B. Holmes, J. H. Burroughes, R. N. Marks, C. Taliani, D. D. C. Bradley, D. A. Dos Santos, J. L. Brédas, M. Lögdlund, W. R. Salaneck, Nature 397, p.121 (1999).

[7] K. Meerholz, Nature 437, p.327 (2005).

[8] R. Das, P. Harrop, Organic & Printed Electronics Forecasts, Players & Opportunities 2007-2027, IDTechEx Ltd.

[9] T. Sasaoka, M. Sekiya, A. Yumoto, J. Yamada, T. Hirano, Y. Iwase, T. Yamada, T. Ishibashi, T. Mori, M. Asano, S. Tamura, T. Urabe, SID Symposium Digest of Technical Papers 32, 384 (2001).

[10] A. Mikami, T. Koshiyama, T. Tsubokawa, Jpn. J. Appl. Phys. 44, p.608 (2005).

[11] M. Eritt, C. May, K. Leo, M. Toerker, C. Radehaus, Thin Solid Films, 518 (11), p.3042 (2010).

[12] F. M. Tseng, A.-C. Cheng, Y.-N. Peng, Technological Forecasting and Social change 76, p.897 (2009).

[13] J. Shinar, R. Shinar, Comprehensive Nanoscience and Technology, V.1, p.73 (2010).

[14] S.-H. Eom, E. Wrzesniewski, J. Xue, Organic Electronics 12, p. 472 (2011).

[15] H.-Y. Lin, J.-H. Lee, M.-K. Wei, C.-L. Dai, C.-F. Wu, Y.-H. Ho, H.-Y. Lin, T.-C. Wu, Optics Communications 275, p.464 (2007).

[16] R. Bathelt, D. Buchhauser, C. Gärditz, R. Paetzold, P. Weilmann, Organic Electronics 8, p.293 (2007).

[17] K. Saxena, V. K. Jain, D. S. Mehta, Optical Materials 32, p.221 (2009).

[18] H. Hosono, Thin Solid Films 515, p.6000 (2007).

[19] J. Jancar, J. F. Douglas, F. W. Starr, S. K. Kumar, P. Cassagnau, A. J. Lesser, S. S. Sternstein, M. J. Buehler, Polymer 51, p.3321 (2010).

[20] F. So, B. Krummacher, M. K. Mathai, D. Poplavskyy, S. A. Choulis, V.-E. Choong, J. Appl. Phys. 102, 091101 (2007).

[21] A. Köhler, H. Bässler, Materials Science and Engineering R 66, p.71 (2009).

[22] F. Schindler, Dissertation, Ludwig-Maximilians-Universität München (2006).

[23] M. Hoffmann, Script; Organic Semiconductors, Institut für Angewandte Photophysik, TU Dresden (2006).

[24] S. A. Benning, Dissertation, University Paderborn (2004).

[25] N. C. Giebink, Y. Sun, S. R. Forrest, Organic Electronics 7, p.375 (2006).

[26] B. Wardle: "‘Principles and Applications of Photochemistry"’, John Wiley & Sons, Ltd. (2009).

[27] F. Kozlowski, Dissertation, Technische Universität, TU Dresden (2005).

[28] M. Gross, Dissertation, Ludwig-Maximilians-Universität München (2006).

[29] I.-S. Park, S.-R. Park, D.-Y. Shin, J.-S. Oh, W.-J. Song, J.-H. Yoon, Organic Electronics 11, p.218 (2010).

[30] S. - A. Chen, T. - H. Jen, H. - H. Lu, J. Chin. Chem. Soc., Vol. 57, No. 3B, p. 439 (2010).

[31] F. Laquai, Dissertation, Johannes-Gutenberg-Universität, Mainz (2006).

[32] M. G. Kaplunov, S. S. Krasnikova, S. L. Nikitenko, N. L. Sermakasheva, I. K. Yakushchenko, Nanoscale Res Lett. 7, p.206 (2012).

[33] P. S. Davids, S. M. Kogan, I. D. Parker, D. L. Smith, Appl. Phys. Lett. 69 (15), (1996).

[34] Y. Kawabe, G. E. Jabbour, S. E. Shaheen, B. Kippelen, N. Peyghambarian, Appl. Phys. Lett. 71 (10) (1997).

[35] H. Bässler, Poly. Adv. Technol, 9, 402, (1998).

[36] A. B. Walker, A. Kambili, S. J. Martin, J.Phys.: Condens. Matter 14, p.9825 (2002).

[37] D. M. Taylor, IEEE Transactions and Electrical Insulation, Vol.13, No.5, (2006).

[38] W. D. Gill, J. Appl. Phys., Vol.43, No.12 (1972).

[39] P. M. Borsenberger, J. Appl. Phys., Vol. 68, No. 11, p.5682 (1990).

[40] R. H. Parmenter, W. Ruppel, J. Appl. Phys., Vol.30, No.10 (1959).

[41] P. W. M. Blom, M. J. M. de Jong, J. J. M. Vleggaar, Appl. Phys. Lett. 68, (23), p.3308 (1996).

[42] W. L. Barnes, J. Lightwave Technol. 17 (11), p.2170 (1999).

[43] S. Möller, S. R. Forrest, J. Appl. Phys., Vol. 91, No. 5, (2002).

[44] H. Greiner, Jpn. J. Appl. Phys. 46 (No. 7A), 4125 (2007).

[45] John C. Ho, PhD-Thesis, MIT (2004).

[46] S. Asada, IEEE Journal of Quantum Electronics 27 (4), 884 (1991).

[47] C. Genet, T. W. Ebbesen, Nature 445 (7123), 39 (2007).

[48] P. A. Hobson, S. Wedge, J. A. E. Wasey, I. Sage, W. L. Barnes, Adv. Mater. 14 (19), p.1393 (2002).

[49] F. Flory, L. Escoubas, Gerard Berginc, Journal of Nanophotonics, Vol. 5, 052502-1 (2011).

[50] M.-K. Wei, C.-W. Lin, C.-C. Yang, Y.-W. Kiang, J.-H. Lee, H.-Y. Lin, Int. J. Mol. Sci. 11, p.1527 (2010).

[51] N. Takada, T. Tsutsui, S. Saito, Appl. Phys. Lett. 63, p.2032 (1993).

[52] J. C. Manifacier, J. Gasiot, J. P. Fillard, Journal of Physics E, 9, p.1002 (1976).

[53] C. A. Wilson, R. K. Grubbs, S. M. George, Chem. Mater. 17, p.5625 (2005).

[54] Jill Svenja Becker, PhD Thesis, Harvard University (2002).

[55] Viljami Pore, PhD Thesis, University of Helsinki (2010).

[56] S. M. George, Chem. Rev., Vol. 110, No. 1, p.111 (2010).

[57] M. D. Groner, F. H. Fabreguette, J. W. Elam, S. M. George, Chem. Mater., Vol. 16, No. 4, p.639 (2004).

[58] R. L. Puurunen, W. Vandervorst, J. Appl. Phys. 96, p.7686 (2004).

[59] J. D. Ferguson, A. W. Weimer, S. M. George, Chem. Mater. 16, p.5602 (2004).

[60] K. Neyts, A. U. Nieto, J. Opt. Soc. Am. A, Vol.23, No.5 (2006).

[61] K. Saxena, V. K. Jain, D. S. Mehta, Optical Materials 32, p.221, (2009).

[62] S. M. Jeong, F. Araoka, Y. Machida, K. Ishikawa, H. Takezoe, S. Nishimura, G. Suzaki, Appl. Phys. Lett. 92, p.083307 (2007).

[63] C. F. Madigan, M.-H. Lu, J. C. Sturm, Appl. Phys. Lett. 13, p.1650 (2000).

[64] Y. Sun, S. R. Forrest , Journal of Applied Physics 100, p.073106 (2006).

[65] Y. Sun, S. R. Forrest, Nature Photonics 2, p.483 (2008).

[66] J. Meyer, P. Görrn, S. Hamwi, H.-H. Johannes, T. Riedl, W. Kowalsky, Appl. Phys. Lett. 93, p.073308 (2008).

[67] J. J. Berry, D. S. Ginley, P. E. Burrows, Appl.Phys.Lett. 92, p.193304 (2008).

[68] Y. Tomita, C. May, M. Toerker, J. Amelung, M. Eritt, F. Loeffler, C. Luber, K. Leo, K. Walzer, K. Fehse, Q. Huang, Appl. Phys. Lett. 91, p.063510 (2007).

[69] C. D. Williams, R. O. Robles, M. Zhang, S. Li, R. H. Baughman, A. A. Zakhidov, Appl. Phys. Lett. 93 183506 (2008).

[70] Y. Wang, C. A. Di, Y. Liu, H. Kajiura, S. Ye, L. Cao, D. Wei, H. Zhang, Y. Li, K. Noda, Adv. Mater. 20 4442-9 (2008).

[71] Z. Wu, Z. Chen, X. Du, J. M. Logan, J. Sippel, M. Nikolou, K. Kamaras, J. R. Reynolds, D. B. Tanner, A. F. Hebard, A. G. Rinzler, Science 305, No. 5688, p.1273 (2004).

[72] J. Meiss, M. K. Riede, K. Leo, Appl. Phys. Lett. 94, p.013303 (2009).

[73] B. O'Connor, C. Haughn, K. - H. An, K. P. Pipe, M. Shtein, Appl. Phys. Lett.93, p.223304 (2008).

[74] H. Peng, X. Zhu, J. Sun, Z. Xie, S. Xie, M. Wong, H.-S. Kwok, Appl. Phys. Lett. 87, p.173505 (2005).

[75] S. Giurgola, A. Rodríguez, L. Martínez, P. Vergani, F. Lucchi, S. Benchabane, V. Pruneri, J. Mater. Sci: Mater. Electron. 20, p.181 (2009).

[76] D. Krautz, S. Cheylan, D. S. Ghosh, V. Pruneri, Nanotechnology 20, p.275204 (2009).

[77] S. Cheylan, D. S. Ghosh, D. Krautz, T. L. Chen, V. Pruneri, Org. Electron. 12, p.818 (2011).

[78] L. Martinez, D. S. Ghosh, S. Giurgiola, P. Vergani, V. Pruneri, Opt. Mater. 31, p.1115 (2009).

[79] A. B. Walker, A. Kambili, S. J. Martin, J.Phys.: Condens. Matter 14, p.9825 (2002).

[80] S. Nowy, N. A. Reinke, J. Frischeisen, W. Brütting, Proc. of SPIE Vol. 6999, 69992V, (2008).

[81] G. K. Hall, C. H. B. Mee, Phys.Status.Solidi.a 5, p.389 (1971).

[82] H. Hornauer, J. Vancea, G. Reiss, H. Hoffmann, Zeitschrift für Physik, B: Condensed Matter 77(3), p.399 (1989).

[83] G. Haacke, J. Appl. Phys. 47, 4086 (1976)

[84] U. Scherf, E. J. W. List, Adv. Materials 14, No. 7, p.477 (2002).

[85] N. A. Reinke, C. Ackermann, W. Brütting, Optics Communications 266, p.191 (2006).

[86] P. E. Burrows, Z. Shen, V. Bulovic, D. M. McCarty, S. R. Forrest, J. A. Cronin, M. E. Thompson, J. Appl. Phys., Vol. 79, No. 10, p.7991 (1996).

[87] Y. - R. Jeng, M. - L. Guo, H. - C. Li, T. - F. Guo, Electrochemical and Solid-State Letters, 10 (12), p.139 (2007).

[88] K. Hong, J. - L. Lee, Electron. Mater. Lett. Vol. 7, No. 2, p.77 (2011).

[89] S. H. Kim, J. Jang, J. Y. Lee, Appl. Phys. Lett. 91, p.103501 (2007).

[90] M. Kuik, L. J. A. Koster, A. G. Dijkstra, G. A. H. Wetzelaer, P. W. M. Blom, Organic Electronics 13, p.969 (2012).

[91] B. Perucco, N. A. Reinke, D. Rezzonico, M. Moos, B. Ruhstaller, Optics Express 18, (2010).

[92] G. G. Malliaras, J. C. Scott, J. Appl. Phys., Vol. 85, No. 10, p.7426, (1999).

[93] S. Woo, J. Kim, G. Cho, K. Kim, H. Lyu, Y. Kim, Journal of Industrial and Engineering Chemistry 15, p.716 (2009).

[94] Y. Iwama, D. C. Cho, T. Mori, T. Mizutani, Proceedings of the 7th Intemational Conference on Properties and Applications of Dielectric Materials, Nagoya (2003).

[95] A. Benor, S.-Y. Takizawa, C. Perez-Bolivar, P. Anzenbacher Jr., Organic Electronics 11, p.938 (2010).

[96] S. Y. Kim, J. - L. Lee, K. - B. Kim, Y. - H. Tak, J. Appl. Phys., Vol. 95, No. 5, (2004).

[97] M. G. Helander, Z. - B. Wang, M. T. Greiner, Z. - W. Liu, J. Qiu, Z. - H. Lu, Adv. Mater. 22, p.2037 (2010).

[98] K. Tamano, D.-C. Cho, T. Mori, T. Mizutani, M. Sugiyama, Thin Solid Fims 438, 182 (2003).

[99] C.-W. Chen, P.-Y. Hsieh, H.-H. Chiang, C.-L. Lin, H.-M. Wu, C.-C. Wu, Appl. Phys. Lett. 83, 5127 (2003).

[100] G. Papadimitropoulos, N. Vourdas, V. E. Vamvakas, D. Davazoglou, J. Phys.: Conf. Ser. 10 p.182 (2005).

[101] D. S. Gosh, R. Betancur, T. L. Chen, V. Pruneri, J. Martorell, Sol. Energy Mater. Sol. Cells 95, p.1228 (2011).

[102] D.S. Ghosh, T.L. Chen, V. Pruneri, Appl. Phys. Lett. 96, 091106 (2010).

[103] Z. B. Wang, M. G. Helander, J. Qiu, D. P. Puzzo, M. T. Greiner, Z. M. Hudson, S. Wang, Z. W. Liu, Z. H. Lu, Nature Photonics 5, p.753 (2011).

[104] S. K. So, W. K. Choi, C. H. Cheng, L. M. Leung, C. F. Kwong, Appl. Phys. A 68, p.447 (1999).

[105] J.S. Kim, R.H. Friend, F. Cacialli, Synthetic Metals 111-112, p.369 (2000).

[106] R. H. Jordan, A. Dodabalapur, R. E. Slusher, Appl. Phys. Lett. 69, p.1997 (1996).

[107] E. F. Shubert, N. E. J. Hunt, M. Micovic, R. J. Malik, D. L. Sivco, A. Y. Cho, G. J. Zydzik, Science 265 p.943 (1994).

[108] Y. Sun, N. C. Giebink, H. Kanno, B. Ma, M. E. Thompson, S. R. Forrest, Nature 440, 908 (2006).

[109] S. Reineke , F. Lindner , G. Schwartz , N. Seidler , K. Walzer , B. Lüssem , K. Leo , Nature 459, 234 (2009).

[110] S. Y. Ryu, J. T. Kim, J. H. Noh, B. H. Hwang, C. S. Kim, S. J. Jo, H. Seok Hwang, S. J. Kang, H. K. Baik, C. H. Lee, S. Y. Song, S. J. Lee, Appl. Phys. Lett. 92, 103301 (2008).

[111] M. Zhang, S. Xue, W. Dong, Q. Wang, T. Fei, C. Gu, Y. Ma, Chem. Commun. 46, 3923 (2010).

[112] N. Rehmann, C. Ulbricht, A. Köhnen, P. Zacharias, M. C. Gather, D. Hertel, E. Holder, K. Meerholz, U. S. Schubert, Adv. Mat. 20, p.129 (2008).

[113] L. Duan, L. Hou, T. - W. Lee, J. Qiao, D. Zhang, G. Dong, L. Wanga, Y. Qiu, J. Mater. Chem., 20, p.6392 (2010).

[114] S.-R. Tseng, H.-F. Meng, K.-C. Lee, S.-F. Horng, Appl. Phys. Lett. 93, 153308 (2008).

[115] US Patent 7063994 - Organic semiconductor devices and methods of fabrication including forming two parts with polymerisable groups and bonding the parts.

[116] C.-Y. Chang, F.-Y. Tsai, S.-J. Jhuo, M.-J. Chen, Organic Electronics 9, Issue 5, p.667 (2008).

[117] J. C. Bernède, A. Godoy, L. Cattin, F. R. Diaz, M. Morsli and M. A. del Valle (2010). Organic Solar Cells Performances Improvement Induced by Interface Buffer Layers, Solar Energy, Radu D Rugescu (Ed.), ISBN: 978-953-307-052-0, InTech.

[118] J. W. Elam, S. M. George, Chem. Mater., Vol. 15, No. 4, p.1020 (2003).

[119] S. D. Elliott, G. Scarel, C. Wiemer, M. Fanciulli, G. Pavia, Chem. Mater., Vol. 18, No. 16, p.3764 (2006).

[120] B. D. Chin, N. S. Kang, J.-W. Yu, S. M. Jo, J. Y. Lee, J. Appl. Phys. 102, p.024506 (2007).

[121] M.D. Groner, F.H. Fabreguette, J.W. Elam, S.M. George, Chem. Mater. 16, p.639 (2004).

[122] T. - W. Lee, O. O. Park, Adv. Mater. 12, No. 11, p.801 (2000).

[123] Z. B. Deng, X. M. Ding, S. T. Lee, W. A. Gambling, Appl. Phys. Lett. 74, p.2227 (1999).

[124] H. C. Lin, P. D. Yea, G. D. Wilk, Appl. Phys. Lett. 87, p.182904 (2005).

[125] C. Zhong, C. Duan, F. Huang, H. Wu, Y. Cao, Chem. Mater., Vol. 23, No. 3, p.326 (2011).

[126] J. - D. You, S. - R. Tseng, H. - F. Meng, F. - W. Yen, I. - F. Lin, S. - F. Horng, Organic Electronics 10, p.1610 (2009).

[127] S. - M. Cho, J. - H.Bae, E. Jang, M. - H. Kim, C. Lee, S. - D. Lee, Semicond. Sci. Technol. 27, p.125018 (2012).

[128] C. Zhang, S. Liu, F. Wang, Y. Zhang, Microelectronics Journa l39, p.1525 (2008).

[129] T. - C. Lin, C. - H. Hsiao, J. - H. Lee, Proc. of SPIE Vol. 5937, 59371Q, (2005).

[130] PhD-Thesis, Stefan Nowy, University Augsburg (2010).

[131] J. C. Scott, P. J. Brock, J. R. Salem, S. Ramos, G. G. Malliaras, S. A. Carter, L. Bozano, Synthetic Metals 111-112, p.289 (2000).

[132] J. H. Ahn, C. Wang, C. Pearson, M. R. Bryce, M. C. Pettya, Appl. Phys. Lett., Vol. 85, No. 7, p.1283 (2004).

[133] L. D. Bozano, K. R. Carter, V. Y. Lee, R. D. Miller, R. DiPietro, J. C. Scott, J. Appl. Phys., Vol. 94, No. 5, p.3061 (2003).

[134] S. de F. C. da Silva, M. Foschini, H. S. Silva, J. R. Tozoni, F. A. Castro, R. A. Silva, A. Marletta, Organic Electronics 13, p.2935 (2012).

[135] D. Y. Kim, J. K. Grey, P. F. Barbara, Synthetic Metals 156, p.336 (2006).

[136] P. Cea, Y. Hua, C. Pearson, C. Wang, M. R. Bryce, F. M. Royo, M. C. Petty, Thin Solid Films 408. p.275 (2002).

[137] J. H. Ahn, C. Wang, N. E. Widdowson, C. Pearson, M. R. Bryce, M. C. Petty, Journal of Applied Physics 98, p.054508 (2005).

[138] G. Saygili, C. Varlikli, C. Zafera, C. Ozsoya, Synthetic Metals 162, p.621 (2012).

[139] D. Krautz, E. Lunedei, J. Puigdollers, G. Badenes, R. Alcubilla, S. Cheylan, Appl. Phys. Lett. 96, p.033301 (2010).

[140] R. Jakubiak, C. J. Collison, W. C. Wan, L. J. Rothberg, and B. R. Hsieh, J. Phys. Chem. A 103, 2394 (1999).

[141] V. Sholin, E. J. Lopez-Cabarcos, S. A. Carter, Macromolecules, Vol. 39, No. 17, p.5830 (2006).

[142] Y. Shi, J. Liu, Y. Yang, J. Appl. Phys., Vol. 87, No. 9, p.4254 (2000).

[143] K. Thangaraju, J. Kumar, P. Amaladass, A. K. Mohanakrishnan, V. Narayanan, Appl. Phys. Lett. 89, p.082106 (2006).

[144] C. A. Amorim, M. R. Cavallari, G. Santos, F. J. Fonseca, A. M. Andrade, S. Mergulhão, Journal of Non-Crystalline Solids 358, p.484 (2012).

[145] A. Fuchs, T. Steinbrecher, M. S. Mommer, Y. Nagata, M. Elstner, C. Lennartz, Phys. Chem. Chem. Phys. 14, p.4259 (2012).

[146] K. - H. Choi, D. - H. Hwang, H. - M. Lee, L. - M. Do, T. Zyung, Synthetic Metals 96, p.123 (1998).

[147] R. Jakubiak, C. J. Collison, W. C. Wan, L. J. Rothberg, and B. R. Hsieh, J. Phys. Chem. A 103, 2394 (1999).

[148] K. - M. Yeh, Y. Chen, Organic Electronics 9, p.45 (2008).

[149] M. Valadares, I. Silvestre, H. D. R. Calado, B. R. A. Neves, P. S. S. Guimarães, L. A. Cury, Materials Science and Engineering C 29, p.571 (2009).

[150] M. D. McGehee, T. Bergstedt, C. Zhang, A. P. Saab, M. B. O'Regan, G. C. Bazan, V. I. Srdanov, A. J. Heeger, Adv. Mater. 11, No. 16, p.1349 (1999).

[151] Y. Qiu, L. Duan, X. Hu, D. Zhang, M. Zheng, F. Bai, Synthetic Metals 123, p.39 (2001).

[152] T. Q. Nguyen, I. B. Martini, J. Liu, B. J. Schwartz, J. Phys. Chem. B 104, p.237 (2000).

[153] R. Pizzoferrato, T. Ziller, A. Micozzi, A. Ricci, C. L. Sterzo, A. Ustione, C. Oliva, A. Cricenti, Chemical Physics Letters 414, p.234 (2005).

[154] B. Ruhstaller, J. C. Scott, P. J. Brock, U. Scherf, S. A. Carter, Chem. Phys. Lett. 317, p.238 (2000).

[155] Fluxim Setfos 3.3, Handbook and Tutorial (2013).

[156] Z. Ye, PhD-Thesis, Iowa State University (2011).

[157] C. C. Katsidis, D. I. Siapkas, Applied Optics Vol. 41, No. 19, p.3978 (2002).

[158] M. C. Troparevsky, A. S. Sabau, A. R. Lupini, Z. Zhang, Opt Express. 18 p.24715 (2010).

Appendix D

Publications

Talks

D. S. Ghosh, T. L. Chen, D. Krautz, S. Cheylan, V. Pruneri: *"‘Environmentally stable Al – doped ZnO transparent electrode for organic optoelectronic devices"’*, Renewable Energy and the Environment, Austin, TX, USA, 2. – 4. November 2011

D. S. Ghosh, T. L. Chen, D. Krautz, S. Cheylan, V. Pruneri: *"‘Ultrathin metal for indium free organic lighting and photovoltaics"’*, Photonics 2010, 10th International conference on fiber optics and photonics, Guwahati, India, December 2010

D. S. Ghosh, D. Krautz, S. Cheylan, V. Pruneri: *"‘Ultrathin metal transparent electrodes for lighting and photovoltaic applications"’*, Optics and Photonics for Advanced Energy Technology, Cambridge (USA), 24. June 2009

S. Cheylan, D. Krautz, J. Puigdollers, C. Voz, R. Alcubilla, G. Badenes: *"‘Enhanced performance of OLEDs using polymer blends as the active layer"’*, 7th Conference on Electron Devices (CDE 09), Santiago de Compostela, 11. – 13. February 2009

S. Cheylan, D. Krautz, J. Puigdollers, C. Voz, R. Alcubilla, G. Badenes: *"‘Enhanced performance of OLED based on a molecularly doped polymer"’*, 1st International Symposium on Flexible Organic Electronics (IS – FOE), Greece, Halkidiki, 9. – 11. July 2008

D. Krautz, S. Cheylan, J. Puigdollers, C. Voz, R. Alcubilla, G. Badenes: *"‘Enhanced performance of OLEDs based on a molecularly DOPED polymer"’*, International Symposium on Flexible Electronics (ISFE), Spain, Tarragona, 6. – 9. April 2008

D. Krautz, S. Cheylan, J. Puigdollers, C. Voz, R. Alcubilla, G. Badenes: *"‘Polymeric Blends for organic light emitting diodes"’*, ENMM07, VIII Escuela Nacional de Materiales Moleculares, Spain, Estepona, 20. – 27. May 2007

S. Cheylan, H. Bolink, A. Fraleoni – Morgera, D. Krautz, J. Puigdollers, C. Voz, L. Setti, R. Alcubilla, G. Badenes: *"‘Single layer organic light emitting diode based on a thiophene polymer"’*, CDE07, Conferencia de Dispositivos Electronicos, San Lorenzo del Escorial, January 2007

Posters

D. Krautz, D. S. Ghosh, V. Pruneri, S. Cheylan: *"‘Nickel as an alternative semitransparent anode to Indium Tin Oxide for OLED application"’*, European Conference on Molecular Electronics – ECME09, Copenhagen, Denmark, 09. – 12. September 2009

D. Krautz, S. Cheylan, J. Puigdollers, C. Voz, R. Alcubilla, G. Badenes: *"‘Enhanced performance of OLED based on a molecularly doped polymer after thermal annealing"’*, ICEL – 7, 7th International Conference on Electroluminescence of Molecular Materials and Related Phenomena, Dresden, Germany, 02. – 06. September 2008

D. Krautz, S. Cheylan, H. Bolink, A. Fraleoni – Morgera, J. Puigdollers, C. Voz, L. Setti, R. Alcubilla, G. Badenes: *"‘Thiophene polymer containing a cyano group as a side chain substituent for OLED application"’*, ICEO08, 4th International Conference on Organic Electronics, Eindhoven, The Netherlands, 16. – 18. June 2008

A. Fraleoni – Morgera, S. Cheylan, D. Krautz, J. Puigdollers, L. Setti, I. Mencarelli, R. Alcubilla, G. Badenes: *"‘Photophysical properties of polythiophenes containing different amounts of cyano functional group as a side chain substituent"’*, EMRS08, European Material Research Society Spring Meeting, Strasbourg, France, 26. – 30. May 2008

D. Krautz, S. Cheylan, J. Puigdollers, C. Voz, R. Alcubilla, G. Badenes: *"‘Solvent influence on the performance of OLEDs based on polyfluorenes"’*, WIP08, School on Photonic Metamaterials, Paris, France, 14. – 18. April 2008

S. Cheylan, D. Krautz, J. Puigdollers, C. Voz, R. Alcubilla, G. Badenes: *"‘Organic Blend for Light Emitting Diodes"’*, ECME07, European Conference on Molecular Electronics, Metz, France, 5. – 08 September 2007

D. Krautz, S. Cheylan, H. Bolink, A. Fraleoni – Morgera, J. Puigdollers, C. Voz, L. Setti, R. Alcubilla, G. Badenes: *"‘Single layer organic light emitting diode based on a thiophene polymer with a cyano group"’*, PHOREMOST Workshop and General Meeting, "‘Advances in Nanophotonics"’, Vilnius, Lithuania, 26. – 28. September 2006

Papers

T. L. Chen, D. S. Ghosh, D. Krautz, S. Cheylan, V. Pruneri: *"‘Highly stable Al – doped ZnO transparent conductors using an oxidized ultrathin metal capping layer at its percolation thickness"’*, Appl. Phys. Lett. 99, (2011) 093302

S. Cheylan, D. S. Ghosh, D. Krautz, T. L. Chen, V. Pruneri: *"‘Organic light – emitting diode with indium – free metallic bilayer as transparent anode"’*, Organic Electronics 12, (2011) 818

D. Krautz, E. Lunedei, J. Puigdollers, G. Badenes, R. Alcubilla, S. Cheylan: *"‘Interchain and intrachain emission branching in polymer light – emitting diode doped by organic molecules"’*, Applied Physics Letter, 96 (2010) 033301

D. Krautz, S. Cheylan, D. S. Gosh, V. Pruneri: *"‘Nickel as an alternative semitransparent anode to Indium Tin Oxide for polymer LED application"’*, Nanotechnology, 20 (2009) 275204

Research Stays

15.02.2009 - 14.08.2009, *Merck Chemicals Ltd*, Chilworth Technical Centre, University Parkway Southampton, SO16 7QD, United Kingdom

09.09.2008 - 10.09.2008, *Chair of Display Technology*, University Stuttgart, Allmandring 3b, 70569 Stuttgart, Germany

08.09.2008 - 08.09.2008, *Siemens AG*, Corporate Technology, Innovative Electronics, CT MM 1 Günther – Scharowsky – Str. 1, 91058 Erlangen, Germany

05.03.2007 - 09.03.2007, *Chair of Display Technology*, University Stuttgart, Allmandring 3b, 70569 Stuttgart, Germany